TECHNISCHE UNIVERSITÄT MÜNCHEN
Fachgebiet Theoretische Chemie

The DFT + U Method in the Framework of the Parallel Density Functional Code ParaGauss

Raghunathan Ramakrishnan

Vollständiger Abdruck der von der Fakultät für Chemie der Technischen Universität München zur Erlangung des akademischen Grades eines

Doktors der Naturwissenschaften (Dr. rer. nat.)

genehmigten Dissertation.

Vorsitzender: Univ.-Prof. Dr. K. Köhler

Prüfer der Dissertation:

1. Univ.-Prof. Dr. N. Rösch
2. Univ.-Prof. Dr. M. Kleber

Die Dissertation wurde am 22.02.2011 bei der Technischen Universität München eingereicht und durch die Fakultät für Chemie am 15.03.2011 angenommen.

Acknowledgments

The knowledge I gained during the course of my thesis work is very valuable to me and I am very thankful to my supervisor, Prof. Dr. Notker Rösch, for giving me the opportunity to work for my doctoral thesis in his research group and for his interest in this project. Prof. Rösch's constant advising in both scientific and non-scientific issues are very important to me and I think that they came at the right time of my academic career. I wish to thank Prof. Dr. Manfred Kleber for refereeing my fellowship reports and providing feedbacks.

It is a pleasure to thank Dr. Alexei Matveev for helping me improve my programming skills and for various discussions. I am indebted to Dr. Sven Krüger for various discussions and helps through out my project.

I would like to thank Dr. Sonjoy Majumder for his help during the initial phase of the project. I am thankful to my office room mates, past and present, Dr. Sun Qiao, Ajanta Deka, Prof. B. Dunlap, Dr. Ji Lai, Yin Wu, Thomas Martin Soini, Chun-Ran Chang, Dr. Kremleva Alena for various helps and to give me enough space to make me feel at home.

I thank Frau. Ruth Mösch, Frau. Barbara Asam for various administrative helps. I thank my colleagues Dr. Alena Ivanova, Dr. Alexander Genest, Dr. Amjad Mohammed Basha, Astrid Nikodem, Dr. Benjami Martorell, David Tittle, Duygu Başaran, Dr. Egor Vladimirov, George Beridze, Gopal Dixit, Dr. Grigory Shamov, Dr. Grzegorz Jezierski, Dr. Hristiyan Aleksandrov, Dr. Ilya Yudanov, Dr. Ion Chiorescu, Dr. Juan Santana, Dr. Lyudmila Moskaleva, Manuela Metzner, Mayur Karwa, Miquel Huix i Rotllant, Dr. Miriam Häberle, Dr. Olga Zakharieva, Ralph Koitz, Dr. Rupashree Shyama Ray, Dr. Sergey Bosko, Shane Parker, Siham Naima Derrar, Dr. Virve Karttunen, Dr. Vladimir Nasluzov, Dr. Wilhelm Eger, and Zhijian Zhao for providing a friendly working environment.

I thank the library, academic and non-academic staff members of Technische Universität München for their excellent service. Thanks are also due to various land ladies and Hausmeister(in) for making life simple in Munich.

I am grateful to Prof. Krishnan Mangala Sunder for his interest in my academic progress and for various discussions and helps for a very long time.

I thank my wife Shampa, my brother and my parents whose love, support and encouragement enabled me to complete this work.

Finally, I gratefully acknowledge Deutscher Akademischer Austausch Dienst for awarding me a fellowship to carry out my doctoral research in Germany.

Dedicated to my teachers

Contents

1 Introduction **1**

1.1 Theory 1

1.2 Applications 6

1.3 Overview of the Thesis 7

2 Kohn–Sham Density Functional Theory **9**

2.1 The Kohn–Sham Method 9

2.1.1 Background 9

2.1.2 The Kohn–Sham Approach 11

2.1.3 Approximate Exchange-Correlation Functionals 14

2.2 Generalization and Interpretation of Kohn–Sham Theory 16

2.2.1 Non-Integer Orbital Occupation Numbers 16

2.2.2 Scaling Relations for Density Functionals 17

2.2.3 Orbital Energies 18

2.3 Self-interaction Error 19

2.3.1 Conditions for Exact Exchange-Correlation Functionals 19

2.3.2 Self-Interaction Cancellation by Semi-Local Functionals 21

2.3.3 Manifestations of the Self-Interaction Error 27

2.3.4 Self-Interaction Correction Schemes 30

3 The DFT + U Methodology **33**

3.1 The DFT + U Formalism 34

3.1.1 The DFT + U Functional form 35

3.1.2 Orbital Occupation Matrix 40

3.2 DFT + U Hamiltonian Matrix and Analytic Gradients 43

3.2.1 Some Useful Expressions 44

3.2.2 DFT + U Hamiltonian Correction Matrix 45

3.2.3 DFT + U Analytic Gradients 46

3.3 Implementation . . . 47
3.3.1 Intermediate Procedures . . . 48
3.3.2 Parallelization of Gradient Computation . . . 48
3.4 FLL-DFT + U corrections . . . 51

4 Computational Details **55**
4.1 Method . . . 55
4.2 Effective Onsite-Coulomb Parameter . . . 56

5 DFT + U Application to Lanthanides **61**
5.1 Lanthanide Trifluorides . . . 62
5.1.1 Role of $4f$ Orbitals in the Bonding of LuF_3 . . . 63
5.1.2 Role of $5d$ Orbitals in the Bonding of LnF_3 . . . 71
5.2 Ceria Nanoparticles . . . 74
5.2.1 Model Nanoparticles . . . 76
5.2.2 Results and Discussions . . . 77

6 DFT + U Application to Actinides **83**
6.1 Uranyl Dication . . . 84
6.1.1 Results and Discussions . . . 85
6.1.2 Conclusions . . . 94
6.2 Penta Aqua Uranyl . . . 95
6.2.1 Results and Discussions . . . 95
6.2.2 Conclusions . . . 105
6.3 Uranyl Monohydroxide . . . 105
6.3.1 Results and Discussions . . . 106
6.3.2 Conclusions . . . 121

7 Summary and Outlook **123**

A Basis sets **127**

Bibliography **137**

List of abbreviations

B3LYP	Becke 3-parameter Lee–Yang–Parr
BP	Becke–Perdew
CCSD(T)	Coupled-Cluster with Single and Double and Perturbative Triple excitations
DF	Density Functional
DFT	Density Functional Theory
DKH	Douglas–Kroll–Hess
FF	Fitting Function
FOJT	First-Order Jahn-Teller
GGA	Generalized Gradient Approximation
HF	Hartree–Fock
HFS	Hartree–Fock–Slater
HK	Hohenberg–Kohn
HOMO	Highest Occupied Molecular Orbital
IP	Ionization Potential
KS	Kohn–Sham
LCAO	Linear Combination of Atomic Orbitals
LCGTO	Linear Combination of Gaussian-Type Orbitals
LUMO	Lowest Unoccupied Molecular Orbital
LDA	Local Density Approximation
MO	Molecular Orbital
MP2	Second-order Møller–Plesset perturbation theory
MGGA	Meta Generalized Gradient Approximation
PBE	Perdew–Burke–Ernzerhof
PBE0	Zero parameter hybrid functional based on PBE
PBEN	Hammer, Hansen, and Nørskov revision of PBE
PW91	Perdew–Wang, year 1991
RECP	Relativistic Effective-Core Potential

RPA	Random Phase Approximation
SCF	Self-Consistent Field
SD	Slater–Dirac
SI	Self-Interaction
SIC	Self-Interaction Correction
SIE	Self-Interaction Error
SOJT	Second-Order Jahn-Teller
TPSS	Tao–Perdew–Staroverov–Scuseria
UHF	Unrestricted Hartree–Fock
VWN	Vosko–Wilk–Nusair
XC	Exchange-Correlation
ZORA	Zero-Order Regular Approximation

Chapter 1

Introduction

1.1 Theory

A major focus of research in quantum chemistry is to examine existing methods and to improve them to solve the electronic Schrödinger equation of atoms, molecules and solids [1]. The earliest attempt to solve the Schrödinger equation of atomic systems was led by D. R. Hartree [1, 2]. He assumed that in a system of N electrons surrounding a fixed nucleus, each electron experiences a field due to the mean field of other $N-1$ electrons and the nucleus. Hartree approximated the effect of many body interactions by the potential which arises from the $N-1$ electrons distributed according to their own wavefunctions ψ_i and solved the corresponding Schrödinger equation for the single electron orbitals ψ_i. N of these wavefunctions represent the occupied states of the atom and $|\psi_i|^2$ gives the magnitude of charge density of the i-th electron. The total charge density ρ of the atomic system will be given by summing the orbital densities over the occupied orbitals.

Unlike the orbitals ψ_i, the electron density ρ of an atomic or molecular system is an observable quantity, for example, in X-ray scattering experiments, ρ is related to the spatial distribution of the electrons [3, 4]. Such an interpretation of ρ is natural and according to E. Schrödinger, electron density is the distribution of negative charge in real space [5, 6]. In Schrödinger's 1926 paper [5], he remarks that "We have repeatedly called attention to the fact that the ψ function itself cannot and may not be interpreted directly in terms of three-dimensional space—however much the one-electron problem tends to mislead us on this point—because it is in general a function in configuration space, not real space" (quoted from [6]).

The essential properties of the electron density have been briefly summarized in a recent review by R. F. W. Bader [6] as "the electron density provides a physical model of matter, one in which point-like nuclei are embedded in a relatively diffuse spatial distribution of negative charge—the density of electronic charge—a distribution that is static for a system in a stationary

state and one that changes in a continuous manner during any adiabatic change, i.e., one that does not involve a change in the electronic state of the system. In the spirit of the Born-Oppenheimer approximation to the vibronic wavefunction, the electron density is assumed to adjust instantaneously to any and all motions of the nuclei".

Thus, based on similar views, earlier attempts have been made to focus on the electron density when solving the Schrödinger equation. The theory of the inhomogeneous electron gas is aimed at describing the properties of the ground electronic state of a system by the electron density $\rho(\mathbf{r})$ and to provide methods to calculate this quantity. One of the earlier theories of the inhomogeneous electron gas is the semi-classical, statistical approximation commonly known as the Thomas–Fermi model [7].

Thomas–Fermi theory and its extensions were the predecessors of modern density functional theory (DFT). The objective of DFT is to describe the properties of a many-electron system using functionals of $\rho(\mathbf{r})$ [8]. DFT is founded on two theorems for the electron density which are collectively called as Hohenberg–Kohn theorems [9]. The first of these theorems, proves by contradiction that the ground-state electron density uniquely specifies the Hamiltonian operator of a system characterized by a universal *system-independent* density functional $F[\rho]$ and a *system-dependent* external potential $v_{ext}(\mathbf{r})$ that usually represents the electron-nuclear interaction. The first Hohenberg–Kohn theorem is an uniqueness theorem which establishes an one-to-one mapping between the electron density and the external potential. The second Hohenberg–Kohn theorem provides a variational procedure where minimization of the total energy functional $E[\rho]$ subject to the constraint that the electron density $\rho(\mathbf{r})$ integrates to the total number of electrons N, yields the ground state energy of a quantum mechanical N-electron system [10, 11]. Here the total energy functional $E[\rho]$ is the sum of the universal functional $F[\rho]$ and the energy contribution due to the electron-nuclear interaction, $\int \rho(\mathbf{r}) v_{ext}(\mathbf{r}) d\mathbf{r}$.

The universal, system-independent electron density functional $F[\rho]$ consists of a kinetic energy term and an electron-electron interaction term, the latter term can be further separated into a classical Coulomb term according to independent-particle approximation and a term that accounts for non-classical effects in a quantum mechanical system and many-body Coulomb effects. In the earlier density functional approach such as the Thomas–Fermi model, all the contributions to $F[\rho]$ were formulated as pure density functionals that are explicitly dependent on $\rho(\mathbf{r})$ only. Proposed functionals inaccurately modelled the kinetic energy contribution which predicted too large a positive energy contribution in molecular calculations so that molecules turned out to be unstable.

The present success of DFT is largely due to Kohn–Sham's formalism [12] of DFT (KS-DFT) that introduces a reference system of non-interacting electrons that are under the influence

of an effective potential. The Kohn–Sham approach gives procedures to solve the corresponding Schrödinger equation of these non-interacting electrons, to compute $\rho(\mathbf{r})$ using the orbitals of this reference system as described above in the case of Hartree's atomic calculations, and to compute the largest contribution to the universal density functional $F[\rho]$ which is the kinetic energy. In KS-DFT, the kinetic energy term is computed as an *orbital dependent term*. The leading contribution, the kinetic energy of the reference system of non-interacting electrons, turned out to be a good approximation to the kinetic energy of the real system of interacting electrons. KS-DFT retains the classical form of the Coulomb electron-electron interaction term which is formulated within the independent particle approximation as in the Thomas–Fermi model.

A cornerstone of KS-DFT is the introduction of the exchange-correlation (XC) functional. The purpose of the XC functional is to provide the *residual kinetic energy* (which is the difference between the kinetic energy of the real system and that of the reference system of non-interacting electrons), a relatively small part, and to include the non-classical electron-electron interaction energy namely the *exchange* energy as well as many-body Coulomb correlation effects. However the exact form of the XC functional is not known. Thus the accuracy of a proper KS-DFT calculation is strictly dependent on the approximations involved in modelling the XC functional. Approximate exchange-correlation functionals are often based on the properties of the hypothetical model of a homogeneous gas of interacting electrons. For this model, an exact form of the exchange energy density is known along with accurate form of the correlation part of the XC that has been found through quantum Monte Carlo simulations [10]. In this model, an electron gas containing virtually an infinite number of electrons is subjected to a positive background charge distribution in an infinite volume which leads to a constant electron density everywhere.

In the *local density approximation* (LDA), the assumption involved is that the XC energy of a real system has the same functional form as the XC energy of a uniform interacting gas of electrons with same density as the real system *locally* [10]. LDA is a good approximation for atoms, and the structure of many molecules and solids. The (relative) accuracy of LDA stems from the fact that LDA affords a surprisingly good representation of the spherically averaged hole function. *Gradient-corrected approximations* (for example, the generalized gradient approximation, GGA) afford an improved description as they account for the variation of ρ by including terms involving the gradient of the density $\nabla\rho$ [10] so as to describe a real atomic or molecular system which exhibit rapidly varying densities. Approximations beyond LDA and GGA focus on arriving at better and realistic functional forms of the density, for example, by including terms dependent on higher derivatives of the density, such as $\nabla^2\rho$ [10].

The main advantage of DFT over wavefunction-based methods is related to the above mentioned Schrödinger's remark about electron density that for a many-electron system, the electron

density $\rho(\mathbf{r})$ has a lower dimensionality than the N-electron wavefunction. Indeed while the cost of computation in the commonly used wavefunction based methods scale as B^4-B^7 for a many-electron system represented by *B-basis functions*, DFT-based methods lead to B^3-B^4 scaling [13]. For large systems, approximations to the *matrix elements* involved in a DFT calculation can provide even linear or quadratic (B^1-B^2) scaling [10].

While KS-DFT is an efficient alternative to wavefunction based theories, results of KS-DFT calculations especially when they employ LDA and GGA XC functionals can suffer from a subtle artifact. The classical Coulomb energy contribution includes spurious *self-interaction* (SI) contributions which represent unphysical electron-electron interactions such as an electron interacting with itself. In the exact KS-DFT, such contributions are supposed to be cancelled by corresponding *self-exchange* contributions in the XC functional, hence to correct for the self-interaction. Approximate XC functionals such as LDA and GGA only partly account for *self-interaction correction* (SIC) and the error thus introduced due to incomplete SIC is called as the *self-interaction error* (SIE).

Some of the major failures of LDA and GGA functionals such as low barriers of reactions, low band gaps of solids, spurious orbital mixing, underestimation of KS eigenvalues, wrong dissociation limits of molecules, destabilization of anions, overstabilization of cations are all manifestations of the self-interaction error. Although these situations have been widely identified, the magnitude of the errors they introduce in a KS-DFT calculation has only been vaguely understood [14, 15]. Thus in KS-DFT calculations employing approximate LDA or GGA functionals, a compromise between accuracy and computational efficiency is being made.

Improvements in the development of better XC functionals mostly come from investigations of properties of the hypothetical *exact XC* functional [16]. Some aspects of the properties of the exact XC functional are readily understood by inspecting exactly solvable one electron systems such as the hydrogen (H) atom and other model systems. Better XC functionals that are classified as *meta*-GGA [10] and *hyper*-GGA [10] functionals approximately model the *exact behavior*. Development of XC functionals which can consistently model the exact behavior of even small molecular systems is an active area of research [16].

In the so-called DFT + X methodologies [17], the DFT total energy functional (usually LDA and GGA) is augmented by a suitable model Hamiltonian in order to partly recover the exact behavior. While the major advantage of such schemes is the improvement of LDA and GGA approximations in an inexpensive way, these methodologies often involve inclusion of semi-empirical parameters. Thus in the DFT + X methodologies, a two-level hierarchy of parametrization should be noted. The semi-empirical parameters that eventually enter the XC functionals are characteristic of the level of XC approximation itself and not system specific. The parameters

that enter the model Hamiltonian are often specific to the implementation, the XC-functional, the system, the basis set used, and the application itself. Although these DFT + X methodologies are only crude approximations, they make it possible to improve the DFT description for larger or complex systems at a reduced computational cost and through careful studies of smaller systems one can gain more insight about the nature of the corrections they provide. Two widely used DFT + X approaches are the DFT + D and the DFT + U approaches.

In the DFT + D methodology [18, 19], the model Hamiltonian comprises $1/R^6$ terms which aims at describing the interatomic dispersive interactions. Thus dispersive interactions which alternatively require high-level *ab initio* methods can be included at a reduced computational expense.

The DFT + U methodology [20] which is the main subject of this thesis originates from diverse motivations thus resulting in the culmination of several variants of the model Hamiltonian. Historically, the DFT + U approach was used to improve the *local spin density approximation* (LSDA) description of systems that contain correlated electrons in localized d or f orbitals. In the LSDA + U approach an intra-atomic Hubbard U repulsion term is added to the DFT total energy Hamiltonian to reduce the intra-atomic *hybridization* of these localized orbitals by driving the occupations of these orbitals to take the integer values 0 or 1. Such *localization* of occupied orbitals tends to increase the *band gap* and to describe well the Mott insulating state of transition metal oxides [20]. Without such explicit inclusion of a Hubbard U repulsion term, the LSDA description predicts such metal oxides to be conducting. When applying the DFT + U approach to molecules as in the present work, the DFT + U correction Hamiltonian is aimed to approximately provide self-interaction corrections in LDA and GGA calculations to partly recover the correct electron-electron interaction. In this way, a model DFT approach is developed that allows one to study the effect of self-interaction in an atom-specific (even shell-specific) fashion.

PARAGAUSS is a program package to perform high-performance density functional calculations of molecular systems and clusters [21, 22]. A wide range of molecules, from small molecules comprising a few atoms to large clusters that contain up to several hundreds of atoms have been studied using PARAGAUSS. In this way valuable contributions have been made to various scientific disciplines such as theoretical and computational chemistry, spectroscopy, surface science, material science and environmental chemistry. A main theme in problem solving in any discipline of science is to exploit the available symmetry constraints. Symmetry-adapting a mathematical problem is one of the most basic and naturally efficient strategies especially when solving a quantum mechanical problem. In this respect, PARAGAUSS is one of the few electronic structure codes which can utilize *non-Abelian* point group symmetries to symmetry-adapt the electronic Schrödinger equation [23].

The complexity in molecular electronic structure calculations increases with the atomic numbers of the constituting atoms. A natural consequence of increasing atomic numbers is the need to incorporate relativistic effects on the electronic structure. In order to provide a relativistically correct description of spin-1/2 particles such as electrons, one has to solve the Dirac equation to get a wavefunction with four components and a set of eigenvalues where electronic and positronic contributions are coupled. When focussing only on the decoupled negative-energy spectrum of the Dirac Hamiltonian, an approximation strategy called the Douglas–Kroll–Hess (DKH) method can be employed which leads to an expansion of the Dirac Hamiltonian in the external potential. Truncation of this expansion to include a finite number of terms leads to DKH approximations of various orders. The second-order DKH approximation within which the aforementioned series expansion is sufficiently converged has been implemented in PARAGAUSS [24]. It is also possible to employ the *pseudopotential* strategy in PARAGAUSS to approximately model relativistic effects which are more relevant to core electrons.

While continuously used for contributing to the understanding of realistic large chemical systems and to the related chemical physics, the framework provided by the code PARAGAUSS is also suitable to investigate problems related to fundamental aspects of DFT. This is possible by the variety of exchange-correlation functionals that have been implemented in PARAGAUSS.

The main goal of the present work is to implement some commonly used variants of the DFT + U methodology that are relevant to molecular calculations and to carry out evaluatory applications which can identify various manifestations of the subtle artifacts introduced in KS density functional calculations. For solid-state problems, the DFT + U methodology has been proven to be successful in combination with plane-wave based approaches [20]. The present work represents the first implementation of the DFT + U methodology in the linear combination of Gaussian-type orbitals (LCGTO) framework of PARAGAUSS which are more suitable for molecular calculations [25].

1.2 Applications

The unifying theme of the applications performed during this thesis work is to investigate the artifacts introduced by approximate XC functionals in a KS-DFT calculation of systems with f electrons and to identify the manifestations of the self-interaction error in various chemical properties of lanthanide and actinide systems [25–27].

In solid state calculations, the DFT + U methodology is often invoked to describe electrons that are localized on atomic centers. The $3d$ orbitals of transition metal oxides or $4f$ orbitals of rare earth complexes show such *quasi-atomic* localization. The Coulomb correlation is strong

between these localized electrons thus these systems are known as strongly correlated systems [28]. The molecular systems studied in this thesis can be categorized into three types according to the localized nature of the f electrons they contain:

1. Highly localized $4f$ electron systems which show negligible intra/inter atomic hybridization. For example, lanthanide complexes with La III (f^0), Gd III (f^7), Lu III (f^{14}) ions belong to this category. Magnetic moments of these systems correspond to a $4f^n$ configuration of trivalent lanthanides; in an ionic formulation of the bonding, the valence $6s^2$ and $5d^1$ electrons are transferred to the ligands. With a formal $4f^n$ configuration, the $4f$ orbitals in Ln^{3+} systems do not participate in bonding with ligands.

2. $4f$ electron systems which show valence transitions. The oxides of cerium belong to this category where the Ce III (f^1) ion can be oxidized to Ce IV (f^0) state. In the trivalent state, the $4f^1$ electron is localized on the Ce atom but in the tetravalent state along with the $6s^2$ and $5d^1$ electrons, the $4f^1$ electron can form the bonds to the oxygen centers.

3. Semi-localized $5f$ electron systems which show non-negligible intra/inter atomic hybridization. The $5f$ orbitals of these systems are radially less compact when compared to $4f$ orbitals of lanthanides, hence they can be involved in σ and π interaction with ligands. The early members of the actinides U, Np and Pu belong to this category.

1.3 Overview of the Thesis

Chapter 2 presents the theoretical background of the KS-DFT formalism along with a brief discussion of related concepts (Sections 2.1 and 2.2). Certain inherent limitations of the commonly used approximate XC functionals which form the motivation for schemes such as DFT + U are summarized in Section 2.3.

In Chapter 3, an overview of the underlying theory of the DFT + U methodology is presented (Section 3.1). Specific details about the variant of the DFT + U methodology which has been used in this work are given in Section 3.2. The major steps in the implementation of the DFT + U methodology in PARAGAUSS are summarized in Section 3.3 along with a brief discussion of the nature of DFT + U corrections to total electronic and orbital energies.

Chapter 4 summarizes the computational methods used in this work (Sections 4.1). Section 4.2 briefly outlines a procedure followed in this work to empirically estimate the onsite-Coulomb parameter along with a listing of these parameters used in this work.

Chapters 5 and 6 are devoted to the application of the DFT + U methodology as a tool to probe self-interaction artifacts in KS-DFT calculations of f-electron systems. Chapter 5 deals

with the application of the DFT + U methodology to Lanthanide systems. In Section 5.1, results of a DFT + U investigation of the role of $4f$ orbitals in the bonding of LuF_3 are presented. Some brief remarks on the structural features of the lanthanide trifluoride molecules are summarized in Section 5.2. Preliminary results of a DFT + U investigation to model ceria nano-particles are presented in Section 5.3.

Chapter 6 discusses the application of the DFT + U methodology to some uranyl complexes. Here, the manifestation of the self-interaction error as spurious structural distortions in LDA and GGA calculations of uranyl complexes is investigated. The first part (Section 6.1) deals with the uranyl ion in gas phase as a model system to understand the DFT + U corrections. In Section 6.2, results of a DFT + U study of the penta aqua uranyl complex are presented. Finally, in Section 6.3, results of a systematic study of the uranyl monohydroxide cation are summarized.

Chapter 2

Kohn–Sham Density Functional Theory

In the previous chapter, an overview from an historical perspective was given to electron density as a suitable quantity to compute molecular properties. The idea of computing the electron density from a suitably defined set of orbitals dates back to Schrödinger's definition [5] of electron density ρ and from Hartree's works on atomic systems. The Hohenberg–Kohn theorems show that the ground state density ρ_0 uniquely defines the system Hamiltonian and that it is possible to apply the variational principle to calculate the properties of a system from ρ_0. The Kohn–Sham formalism of density functional theory (KS-DFT) actually leads to a *practical* way for constructing orbitals to obtain the ground state electron density ρ_0 and to a build the system Hamiltonian. In the present chapter, the theoretical background of KS-DFT is summarized. For more complete and general discussions related to the content of the present chapter, one is referred to [8, 10, 29, 30].

In Section 2.1, the background of KS-DFT is presented. In Section 2.2 certain concepts regarding a generalization of KS-DFT are briefly discussed, followed by some theoretical ideas regarding the interpretation of KS-DFT. Section 2.3 exclusively discusses the limitations of certain approximations to KS-DFT by considering the H atom as an example.

2.1 The Kohn–Sham Method

2.1.1 Background

The first Hohenberg–Kohn (HK) theorem [9] states that the ground-state electron density $\rho_0(\mathbf{r})$ uniquely describes all properties of the electronic ground state of a system. The second HK theorem gives a variational procedure to calculate the ground state electronic energy E_0 of a

system through the constrained minimization of the energy functional $E[\rho]$

$$E_0 = \min_{\rho \to N} \left(E[\rho] \right), \tag{2.1}$$

where the energy functional $E[\rho]$ is defined as the sum of a system dependent term due to the nuclei-electron interaction $V_{Ne}[\rho]$ and a *universally valid* functional which is independent of the number of electrons and the nuclear environment $F[\rho]$

$$E[\rho] = V_{Ne}[\rho] + F[\rho]. \tag{2.2}$$

The universal density functional $F[\rho]$ of the electronic system defined in the HK theorem is hypothetical without an explicit definition. Some generalizations can however be made about $F[\rho]$; it is a sum of contributions due to kinetic energy T and electron-electron interaction V_{ee}

$$F[\rho] = T[\rho] + V_{ee}[\rho], \tag{2.3}$$

where V_{ee} can be further divided into contributions due to the uncorrelated *classical* Coulomb energy term $J[\rho]$ and sum of *non-classical* (purely quantum mechanical) and *many-body* electrostatic effects $G[\rho]$

$$V_{ee}[\rho] = J[\rho] + G[\rho]. \tag{2.4}$$

Thus the total electronic energy functional $E[\rho]$ can be written in the following form

$$E[\rho] = V_{Ne}[\rho] + T[\rho] + J[\rho] + G[\rho]. \tag{2.5}$$

Among the various terms in the above equation, analytic forms are known only for the nuclei-electron interaction term $V_{Ne}[\rho]$ and the classical Coulomb energy term $J[\rho]$ where as analytic expressions for $T[\rho]$ and $G[\rho]$ are not known.

The nuclei-electron interaction term $V_{Ne}[\rho]$ is defined as the integral

$$V_{Ne}[\rho] = \int \rho(\mathbf{r}) v_{ext}(\mathbf{r}) d^3\mathbf{r}, \tag{2.6}$$

where the kernel of the integral is the external potential $v_{ext}(\mathbf{r})$ which is the local Coulomb potential at the position $\mathbf{r}$ due to the charges of M nuclei. In atomic units, $v_{ext}(\mathbf{r})$ is expressed as

$$v_{ext}(\mathbf{r}) = -\sum_{A=1}^{M} \frac{Z_A}{|\mathbf{r} - \mathbf{R}_A|}, \tag{2.7}$$

where Z_A and $\mathbf{R}_A$ charge and the position of nucleus A. The classical Coulomb energy contribution $J[\rho]$ to the electron-electron interaction is defined as

$$J[\rho] = \frac{1}{2} \int \frac{\rho(\mathbf{r})\rho(\mathbf{r}')}{|\mathbf{r} - \mathbf{r}'|} d^3\mathbf{r} d^3\mathbf{r}'. \tag{2.8}$$

The term $J[\rho]$ is referred to as the uncorrelated classical Coulomb energy term because this term discards the condition that within the point mass approximation, no two electrons with same spin can simultaneously be located at the same space. Thus the term $J[\rho]$ does not capture all the effects due to the $1/r_{12}$ form of the Coulomb operator. Thus the contribution due to many-body Coulomb interaction are included along with non-classical electrostatic effects through the term $G[\rho]$ in Eq. (2.4).

Among the various contributions to the *universal* functional $F[\rho]$, a significant contribution comes from the kinetic energy term $T[\rho]$. In the earlier framework of Thomas–Fermi model [7, 31, 32], the kinetic energy functional has the form

$$T[\rho] = \int \rho^{5/3}(\mathbf{r}) d^3\mathbf{r}, \tag{2.9}$$

which resulted in too large a positive energy contribution in molecular calculations rendering molecules unstable [33]. Subsequent investigations lead to better kinetic energy functionals which however came with their own short-comings [34]. At present, studies that aim at modelling better kinetic energy functional as a *pure*-density functional contribute to the so-called *orbital-free density functional theory* [35].

2.1.2 The Kohn–Sham Approach

The Kohn–Sham (KS) approach to density functional theory introduces *orbitals*. The purpose of introducing orbitals is two-fold: they are used to compute the ground state electron density ρ_0 and to provide a framework to compute the kinetic energy functional $T[\rho]$. For this purpose, W. Kohn and L. J. Sham [12] introduced the idea of a reference system of *non-interacting electrons* that are influenced by a *local effective potential* $v_{eff}(\mathbf{r})$. This effective potential is chosen such that the system of N non-interacting electrons exhibits the same ground state density ρ_0 as the real system of interacting electrons. The Hamiltonian operator that defines the system of non-interacting electrons is defined as a sum of one-electron Hamiltonian operators

$$\hat{H}_S = \sum_i^N \hat{h}_i^{KS}, \tag{2.10}$$

where the one-electron Hamiltonian operator is defined as

$$\hat{h}_i^{KS} = -\frac{1}{2}\nabla_i^2 + v_{eff}(\mathbf{r}_i). \tag{2.11}$$

The *exact* wavefunction of non-interacting electrons is a Slater determinant Φ_S, which for an N-electron system is defined as

$$\Phi_S = \frac{1}{\sqrt{N!}} \begin{vmatrix} \phi_1(\mathbf{x}_1) & \phi_2(\mathbf{x}_1) & \dots & \phi_N(\mathbf{x}_1) \\ \phi_1(\mathbf{x}_2) & \phi_2(\mathbf{x}_2) & & \phi_N(\mathbf{x}_2) \\ \vdots & \vdots & & \vdots \\ \phi_1(\mathbf{x}_N) & \phi_2(\mathbf{x}_N) & \dots & \phi_N(\mathbf{x}_N) \end{vmatrix}, \tag{2.12}$$

where $\phi_i(\mathbf{x}_i)$ are the spin-orbitals which can be expressed as a product of spatial ($\mathbf{r}$) and spin (σ) dependent factors

$$\phi_i(\mathbf{x}) = \psi_i(\mathbf{r})\omega_i(\sigma). \tag{2.13}$$

The spatial functions $\psi_i(\mathbf{r})$ are eigenfunctions of the so-called KS equations. The spin-polarized version of the KS are written as

$$\hat{h}_i^{KS,\sigma}\psi_i^\sigma(\mathbf{r}) = \varepsilon_i^\sigma \psi_i^\sigma(\mathbf{r}), \tag{2.14}$$

which are similar to Fock equations in the Hartree–Fock (HF) formalism. From the KS orbitals spin densities are computed as

$$\rho^\sigma(\mathbf{r}) = \sum_i^{N^\sigma} |\psi_i^\sigma(\mathbf{r})|^2, \tag{2.15}$$

where the summation is done over the N^σ lowest spin orbitals. The above equation can also be written by introducing the occupation number n_i^σ of the spatial orbitals as

$$\rho^\sigma(\mathbf{r}) = \sum_i n_i^\sigma |\psi_i^\sigma(\mathbf{r})|^2, \tag{2.16}$$

now the summation index i runs over all the spatial orbitals and not restricted to the N^σ lowest spin orbitals. When n_i^σ is restricted to take the integer values 0 or 1, the formalism is similar to the HF approach. Further, when the occupation numbers of the lowest N^σ spatial orbitals take the value 1, and others 0, the density $\rho^\sigma(\mathbf{r})$ corresponds to the ground state. The total electron density due to both spin densities is then the sum

$$\rho(\mathbf{r}) = \sum_\sigma \rho^\sigma(\mathbf{r}). \tag{2.17}$$

The kinetic energy of the system of N non-interacting electrons is then computed formally as in the HF approximation as

$$T_S[\rho] = \sum_\sigma \sum_i^{N^\sigma} \left\langle \psi_i^\sigma(\mathbf{r}) \left| -\frac{1}{2}\nabla_i^2 \right| \psi_i^\sigma(\mathbf{r}) \right\rangle. \tag{2.18}$$

In the above equation the summation is performed over N^σ lowest occupied orbitals of both spin types. Eq. (2.18) can be generalized by introducing the occupation numbers as

$$T_S[\rho] = \sum_\sigma \sum_i n_i^\sigma \left\langle \psi_i^\sigma(\mathbf{r}) \left| -\frac{1}{2}\nabla_i^2 \right| \psi_i^\sigma(\mathbf{r}) \right\rangle. \tag{2.19}$$

The approximate kinetic energy term $T_S[\rho]$ which is the kinetic energy of N non-interacting electrons is not equal to the kinetic-energy of N interacting electrons [10]

$$T_S[\rho] \leq T[\rho]. \tag{2.20}$$

In KS-DFT, the difference between the true kinetic energy $T[\rho]$ and the non-interacting kinetic energy $T_S[\rho]$ along with the non-classical electrostatic contribution in Eq. (2.4) are collectively defined as the *exchange-correlation functional*

$$E_{xc} = T[\rho] - T_S[\rho] + G[\rho]. \tag{2.21}$$

The exchange-correlation (XC) functional $E_{xc}[\rho]$ can be written as a sum of *exchange* $E_x[\rho]$ and *correlation* $E_c[\rho]$ functionals as

$$E_{xc}[\rho] = E_x[\rho] + E_c[\rho]. \tag{2.22}$$

The exact form of the exchange functional $E_x[\rho]$ (as functional of the orbitals) is that of a single determinant as in the HF approximation:

$$E_x = -\frac{1}{2}\sum_{\sigma}\sum_{i,j}^{N^\sigma}\left\langle \psi_i^\sigma(\mathbf{r})\psi_j^\sigma(\mathbf{r}')\left|\frac{1}{|\mathbf{r}-\mathbf{r}'|}\right|\psi_j^\sigma(\mathbf{r})\psi_i^\sigma(\mathbf{r}')\right\rangle \tag{2.23}$$

or by introducing the occupation numbers as in the kinetic energy term, Eq. (2.18)

$$E_x = -\frac{1}{2}\sum_{\sigma}\sum_{i,j} n_i^\sigma n_j^\sigma\left\langle \psi_i^\sigma(\mathbf{r})\psi_j^\sigma(\mathbf{r}')\left|\frac{1}{|\mathbf{r}-\mathbf{r}'|}\right|\psi_j^\sigma(\mathbf{r})\psi_i^\sigma(\mathbf{r}')\right\rangle. \tag{2.24}$$

The *exchange interaction* is a purely quantum mechanical effect for which no classical analog exists. The exchange interaction is characteristic of *fermions* which follow the *Pauli exclusion principle* that the total wavefunction of two identical fermions is anti-symmetric. Similar to the HF formalism, the KS formalism introduces exchange interaction by choosing the total electronic wavefunction as a Slater determinant, Eq. (2.12). It should be noted that the wavefunctions involved in the above definition of the exchange functional are KS orbitals; thus the exchange contribution according to Eq. (2.23 or 2.24) will be exact only when the KS orbitals represent the true density.

The correlation functional $E_c[\rho]$ has no explicit analytic definition. In conventional quantum chemistry, the correlation energy is defined as the difference between the exact electronic energy and the HF energy. In the KS theory, the residual kinetic energy contribution as in Eq. (2.21) has to be provided by $E_c[\rho]$ along with the many body Coulomb correlation effects. Thus within the KS-DFT formalism, the total electronic energy functional is written as

$$E[\rho] = V_{Ne}[\rho] + T_S[\rho] + J[\rho] + E_{xc}[\rho]. \tag{2.25}$$

The local effective potential that enters into the one-electron Hamiltonian operator in Eq. (2.11) is defined as

$$v_{eff}^{\sigma}(\mathbf{r}) = v_{ext}(\mathbf{r}) + v_H(\mathbf{r}) + v_{xc}^{\sigma}(\mathbf{r}), \tag{2.26}$$

where the external potential term is simply written according to Eq. (2.7) and the Hartree potential of a charge density $v_H(\mathbf{r})$ and the XC are defined as the *functional derivatives* [8]

$$v_H(\mathbf{r}) = \frac{\delta}{\delta\rho} J[\rho] = \int \frac{\rho(\mathbf{r}')}{|\mathbf{r}-\mathbf{r}'|} d^3\mathbf{r}' \tag{2.27}$$

and

$$v_{xc}^{\sigma}(\mathbf{r}) = \frac{\delta}{\delta\rho^{\sigma}} E_{xc}[\rho]. \tag{2.28}$$

The effective potential is already dependent on the density through the Hartree potential in Eq. (2.27) and the XC potential in Eq. (2.28). Thus the KS equations according to Eq. (2.11) have to be solved self-consistently.

2.1.3 Approximate Exchange-Correlation Functionals

The XC energy $E_{xc}[\rho]$ is usually expressed in terms of the XC energy density or XC energy per electron $\varepsilon_{xc}[\rho]$ as

$$E_{xc}[\rho] = \int \rho(\mathbf{r}) \varepsilon_{xc}[\rho](\mathbf{r}) d^3\mathbf{r}, \tag{2.29}$$

where the term $\varepsilon_{xc}[\rho]$ which acts as the integration kernel can be written as the sum

$$\varepsilon_{xc}[\rho] = \varepsilon_x[\rho] + \varepsilon_c[\rho]. \tag{2.30}$$

KS-DFT is in principle exact when the XC functional employed is exact. However, the analytic form of the XC functional is not known and therefore it has to be approximated for practical calculations.

2.1.3.1 Local Density Approximation

A simple, yet highly successful approximation is the *local density approximation* (LDA) [8, 10, 12, 36]. Here, the XC energy density at position $\mathbf{r}$ is the XC energy density of a homogeneous electron gas of the same electron density at that local density

$$\varepsilon_{xc}[\rho](\mathbf{r}) \approx \varepsilon_{xc}^{LDA}(\rho(\mathbf{r})) \tag{2.31}$$

In the following, a brief description is given for some of the commonly used LDA XC functionals. The simplest LDA XC functional is the Slater–Dirac exchange functional (SD) [37, 38], where ε_x has a dependency of $\rho^{1/3}$. The spin-specific variant of SD exchange is sometimes called as the

local spin density approximation (LSDA) exchange. The SD exchange for the statistical LDA exchange is normally used along with a term to account for correlation contribution. Vosko, Wilk, and Nusair [40] gave a correlation functional (VWN) by fitting the data of a Monte-Carlo simulation [41] of uniform electron gas. The VWN correlation term is usually referred to as LSDA correlation. Perdew and Wang gave an improved correlation functional (PW) through a different parametrization [42]. When both VWN and PW LDA correlation functionals are used along with SD exchange functional, the XC functionals are commonly referred to as VWN and PW-LDA respectively. The most severe drawback of the LDA is the systematic overestimation of binding energies, hence resulting in rather short bond lengths.

2.1.3.2 Generalized Gradient Approximation

An improved approximation is the so-called *generalized gradient approximation* (GGA) in which $\varepsilon_{xc}[\rho](\mathbf{r})$ is a function of both the density, $\rho(\mathbf{r})$ and the absolute value of the gradient of the density, $\nabla\rho(\mathbf{r})$ at position $\mathbf{r}$.

$$\varepsilon_{xc}[\rho](\mathbf{r}) \approx \varepsilon_{xc}^{GGA}(\rho(\mathbf{r}), |\nabla\rho(\mathbf{r})|) \tag{2.32}$$

Some of the commonly used GGA XC functionals are BP (X: B88, Becke, 1988 [43], C: P86, Perdew, 1986 [44]), PW91 (XC: Perdew–Wang, 1991 [45]), PBE (XC: Perdew–Burke–Ernzerhof, 1996 [46]) and PBEN (X: PBE, C: Hammer–Hansen–Nørskov, 1999 [47]). As corresponding LDA XC functionals for the above listed GGA XC functionals, BP includes the VWN functional while PW91, PBE and PBEN include the PW-LDA XC functional.

2.1.3.3 Higher Approximations

Better XC functionals are aimed at providing an improved description beyond that of GGA XC functionals. A class of XC functionals that also accounts for the Laplacian or the second derivative of the electron density are classified as meta-GGA functionals (mGGA). Evaluation of the Laplacian of the electron density may lead to numerical instabilities, hence the effect of the second derivative of the electron density is often approximately introduced in the form of the orbital kinetic energy density. One such mGGA XC functional is the TPSS (Tao–Perdew–Staroverov–Scuseria) XC functional [48]. All the three types of approximations – LDA, GGA and mGGA— are also referred to as *semi-local* approximations because in these approximations the XC energy density (ε_{xc}) at a position $\mathbf{r}$ is a function of the electron density (ρ) at the position $\mathbf{r}$ and its infinitesimal neighborhood.

A *non-local* XC functional includes wholly or partly the exact non-local exchange functional as defined in Eq. (2.23). These functionals are also known as hyper-GGA functionals. When

these hyper-GGA functionals include only a fraction of the exact exchange functional, they are also known as *hybrid-DFT* XC functionals. Two commonly used hybrid-DFT XC functionals are B3LYP (Becke 3-parameter Lee–Yang–Parr) [49–51] and PBE0 [52]. The B3LYP XC functional is defined as

$$E_{xc}^{B3LYP} = E_x^{SD} + 0.20\left(E_x^{exact} - E_x^{SD}\right) + 0.72\left(E_x^{B88} - E_x^{SD}\right) + 0.81\left(E_c^{LYP} - E_c^{VWN}\right) \quad (2.33)$$

where all the constituting exchange and correlations functionals have been defined previously except for the LYP-GGA correlation functional which is due to Lee, Yang and Parr [50]. The hybrid DFT functional PBE0 [52] functional has a much simpler composition

$$E_{xc}^{PBE0} = 0.75E_x^{PBE} + 0.25E_x^{exact} + E_c^{PBE}. \quad (2.34)$$

It should be noted that in the hyper-GGA level, only the exchange contribution has a non-local contribution while the correlation contribution is from a semi-local functional.

The random phase approximation (RPA) [53] provides a fully non-local approximation to the correlation energy which can be used along with the exact exchange term to get a fully non-local exchange-correlation energy. Thus commonly used exchange-correlation functionals can be categorized as five levels of approximation (LDA, GGA, mGGA, hyper-GGA, RPA) as suggested by Perdew and Schmidt [54].

2.2 Generalization and Interpretation of Kohn–Sham Theory

2.2.1 Non-Integer Orbital Occupation Numbers

The KS-DFT formalism can be generalized by defining the occupation numbers n_i^σ of the KS spin-orbitals ϕ_i^σ also to take values between 0 and 1: $0 \leq n_i^\sigma \leq 1$.

Perdew, Parr, Levy and Balduz justified [59] the non-integer occupation extension of KS-DFT by generalizing KS-DFT to *zero temperature grand canonical ensembles* where the ground state of a system with a non-integer number of electrons $N+n$, is an ensemble mixture of the system at two of its ground states with integer number of electrons N and $N+1$. Here, the variable n is the spin-specific occupation number n_i^σ of the highest occupied molecular orbital (HOMO) of an N-electron system i.e. n_{HOMO}^σ. Thus the ground state energy of a system with $N+n$ electrons where $0 \leq n \leq 1$, is a linear combination of energies of the pure ground states with N and $N+1$ electrons:

$$E_{N+n}^0 = (1-n)\,E_N^0 + nE_{N+1}^0, \quad (2.35)$$

and the ground state density can then be written as the ensemble sum

$$\rho_{N+n}^0 = (1-n)\,\rho_N^0 + n\rho_{N+1}^0. \quad (2.36)$$

Introduction of non-integer occupations provides a way to generalize KS-DFT to *finite-temperature grand canonical ensembles* where the mean value of N is considered to be a continuous variable [36, 60, 61]. In extended molecular systems or solids, the total number of electrons N may be considered as a continuous variable only for practical convenience, hence introducing non-integer occupations in KS-DFT provides a way to calculate properties such as the band structure with a total number of electrons N slightly varying from the integer value [36].

2.2.2 Scaling Relations for Density Functionals

The ensemble form of the energy functional E^0_{N+n} as defined in Eq. (2.35) varies linearly with respect to the continuous variable n between the integer number of electrons N and $N+1$. For an n-electron system at ground state, where N and corresponding energy and density are zero, Eq. (2.35) and Eq. (2.36) can be written as:

$$E^0_n = nE^0_1 \tag{2.37}$$

and

$$\rho^0_n = n\rho^0_1. \tag{2.38}$$

The scaling behavior of individual contributions to the energy functional $E[\rho]$ of an n electron system, were given by Zhang and Yang [62–64] as

$$T_{S,n} = nT_{S,1}, V_{Ne,n} = nV_{Ne,1} \quad \text{and} \quad J_n = n^2 J_1, \tag{2.39}$$

where the contributions due to the non-interacting kinetic energy T_S and the external potential V_{Ne} both scale linearly as the total energy functional, Eq. (2.35), the classical Coulomb term scales quadratically. For the XC contribution E_{xc}, Zhang and Yang gave the scaling relation

$$E_{xc,n} = n(1-n)J_1 + nE_{xc,1}. \tag{2.40}$$

and pointed out that approximate XC functionals violate this scaling behavior. In the above equation, Eq. (2.40), for the values $n = 0$ or $n = 1$, the first term on the right hand side vanishes. On the other hand, for fractional values of n, the exchange-correlation functional $E_{xc,n}$ comprises a *penalty* contribution of the form $n(1-n)$. It should be noted that the scaling relations for $T_{S,n}$, $V_{Ne,n}$ and J_n according to Eq. (2.39) can be easily derived but the scaling relation for the XC contribution, Eq. (2.40) is non-trivial and it was presented in Ref. [64] without proof. However it is easy to see that the $n(1-n)$ term ensures cancellation of both the quadratic self-Coulomb term and the linear self-exchange term for any n when $J_1 = -E_{xc,1}$, Eq. (2.40).

2.2.3 Orbital Energies

The energy of a *vertical* electronic transition (without reorganization of nuclear framework) between two states can be calculated as the difference between the total energies of corresponding states involved in the transition. In the HF approximation this leads to *Koopmans theorem* [65], according to which the vertical ionization energy to remove an electron from a HF spin orbital (ϕ_i^σ) can be approximated as the negative of the corresponding orbital energy

$$I_i \approx E_{N-1}(n_i^\sigma = 1) - E_N(n_i^\sigma = 0) = -\varepsilon_i^\sigma. \tag{2.41}$$

An extension of Koopmans theorem for fractional occupation numbers which is valid in KS-DFT is called Slater–Janak theorem [66], according to which KS orbital energies are derivatives of the total energy functional with respect to corresponding occupation numbers:

$$\frac{dE[\rho]}{dn_i^\sigma} = \varepsilon_i^\sigma. \tag{2.42}$$

By comparing Eq. (2.41) and Eq. (2.42), one can realize that Koopmans theorem may be viewed as a finite difference analogue of the Slater-Janak theorem. Since the ground state energy E^0 in KS-DFT varies linearly with respect to the spin polarized occupation number of the HOMO, Eq. (2.35), it is clear that both the exact derivative of $E^0[\rho]$, Eq. (2.42), and finite derivative variant using an arbitrary step size $0 \leq n \leq 1$, Eq. (2.41), are equal. Thus in KS-DFT, the negative of ε_{HOMO} can be approximated to the first ionization potential

$$I \approx -\varepsilon_{HOMO}^\sigma. \tag{2.43}$$

An extension of the above equation to orbitals that are below the HOMO is only restricted by the fact that Hohenberg–Kohn–Sham theory is a ground state theory within which Eq. (2.43) can be justified while removal of an electron from an orbital below the HOMO involves an excited state. It should be noted that the Slater-Janak theorem, Eq. (2.42) is valid even when the exchange-correlation functional employed in a calculation is approximate while Eq. (2.43) is valid only when E^0 is a linear function of n_{HOMO}^σ which is the case only when the exchange-correlation functional is exact.

Another concept which is extremely useful in KS-DFT, especially when approximate XC functionals are employed, is *Slater's transition state* [1] which was originally proposed within the Hartree–Fock–Slater (HFS) approximation [39]. For a system with an orbital occupation number n_i^σ for an orbital ϕ_i^σ, Slater expanded $E[\rho]$ as a power series of $E[\rho]$ of a system with $n_i^\sigma = 1/2$

$$E[\rho]|_{n_i^\sigma} = E[\rho]|_{n_i^\sigma = 1/2} + \left.\frac{dE[\rho]}{dn_i^\sigma}\right|_{n_i^\sigma = 1/2} (n_i^\sigma - 1/2) + \ldots. \tag{2.44}$$

Using the above equation and Slater-Janak theorem, Eq. (2.42), ionization of orbital ϕ_i^σ involves a transition from a state with $n_i^\sigma = 1$ to a state with $n_i^\sigma = 0$. The resulting energy change can then be approximated as

$$E[\rho]|_{n_i^\sigma=1} - E[\rho]|_{n_i^\sigma=0} \approx \left.\frac{dE[\rho]}{dn_i^\sigma}\right|_{n_i^\sigma=1/2} = \varepsilon_i^\sigma|_{n_i^\sigma=1/2}\,. \tag{2.45}$$

The above equation is an approximation because contributions from higher order derivatives are ignored. According to Eq. (2.45), the ionization energy can be approximated as the negative of the orbital energy of the orbital from which half an electron is removed. This species with an half-electron is called Slater's transition state. In KS-DFT, Eq. (2.45) is normally used in ground state calculations where the transition state involved is the half-filled HOMO.

2.3 Self-interaction Error

2.3.1 Conditions for Exact Exchange-Correlation Functionals

A KS calculation will yield exact results only when the (unknown) exact XC functional would be employed. The exact XC functional satisfies certain conditions, some of which are violated by approximate XC functionals that are based on LDA and GGA. Often it is possible to define these exact conditions only for certain limiting cases or model systems. One such case is that of a one-electron system, e.g. the H atom; the single electron cannot interact with itself through the Coulomb interaction. For this system the contribution to the total energy due to Coulomb interaction (Eq. 2.3) should be zero:

$$E_{ee}[\rho^\sigma] = 0; \quad \int \rho^\sigma(\mathbf{r})d\mathbf{r} = 1. \tag{2.46}$$

When Eq. (2.46) is not satisfied, the Coulomb interaction in the one electron system is non-vanishing resulting in *self-interaction* (SI) and the error introduced due to SI is called the *self-interaction error* (SIE).

The HF theory is free of SI. For every individual HF orbital, Eq. (2.46) is satisfied in the HF theory. In the general spin-polarized unrestricted HF (UHF) approach, the total electron-electron interaction V_{ee} can be expressed as the sum of contributions due to occupied spin orbitals of both spin type as

$$E_{ee} = \frac{1}{2}\sum_a^{N^\alpha}\sum_b^{N^\alpha}\left(J_{ab}^{\alpha,\alpha} - K_{ab}^{\alpha,\alpha}\right) + \frac{1}{2}\sum_a^{N^\beta}\sum_b^{N^\beta}\left(J_{ab}^{\beta,\beta} - K_{ab}^{\beta,\beta}\right) + \sum_a^{N^\alpha}\sum_b^{N^\beta} J_{ab}^{\alpha,\beta}, \tag{2.47}$$

where J and K are the Coulomb and exchange integrals [55]. The E_{ee} contribution to the UHF total energy of a single electron system can be written as

$$\frac{1}{2}\left(J_{11}^{\sigma,\sigma} - K_{11}^{\sigma,\sigma}\right) = 0. \tag{2.48}$$

In the HF approximation, the self-Coulomb and self-exchange of a single electron are evaluated as the same integral and they cancel each other.

In KS-DFT, E_{ee} is a sum of Coulomb and XC contributions

$$E_{ee} = J[\rho] + E_{xc}[\rho], \tag{2.49}$$

where the Coulomb contribution $J[\rho]$ is the classical Coulomb term as defined in Eq. (2.8) and the XC contribution $E_{xc}[\rho]$ is calculated according to Eq. (2.29). For a single electron density of a given spin, Eq. (2.49) yields

$$J[\rho^\sigma] + E_{xc}[\rho^\sigma] = 0. \tag{2.50}$$

For a single-electron, the correlation contribution is also zero. Thus, cancellation of self-Coulomb energy should be due to the self-exchange term. Thus Eq. (2.50) can be written as the two separate conditions

$$J[\rho^\sigma] + E_x[\rho^\sigma] = 0 \tag{2.51}$$

and

$$E_c[\rho^\sigma] = 0. \tag{2.52}$$

Collectively the above two equations are referred to as conditions for the KS formalism to be free of SI defined for a one-electron spin density which are satisfied by the exact XC functional. The orbital energies are the eigenvalues of the KS Hamiltonian matrix where the electron-electron contribution enter through the Hartree, Eq. (2.27), and the XC, Eq. (2.28), potentials as variational derivatives. Thus, in order for the KS orbital energies to be SI free, the exact condition for the local potentials can be given as

$$v_H(\mathbf{r}) + v_{xc}(\mathbf{r}) = 0. \tag{2.53}$$

The above follows from two separate conditions

$$v_H(\mathbf{r}) + v_x(\mathbf{r}) = 0 \tag{2.54}$$

and

$$v_c(\mathbf{r}) = 0. \tag{2.55}$$

Approximate XC functionals according to LDA and GGA do not satisfy the SI conditions for total energies, Eq. (2.51, 2.52) and local potentials Eq. (2.54, 2.55), but only to some approximation. This situation has been discussed for the HFS approximation (or the X_α method) where it is relatively simple to demonstrate that minimization of the SI cannot be simultaneously for the total energy and the effective one-electron potential. Rather, the parameter denoted by α that enters into the exchange term requires different parametrizations for each purpose, for the total energy and the orbital energies [39, 56, 57]. While the SIE can be analytically defined only for a one-electron system, it is also present in the LDA/GGA calculations of many-electron systems.

2.3.2 Self-Interaction Cancellation by Semi-Local Functionals

For a one-electron system the SIE in the total energy is not a serious problem in certain LDA and all GGA approximations where Eq. (2.50) is sufficiently satisfied because of certain error cancellations between exchange and correlation contributions. However the SIE is severe for the orbital energy of a one-electron system where Eq. (2.53) is not satisfied to a sufficient accuracy in both LDA and GGA approximations. In the following, the performance of some commonly used LDA and GGA functionals in terms of self-interaction cancellation is discussed for the hydrogen atom.

Table 2.1: Total electronic energy (E) and energy of 1s orbital (ε_{1s}) of a hydrogen atom in various LDA and GGA [a] exchange-correlation (XC) functionals along with exact values. All values are in eV.

Approximation	XC	E	ε_{1s}
LDA	SD	–12.437	–6.719
LDA	VWN	–13.025	–7.319
LDA	PW-LDA	–13.026	–7.320
GGA	BP	–13.609	–7.621
GGA	PW91	–13.647	–7.653
GGA	PBE	–13.605	–7.594
GGA	PBEN	–13.749	–7.644
Exact/UHF [b]		–13.606	–13.606

[a] In the DFT calculations, an uncontracted basis set of the size (8s, 4p, 3d) was employed.
[b] The exact value is –0.5 hartree.

Table 2.1 presents the total energy and the energy of the 1s orbital of the H atom in spin-polarized KS-DFT calculations employing various commonly used LDA and GGA XC functionals along with exact values. For the H atom, the UHF total energy of –13.61 eV (–0.5 hartree) is exact. The LDA calculation employing the exchange-only SD functional predicts the total energy to be about -12.4 eV which differs from the exact value by about 1.2 eV. When VWN or PW-LDA XC functionals are employed the total energy of the H atom is much improved but still differs from the exact value by 0.6 eV. All the GGA XC functionals BP, PW91, PBE and PBEN improve the total energy towards the exact value. The energy of the 1s orbital for which the exact value is same as that of the total energy –13.61 eV is incorrectly predicted by all LDA and GGA functionals shown (Table 2.1). The difference between the exact value and the SD value is about

6.9 eV which is slightly reduced to about 6.3 eV by VWN and PW-LDA XC functionals. The GGA functionals improve ε_{1s} to –7.6 eV which still differs from the exact value by about 6 eV. Overall the total energy of the H atom is predicted to sufficient accuracy by LDA functionals that include both exchange and correlation contributions and by all the GGA functionals. However, the magnitude of the orbital energy is significantly underestimated by 6 to 7 eV by all the LDA and GGA functionals discussed here (Table 2.1).

The error introduced in LDA and GGA KS-DFT calculations of the H atom is exclusively due to incomplete self-interaction cancellation in the one-electron potential by LDA and GGA XC functionals. In order to understand even approximately the magnitude of the SIE in the total energy and the orbital (HOMO) energy of a one-electron system, a measure of the exchange-correlation contribution by the LDA and GGA XC functionals is needed. In this aspect, the scaling relations given by Yang and others [64] form an important step towards understanding the nature of the SIE in KS calculations employing approximate functionals. Accordingly, the Coulomb contribution of an n-electron system, where $0 \leq n \leq 1$, scales as

$$J_n = n^2 J_1, \tag{2.56}$$

while the scaling relation for the *exact* exchange-correlation contribution is

$$E_{xc,n}^{exact} = n(1-n)J_1 + nE_{xc,1}^{exact}. \tag{2.57}$$

The exchange-correlation energy contribution due to LDA and GGA XC functionals to a sufficient accuracy takes the form

$$E_{xc,n}^{LDA/GGA} \approx nE_{xc,1}^{LDA/GGA} \approx -nJ_1 \tag{2.58}$$

and by comparing Eq. (2.57) and Eq. (2.58) it is clear that part of the exact behavior which is not accounted by LDA and GGA XC functionals is the contribution due to the penalty functional of the type $n(1-n)J_1$.

For the total energy contribution of a one-electron system ($n = 1$) to a good approximation, the self-Coulomb energy is cancelled by the LDA/GGA self-exchange-correlation energy

$$\text{SIE in } E[\rho^{\sigma}] = J_1 + E_{xc,1}^{LDA/GGA} \approx 0. \tag{2.59}$$

The above equation simply means that the LDA and GGA XC contribution varies approximately linearly with respect to n while the Coulomb contribution varies quadratically, hence they cancel each other when $n = 1$ and in the trivial case where $n = 0$. Using the Slater-Janak theorem [66] according to Eq. (2.42), it is easy to see that self-interaction cancellation is not sufficient in the energy of the HOMO of the one-electron system

$$\text{SIE in } \varepsilon_{HOMO} = 2J_1 + E_{xc,1}^{LDA/GGA} \approx J_1. \tag{2.60}$$

According to the above equation it is clear that the Coulomb energy contribution to orbital energy of a one-electron system is approximately twice the Coulomb contribution to the total energy. Since the XC contribution varies linearly with n, the SIE in the orbital energy is approximately equal to J_1, which is in fact the case of H atom where the energy of the 1s orbital is approximately -7.5 eV in LDA and GGA calculations which differ from the exact value of -13.6 eV by about -6 eV.

Table 2.2 presents the contributions to the total energy and 1s orbital energy of H atom due to the classical Coulomb term $J[\rho]$ and due to the exchange E_x and correlation E_c contributions. For the H atom, the exact ground state density is $\rho_0(\mathbf{r}) = e^{-2r}/\pi$ and the classical Coulomb contribution $J[\rho]$ can be analytically evaluated to 5/16 hartree (8.504 eV) [58]. In an exact KS-DFT calculation or in UHF, the self-Coulomb contribution to the total energy is exactly cancelled by the self-exchange term hence resulting in complete self-interaction cancellation. The SIE is largest in the SD-LDA calculation where the self-Coulomb energy of 8 eV is only partly cancelled by the SD exchange contribution of –7 eV resulting in SIE of about 1 eV. With the inclusion of correlation effects the LDA approximations VWN and PW-LDA slightly reduces the SIE in the total energy due to an error cancellation. For a one-electron system, the exact correlation contribution is zero, but the VWN and PW-LDA XC functionals predict about –0.6 eV of correlation contribution which decreases the SIE to about 0.6 eV. The GGA functionals provide almost correct amount of exchange and correlation contributions and decrease the SIE in energy and the error cancellation between exchange and correlation contributions is also decreased. Also one notes that with improved XC contributions, the classical Coulomb contribution improves from 8.0 eV in the SD-LDA method to about 8.4 eV in GGA methods approaching the exact value of 8.5 eV. Overall the general conclusion can be drawn that the SIE in the total energy of a H atom is rather small and Eq. (2.59) is approximately satisfied in KS-DFT calculations employing commonly used LDA (VWN, PW-LDA) and GGA functionals.

The contributions to the 1s orbital energy due to Coulomb and exchange-correlation energies, enter via the local potentials. The UHF values for Coulomb and exchange contribution are obtained using the Koopmans theorem [65], hence they are the same as the corresponding contributions to the total energy of the H atom. In an exact KS-DFT, the quadratic Coulomb energy contribution to the total energy is $J_n = n^2 J_1$, where $n = 1$. The contribution to the orbital energy according to Slater–Janak theorem [66] is obtained as the corresponding derivative with respect to n. Thus the Coulomb energy contribution to ε_{1s} is $2J_1 = 17.007$ eV and the exact exchange-contribution is obtained using Eq. (2.57) as $-2J_1 = -17.007$ eV. The classical Coulomb contribution to ε_{1s} in LDA calculations is about 14 eV which improves by 0.5 eV in GGA calculations. The XC contribution to ε_{1s} in LDA and GGA calculations is approximately

Table 2.2: Contributions to the total electronic energy (E) and the energy of the 1s orbital (ε_{1s}) of the hydrogen atom in LDA and GGA approximations employing various exchange-correlation (XC) functionals along with exact values: classical Coulomb energy J, exchange energy E_x, correlation energy E_c. All values are in eV.

Quantity	Approximation	XC	J	E_x	$J+E_x$	E_c	$J+E_{xc}$
E	LDA	SD	8.015	–6.891	1.124	0.000	1.124
	LDA	VWN	8.119	–6.977	1.141	–0.589	0.552
	LDA	PW-LDA	8.119	–6.977	1.142	–0.590	0.551
	GGA	BP	8.335	–8.290	0.046	–0.062	–0.016
	GGA	PW91	8.361	–8.249	0.112	–0.172	–0.060
	GGA	PBE	8.349	–8.211	0.138	–0.155	–0.017
	GGA	PBEN	8.395	–8.402	-0.007	–0.156	–0.163
	Exact/UHF [a]		8.504	–8.504	0.000	0.000	0.000
ε_{1s} [b]	LDA	SD	13.804	–7.328	6.476	0.000	6.476
	LDA	VWN	14.049	–7.472	6.577	–0.604	5.974
	LDA	PW-LDA	14.050	–7.473	6.577	–0.604	5.973
	GGA	BP	14.417	–8.364	6.053	–0.216	5.837
	GGA	PW91	14.489	–8.425	6.064	–0.243	5.821
	GGA	PBE	14.458	–8.363	6.095	–0.224	5.870
	GGA	PBEN	14.536	–8.456	6.079	–0.225	5.854
	UHF [c]		8.504	–8.504	0.000	0.000	0.000
	Exact [d]		17.007	–17.007	0.000	0.000	0.000

[a] Exact values: $J = J_1 = 5/16$ hartree and $E_x = -J_1$ hartree.

[b] In LDA and GGA calculations, various contributions to ε_{1s} were obtained according to the Slater–Janak theorem as the numerical derivative $\varepsilon_{1s} = \left(E_H - E_{H^{0.0001+}}\right)/0.0001$. Here the numerator is the difference between corresponding contributions to the total energy.

[c] UHF the contribution to ε_{1s} are obtained according to Koopmans theorem as the finite difference $\varepsilon_{1s} = (E_H - E_{H^+})/1$.

[d] The exact KS-DFT value is obtained using the Slater–Janak theorem: $J = 2J_1 = 5/8$ hartree, $E_x = -J_1$ hartree

similar to the corresponding contributions to the total energy, indicating the fact that LDA and GGA XC contributions vary linearly. The contribution due to the correlation energy is zero in an exact calculation. LDA and GGA functionals contribute about –0.6 eV and –0.2 eV of correlation energy respectively which slightly cancel the self-Coulomb contribution. Overall, the SIE in ε_{1s} of the H atom in LDA and GGA calculations is about 6 eV.

The contribution to the total energy and ε_{1s} of H atom due to kinetic T and nucleus-electron attraction V_{Ne} energies are listed in Table 2.3. Both in LDA and GGA calculations, T and V_{Ne} contributions to the total energy are close to exact values. However, the large SIE in ε_{1s} of about 6–7 eV of self-Coulomb energy partially shields the electron from the nucleus resulting in an underestimation of the external potential by about 6 eV which variationally decreases also the kinetic energy contribution by 6 eV. However by error cancellation, the sum of T and V_{Ne} contributions to ε_{1s} approximately satisfy the virial theorem $-2T/V_{Ne} = 1$ hartree $= -13.6$ eV.

Using the scaling relations of the Coulomb and XC functionals, the *self-interaction analysis*

Table 2.3: Contributions to the total electronic energy (E) and the energy of the 1s orbital (ε_{1s}) of the hydrogen atom in LDA and GGA approximations employing various exchange-correlation (XC) functionals along with exact values: Kinetic energy T, electron-nuclear attraction V_{Ne}. All values are in eV.

Quantity	Approximation	XC	T	V_{Ne}	$T+V_{Ne}$
E	LDA	SD	12.436	–25.998	–13.562
	LDA	VWN	12.697	–26.274	–13.577
	LDA	PW-LDA	12.697	–26.275	–13.577
	GGA	BP	13.367	–26.959	–13.593
	GGA	PW91	13.505	–27.093	–13.587
	GGA	PBE	13.463	–27.051	–13.588
	GGA	PBEN	13.609	–27.195	–13.586
	Exact/UHF [a]		13.606	–27.211	–13.606
ε_{1s} [b]	LDA	SD	6.720	–19.915	–13.196
	LDA	VWN	6.981	–20.275	–13.294
	LDA	PW-LDA	6.982	–20.276	–13.294
	GGA	BP	7.305	–20.764	–13.459
	GGA	PW91	7.455	–20.929	–13.474
	GGA	PBE	7.401	–20.866	–13.465
	GGA	PBEN	7.455	–20.954	–13.499
	Exact/UHF [a]		13.606	–27.211	–13.606

[a] Exact values: $T = 0.5$ hartree and $V_{Ne} = -1.0$ hartree.

[b] In LDA and GGA calculations, various contributions to ε_{1s} were obtained according to the Slater–Janak theorem as the numerical derivative $\varepsilon_{1s} = \left(E_H - E_{H^{0.0001+}}\right)/0.0001$. Here the numerator is the difference between corresponding contributions to the total energy.

done above for a H atom can be generalized to an n-electron case, where $0 \leq n \leq 1$. The self-interaction cancellation in the total energy and the orbital energy of such a fractionally charged H atom with n-electron in LDA and GGA calculations are qualitatively illustrated in Figure 2.1 and Figure 2.2, respectively. It has to be noted that the assumption in these figures is that for a H atom with in the occupation numbers 0 and 1, the classical Coulomb energy contribution scaled quadratically as n according to Eq. (2.56) and the exchange-correlation contribution varies linearly as n according to Eq. (2.58) which are only approximately valid in LDA and GGA.

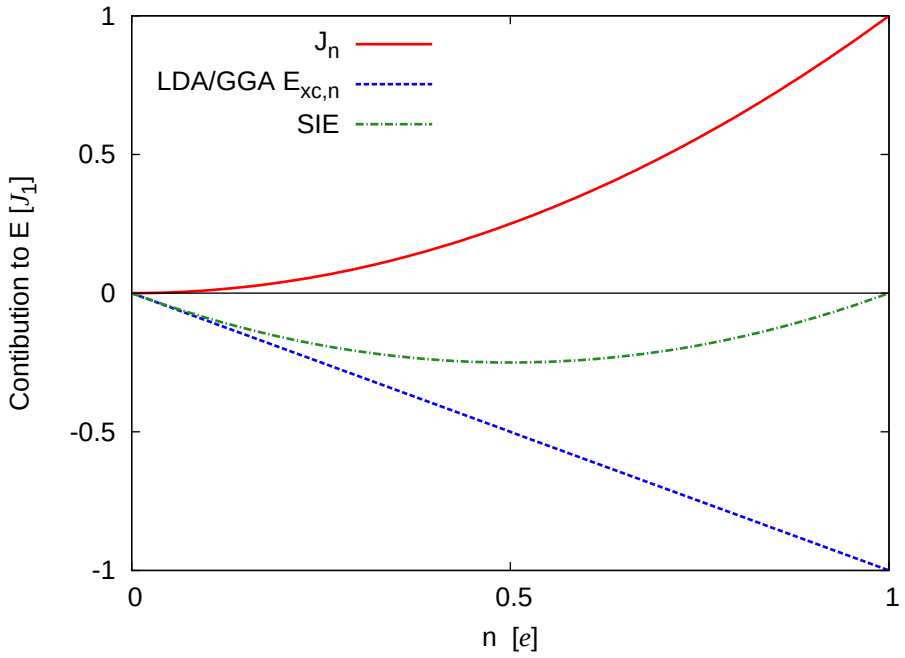

Figure 2.1: Qualitative illustration of the self-interaction cancellation in the total energy by typical LDA/GGA XC functionals for a fractionally charged H atom with n-electron, where $0 \leq n \leq 1$ according to Eq. (2.56, 2.58). Contributions to $E[\rho]$ due to the classical Coulomb J_n energy and the LDA/GGA XC energy $E_{xc,n}$ in units of classical Coulomb contribution of the single electron in H atom, J_1.

From Figure 2.1 one notes that for an n-electron H atom, the SIE in the total energy is due to the underestimation of the Coulomb repulsion and is largest (in absolute terms) when $n = 0.5$ where the absolute value of the SIE is $J_1/4$, where J_1 is the classical Coulomb contribution to the one electron energy, 5/16 hartree in the case of the H atom. From Figure 2.2 one notes that for the fractionally charged H atom, that the SIE of ε_{HOMO} is due to an underestimation of the classical Coulomb repulsion when $0 \leq n \leq 0.5$, and overestimated when $n > 0.5$; for $n = 0.5$ the self-Coulomb energy in this model is completely cancelled by the self-exchange contribution. For $n = 1.0$, the absolute value of the SIE in ε_{HOMO} is equal to J_1.

The conclusions drawn from the analysis of the self-interaction cancellation in the present

section for a general fractionally charged n-electron system can be easily extended to $N+n$ electron systems such as multi-electron atoms. The results of these analyses provide some guidelines about the approximate magnitude of the SIE which one can expect in a KS-DFT calculation when LDA and GGA XC correlation functionals are employed.

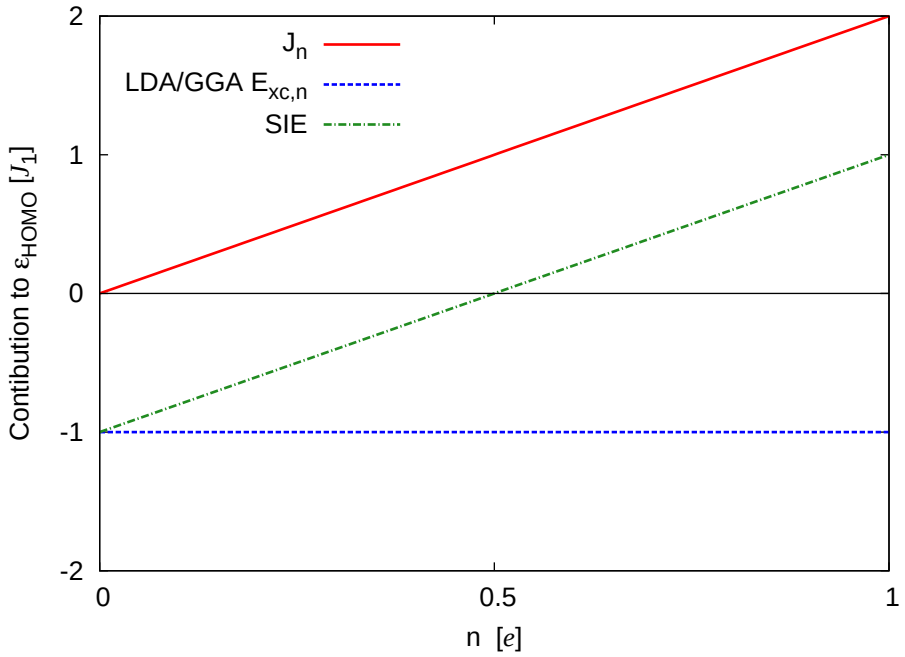

Figure 2.2: Qualitative illustration of the self-interaction cancellation in the energy of the HOMO by typical LDA/GGA XC functionals for a fractionally charged H atom with n-electron, where $0 \leq n \leq 1$ according to derivatives of Eq. (2.56, 2.58). Contributions to ε_{HOMO} due to the classical Coulomb J_n energy and the LDA/GGA XC energy $E_{xc,n}$ (from the corresponding local potentials) in units of classical Coulomb contribution of the single electron in H atom, J_1.

2.3.3 Manifestations of the Self-Interaction Error

The self-interaction error (SIE) which is introduced into KS-DFT calculations employing approximate XC functionals (such as LDA, GGA) arises because of the incomplete cancellation of the self-Coulomb contribution by the self-exchange contribution. SIE in KS orbital energies in LDA and GGA calculations is a simple case of how SIE manifests itself in a property other than the total electronic energy. Certain system specific manifestations of the SIE in LDA and GGA methods have been widely discussed and have been classified as failures of common LDA and GGA XC functionals in describing these systems [14, 15]. Some of the notable failures of LDA and GGA methods are the underestimation of reaction barriers, the underestimation of band gaps, the prediction of wrong dissociation limits of molecules such as H_2^+, the prediction of wrong excitation energies of certain transition metal atoms, wrong orbital energies of atomic

and molecular systems especially the destabilization of the HOMO of anions such as hydride, fluoride, etc. and overstabilization of HOMO of cations. All these situations can be understood as due to the SIE in total energies, orbital energies or both.

The incorrect prediction of the energy of the H atom (Table 2.1) is also one of the failures of LDA and GGA methods. However as discussed in the previous section, the magnitude of this error is rather small at least in GGA methods. Moreover, the absolute electronic energy is not an observable quantity and chemically relevant properties such as the geometry or the energetics are functions of energy differences. If one considers that the main source of error in LDA and GGA calculations is due to wrong quadratic behavior of classical Coulomb contribution (or the linear behavior of exchange contribution), one can semi-quantitatively understand the magnitude of the SIE in total energies and orbital energies from Figures 2.1 and 2.2.

A good example to illustrate the SIE in molecular systems is the LDA/GGA description of the hydrogen molecular cation, H_2^+ at the dissociation limit which shows the SIE in both total energy and orbital energy. Before proceeding further, certain aspects LDA/GGA calculation of H_2^+ at large bond lengths need to be discussed.

The proper dissociation product of H_2^+ is a H^+ ion and a neutral H atom. However when symmetry constraints are enforced such that the two H atoms are identical, the dissociation product is considered to be two separated $H^{0.5+}$ ions. In an exact theory which is size-consistent, both the dissociation products will have same energy.

However in LDA and GGA, two separated $H^{0.5+}$ ions are predicted to be more stable than the dissociation products H^+ and a neutral H atom. The preference for the wrong dissociation of H_2^+ in LDA and GGA is due to the underestimation of the Coulomb energy of two $H^{0.5+}$ ions which results in an overstabilization of this dissociation product.

From Figure 2.1, one can see that both H^+ and H which have 0 and 1 electron respectively are relatively free of SIE when compared to two $H^{0.5+}$ ions with fractional electrons. For a system with half an electron the classical Coulomb term is evaluated as $J_{0.5} = J_1/4$ which is about 2.1 eV (where $J_1 = 5/16$ hartree = 8.5 eV) and E_{xc} is evaluated as $E_{x,0.5} = -J_1/2$ which is about –4.2 eV (Figure 2.1). Hence for two $H^{0.5+}$ ions one can expect $J = 4.2$ eV, $E_{xc} = -8.4$ eV and a SIE of about –4.2 eV. In a PBE calculation of the energy of a $H^{0.5+}$ ion, J and E_{xc} are calculated as 2.3 and –3.9 eV, respectively, with a SIE of –1.6 eV. Thus for two $H^{0.5+}$ ions the SIE in PBE method is about 3.0 eV which is same amount by which the PBE binding energy differs from the exact UHF value at the dissociation limit (r > 100 Å).

Figure 2.3 shows the binding energy curves of H_2^+ in UHF, VWN-LDA and PBE-GGA methods. For this one-electron system, the UHF description is exact. LDA and GGA methods predict the equilibrium bond length of H_2^+ very accurately to be about 1 Å in good agreement with UHF.

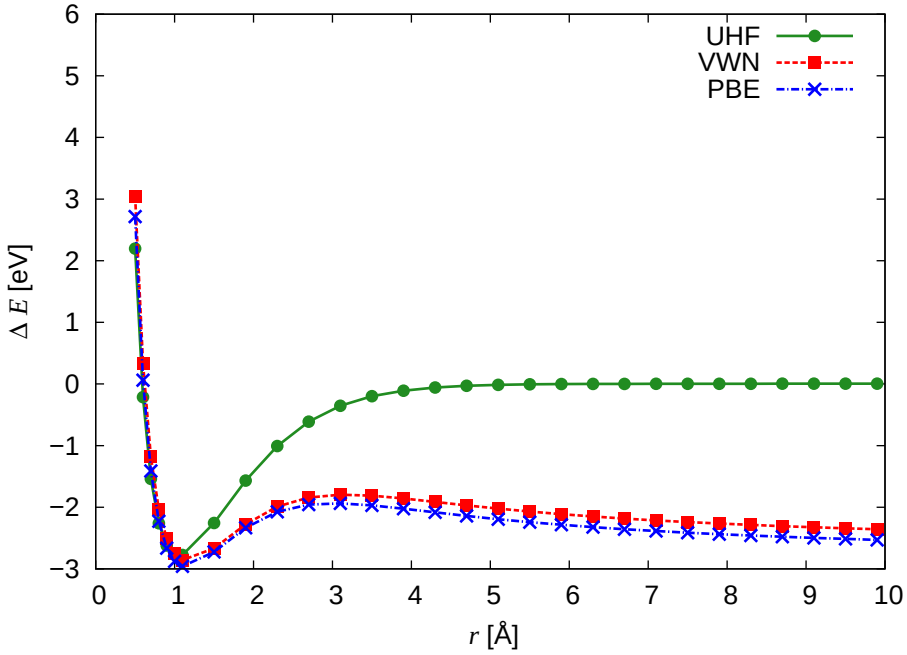

Figure 2.3: Binding energy curves of H_2^+ in UHF, VWN-LDA and PBE-GGA methods. The binding energy is calculated as $\Delta E = E(H_2^+) - E(H) - E(H^+)$. DFT calculations were performed by enforcing symmetry restrictions in which both H nuclei are identical.

LDA, GGA binding energy of H_2^+ is also very close to the exact UHF value at the equilibrium bond length, however at large separations, LDA and GGA energies are too negative and H_2^+ molecule is overstabilized. This situation has been widely discussed in the literature [14, 67]. In Ref. [14], Yang et al. points out that the error in the energy of H_2^+ at dissociation limits is due to SIE due to fractional charges which result in the underestimation of the Coulomb energy.

Without symmetry constraints, LDA and GGA calculations of H_2^+ at large bond distance normally do not converge. This is a consequence of the SIE of the orbital energy. From Figure 2.2, one can see that ε_{HOMO} of H^+ is underestimated and ε_{HOMO} of neutral H is overestimated by J_1. Such a situation entails that the electron localized on the H atom favors to transfer to the 1*s* orbital of the H^+ center which ultimately results in SCF oscillations. It is however possible to favor the localized dissociation product by fixing a electron-hole in one of the H centers, but this will only represent an excited state.

H_2^+ is an interesting system for studying effects of the SIE in semi-local KS calculations. The SIE of the total energy of H_2^+ illustrates why LDA and GGA methods wrongly favor localized solutions while the SIE in orbital energy illustrates convergence issues and issues related to under or overestimation of orbital energies.

2.3.4 Self-Interaction Correction Schemes

From the overall discussions in this chapter so far, it is perhaps evident that an obvious way to proceed in order to account for self-interaction correction (SIC) in approximate KS-DFT calculations is to employ better XC functionals. In this respect, the hybrid-DFT XC functionals such as B3LYP [49–51] and PBE0 [52] that include a fraction of exact exchange similar to HF scheme are expected to lead to improved results.

Developing better semi-local functionals that are also free of SIE requires a thorough analysis of the performance of semi-local methods such as LDA and GGA for simple and fully understood atomic or molecular systems. In this respect, Yang et al. suggested [64] to model XC functionals such that they satisfy Eq. (2.40) in a simpler way by including a penalty functional of the type $n(1-n)J$ in the exchange functional. For fractional occupation numbers, the classical Coulomb contribution is underestimated. Thus the residual Coulomb contribution is provided in the form of a penalty functional which provides a positive correction only when n is fractional. As discussed in the previous sections, such a correction term will automatically provide the SIC needed for KS orbital energies.

In order to improve the already existing semi-local XC functionals, Perdew and Zunger provided a strategy which is commonly known as the SIC-DFT scheme [15]. In this approach, the spurious self-interaction which is the sum of self-Coulomb and self-exchange contributions is subtracted out from the energies of the occupied KS orbitals. Such a scheme ignores error cancellation between the exchange and correlation energy contributions (Table 2.2) and it has been found to be inaccurate for molecules near the equilibrium geometry [68].

The SIC-DFT potential unlike the KS potential is orbital-dependent providing orbital specific corrections. In the optimized effective potential (OEP) approach [69], exact exchange contribution is included but the KS potential is optimized by varying the orbital occupation numbers.

The present thesis work deals with a SIC strategy that uses the DFT + U methodology [20]. The DFT + U approach introduces an orbital dependent correction term to the energy functional $E[\rho]$ according to the generalized Hubbard Hamiltonian. The DFT + U methodology is usually employed for solid state systems with localized electrons. However, this scheme can be also be used for atomic calculations where the orbitals are trivially localized on atoms, for cases like H_2^+ at the dissociation limit where one can expect localization of the single electron on one of the centers and for systems with localized $3d$ or $4f$ electrons where these electrons due to their compact radial distribution are localized on atomic centers even on molecules and solids. Among various variants of the DFT + U methodology, an approach known as FLL-DFT + U (fully localized limit DFT + U) [20] introduces an energy correction term in the form of the penalty functional as in Eq. (2.40) – for specific atomic shells – which provides a Coulomb

contribution for fractional charges and suitably corrects the KS potential to improve the orbital energies.

Chapter 3

The DFT + U Methodology

From the discussions in the previous chapter, it is evident that the magnitude of the SIE present in KS-DFT calculations employing LDA and GGA XC functionals is larger for orbital energies than for total energies. In the case of a H atom when the orbital occupation number is exactly one, the SIE in ε_{1s} is largest resulting in a net destabilization of the $1s$ orbital of H atom (see Figure 2.2). The $3d$ orbitals of transition metals and $4f$ orbitals of lanthanides do not have large radial extension and in compounds formed by these metals, the $3d$ or $4f$ orbitals do not form strong overlaps with the ligand orbitals and they are more localized on the corresponding atoms. Thus when these localized orbitals are occupied, they have integer orbital occupation numbers (i.e. 1 electron per orbital). Thus the orbital energies of $3d$ or $4f$ systems suffer from severe self-interaction error in LDA and GGA calculations. This phenomenon is responsible for the simple case where LDA and GGA incorrectly predict the ground state of atomic Ni to have the configuration $3d^9 4s^1$ instead of the correct configuration $3d^8 4s^2$. A more common situation is the underestimation of band gaps of transition metal oxides in LDA and GGA solid state calculations. Transition metal oxides such as NiO, CoO, and $CaCuO_2$ are antiferromagnetic (AFM) insulators with sufficiently large energy gap between the valence and conduction bands. KS-DFT methods employing semi-local XC functionals such as LDA and GGA severely underestimate the band gap and the magnetic moments and predict these metal oxides to be metallic [70]. The DFT + U methodology was first proposed [20] in order to improve the DFT description of these systems.

The present chapter summarizes the details of the DFT + U methodology which is the main topic of the present work. In section 3.1, the theoretical background of the DFT + U formalism is presented which is followed by section 3.2 where the expressions that are used in the DFT + U method are presented. Section 3.3 deals with the specific details related to the implementation of the DFT + U methodology in the program PARAGAUSS. Finally in section 3.4, a brief analysis of the correction provided by the widely used variant of the DFT + U correction is discussed by

considering C atom as a simple example.

3.1 The DFT + U Formalism

In semi-empirical band structure calculation of solids, approximations given by the generalized Hubbard model [71, 72] leads to an effective Hamiltonian to treat the bevahior of electrons in metals. In the Hubbard model, the electron-electron repulsion of electrons on a site/atom of a metal is quantified by the onsite-Hubbard parameter U. The Anderson model [71], more commonly known as the Anderson impurity model is based on the Hubbard model but allows the treatment of localized, magnetic states of an impurity present in a non-magnetic material. In band structure calculations, such a scheme ensures separate treatments for highly localized d or f electrons and less localized s and p electrons. Motivated by the success of the Anderson model Anisimov et al. [20] suggested that the LSDA description of transition metal oxides such as NiO can be improved by adding an orbital occupation dependent energy correction term to the DFT energy functional in order to exclusively improve the electron-electron description of the $3d$ electrons. This resulted in the formulation of the DFT + U approach, originally intended to improve the LSDA description, in which a screened Hartree-Fock type electron-electron description if provided for the localized electrons such as $3d$ and $4f$ electrons. There have been several implementations of the DFT + U methodology in solid state electronic structure codes in the framework of linear muffin-tin orbitals (LMTO) [20], full-potential linearized augmented plane-wave (FLAPW) [73], projector augmented-wave (PAW) [74] pseudopotential-plane-wave [75], full-potential local orbitals (FPLO) [76] and linear-combination-of-pseudo-atomic-orbital (LCPAO) [77] methods. The present work represents the first implementation of the DFT + U in the framework of symmetry adapted *linear combination of contracted Gaussian-type orbitals* (LCCGTO) framework of the program PARAGAUSS [21,22] which is more suitable for molecular calculations [25–27].

The DFT + U total energy functional is given as the sum of DFT total energy functional and a correction term which depends on the orbital occupation numbers of a given *shell* of orbitals

$$E^{\mathrm{DFT+U}}[\rho, n_s] = E^{\mathrm{DFT}}[\rho] + E^{\mathrm{U}}[n_s], \tag{3.1}$$

where n_s refers to the occupation numbers of a particular shell of orbitals. If the DFT + U treatment is intended for the $3d$ orbitals of a single Ni atom, then a shell denoted by s can be defined as the five $3d$ orbitals of each spin type and n_s will the set of occupation numbers of the $3d$ orbitals. In the symmetry adapted LCCGTO framework of PARAGAUSS, a *shell* corresponds to a unique atom index u, the angular momentum quantum number l of the orbitals and the

contraction number c. Thus the shell index s can be mapped to the indices $[u, L, c]$:

$$s \equiv [u, L, c] \tag{3.2}$$

Thus in the more general symmetry adapted case, the total number of orbitals belonging to a shell is $N_{eq}(2l+1)$ where N_{eq} is the number of atoms belonging to a unique type u. While the energy correction term is shell specific, it has to be noted that such corrections can be provided separately to more that one shell of orbitals of the specified unique atom. The second term in the right hand side (r.h.s.) of Eq. (2.1) is the DFT + U energy correction which has the form

$$E^{\mathrm{U}}[n_s] = E_0^U[n_s] - E^{dc}[n_s], \tag{3.3}$$

where the first term on the r.h.s. is a term derived according to the UHF treatment of the electron-electron interaction of electrons within the shell s and the second term is a *double counting* term which represents the electron-electron interaction contribution of the shell s that is already present in the DFT total energy functional from the contributions of classical Coulomb and exchange-correlation functionals.

3.1.1 The DFT + U Functional form

According to UHF, the contribution to the total energy due to electron-electron interaction is given according to Eq. (2.4). For the present purpose, it is useful to consider an expression for the electron-electron interaction energy obtained by the expanding the spin-specific molecular orbitals ψ_i^σ as a linear combination of the atomic basis functions $\{\phi_\mu\}$

$$\psi_i^\sigma = \sum_\mu C_{\mu i}^\sigma \phi_\mu. \tag{3.4}$$

In terms of the linear expansion coefficients $C_{\mu i}^\sigma$, the elements of a density matrix can now be defined as

$$D_{\mu\nu}^\sigma = \sum_i n_i^\sigma C_{\mu i}^\sigma C_{\nu i}^{\sigma,*}, \tag{3.5}$$

where n_i^σ is the occupation number of the molecular orbital ψ_i^σ.

The standard expression for the electron-electron interaction energy in the basis $\{\phi_\mu\}$ is given by [72]

$$E_{ee}^{UHF} = \frac{1}{2}\sum_\sigma \sum_{\mu\nu\lambda\eta} \left[(\mu\nu|\eta\lambda) D_{\nu\mu}^\sigma D_{\lambda\eta}^{-\sigma} + \{(\mu\nu|\eta\lambda) - (\mu\lambda|\eta\nu)\} D_{\nu\mu}^\sigma D_{\lambda\eta}^\sigma \right] \tag{3.6}$$

where the indices μ, ν, λ, η run over all the basis functions. The four center integrals $(\mu\nu|\eta\lambda)$ that enter Eq. (3.6) are defined as [55]

$$(\mu\nu|\eta\lambda) = \int d\vec{r}_1 d\vec{r}_2 \phi_\mu^*(\vec{r}_1)\phi_\nu(\vec{r}_1) r_{12}^{-1} \phi_\eta^*(\vec{r}_2)\phi_\lambda(\vec{r}_2). \tag{3.7}$$

In arriving at the expression for E_0^{U} in Eq. (3.3) from the expression for the energy contribution due to electron-electron interaction in the UHF formalism as given in above equation, the following approximations are invoked.

Approximations involved in the DFT + U formalism

- Energy correction is meant only for a specified shell s as defined in Eq. (2.4). Thus the atomic basis function indices μ, ν, η and λ correspond to indices of the $N_{eq}(2l+1)$ orbitals of this shell.

- As in the case of semi-empirical schemes such as the Hubbard model, the electron-electron repulsion operator is replaced by an operator representing screened electron-electron repulsion between electrons in the given shell. Thus the *screened* Coulomb and exchange integrals

$$U_{\mu,\nu,\eta,\lambda} = \int d\vec{r}_1 d\vec{r}_2 \phi_\mu^*(\vec{r}_1)\phi_\nu(\vec{r}_1)\hat{V}_{ee}^{scr}\phi_\eta^*(\vec{r}_2)\phi_\lambda(\vec{r}_2) \tag{3.8}$$

  and

$$J_{\mu,\lambda,\eta,\nu} = \int d\vec{r}_1 d\vec{r}_2 \phi_\mu^*(\vec{r}_1)\phi_\lambda(\vec{r}_1)\hat{V}_{ee}^{scr}\phi_\eta^*(\vec{r}_2)\phi_\nu(\vec{r}_2) \tag{3.9}$$

  which replace the four center integrals that enter Eq. (3.7).

- The DFT + U correction term was originally proposed for the tight binding linear muffin tin orbitals where the diagonal elements of the density matrix **D** will give the orbital occupation numbers n_i^σ. Irrespective of the basis set involved, in the atomic limit of localization, the orbitals that belong to given shell s do not mix among themselves.

The DFT + U energy correction term E_0^{U} is obtained by invoking the above mentioned approximations in Eq. (3.6)

$$E_0^{\mathrm{U}} = \frac{1}{2}\sum_\sigma \sum_{\mu\nu\lambda\eta\in s} \left[U_{\mu,\nu,\eta,\lambda} n_\mu^\sigma n_\eta^{-\sigma} \delta_{\mu\nu}\delta_{\lambda\eta} + \left(U_{\mu,\nu,\eta,\lambda} - J_{\mu,\lambda,\eta,\nu}\right) n_\mu^\sigma n_\eta^\sigma \delta_{\mu\nu}\delta_{\lambda\eta} \right], \tag{3.10}$$

where the orbital occupation numbers n_i^σ enter in an *ad hoc* fashion which needs to be defined separately. After simplification, Eq. (3.10) can be written as

$$E_0^{\mathrm{U}} = \frac{1}{2}\sum_\sigma \sum_{\mu\eta\in s} \left[U_{\mu,\mu,\eta,\eta} n_\mu^\sigma n_\eta^{-\sigma} + \left(U_{\mu,\mu,\eta,\eta} - J_{\mu,\eta,\eta,\mu}\right) n_\mu^\sigma n_\eta^\sigma \right]. \tag{3.11}$$

In the HF formalism, self-interaction is implicit, where a self-Coulomb energy term is cancelled exactly by a self-exchange term. This aspect is also reflected in Eq. 3.11 where $U_{\mu,\mu,\mu,\mu} = J_{\mu,\mu,\mu,\mu}$, thus Eq. 3.11 can be presented as

$$E_0^{\mathrm{U}} = \frac{1}{2}\sum_\sigma \sum_{\mu\eta\in s} \left[U_{\mu,\mu,\eta,\eta} n_\mu^\sigma n_\eta^{-\sigma} \right] + \frac{1}{2}\sum_\sigma \sum_{\mu\neq\eta\in s} \left[\left(U_{\mu,\mu,\eta,\eta} - J_{\mu,\eta,\eta,\mu}\right) n_\mu^\sigma n_\eta^\sigma \right]. \tag{3.12}$$

Spherically averaged Coulomb and exchange terms

The DFT + U scheme is easy to implement as a semi-empirical correction term where the difficulties related to defining the screened Coulomb operator $\hat{V}_{ee}^{scr}$ operator and computing the four center integrals are alleviated by introducing these integrals as suitably defined parameters. Within a shell $s \equiv [u, L, c]$ with $N_{eq}(2l+1)$ orbitals, there will be $\left[N_{eq}(2l+1)\right]^2$ Coulomb terms of the form $U_{\mu,\mu,\eta,\eta}$ and $N_{eq}^2[2l(2l+1)]$ terms of the form $\left(U_{\mu,\mu,\eta,\eta} - J_{\mu,\eta,\eta,\mu}\right)$ where self-interaction cancellation between Coulomb and exchange terms with identical indices are taken into account. In a spherical charge distribution or when the shell *s* is filled, spherically averaged onsite-Coulomb and onsite-exchange terms can be defined as

$$\overline{U} = \frac{1}{\left[N_{eq}(2l+1)\right]^2} \sum_{\mu\eta \in s} U_{\mu,\mu,\eta,\eta} \tag{3.13}$$

and

$$\overline{U} - \overline{J} = \frac{1}{N_{eq}^2[2l(2l+1)]} \sum_{\mu \neq \eta \in s} \left(U_{\mu,\mu,\eta,\eta} - J_{\mu,\eta,\eta,\mu}\right). \tag{3.14}$$

After introducing spherically averaged Coulomb and exchange terms in Eq. (3.12) one arrives at the functional form

$$E_0^{\mathrm{U}} = \frac{1}{2}\overline{U} \sum_{\sigma} \sum_{\mu\eta \in s} n_\mu^\sigma n_\eta^{-\sigma} + \frac{1}{2}\left(\overline{U} - \overline{J}\right) \sum_{\sigma} \sum_{\mu \neq \eta \in s} n_\mu^\sigma n_\eta^\sigma. \tag{3.15}$$

There is no unique way to compute the spherically averaged onsite-Coulomb and onsite-exchange terms $\overline{U}$ and $\overline{J}$. They are often employed in DFT + U calculations as empirical parameters to fit observable quantities [97, 98]. In the earlier DFT + U applications, $\overline{U}$ and $\overline{J}$ were approximated using Slater integrals [70, 99]. An *ab-initio* approach to compute these terms using Coulomb and exchange integrals from an UHF calculation was given by Mosey et al. [95, 96]. Alternately one can approximately compute these parameters through constrained DFT calculations which also accounts for screening and relaxation effects [70, 100–102].

Fully localized limit DFT + U functional form

The total DFT + U correction term depends on two terms, Eq. (3.3), of which the first term is defined according to Eq. (3.15). The second term on the r.h.s. of Eq. (3.3) accounts for the electron-electron interaction contribution of the shell *s* that is already included in the DFT total energy through the contributions of classical Coulomb and exchange-correlation functionals. This contribution is separated through the double counting term E^{dc}. Various definitions of E^{dc} have been proposed based on different motivations. In the review by Ylvisaker et al. [79] the performance of different forms of E^{dc} is discussed.

One of the earlier definitions of E^{dc} is based on the fully localized limit approximation (FLL). According to the FLL approximation, in the integer occupation limit, DFT calculations employing semi-local XC functionals such as LDA and GGA, electron-electron interaction is free of self-interaction to a good approximation and hence has the correct form. Thus in the FLL limit, the double counting term E^{dc} takes form of E_0^{U} in the integer occupation limit [80]

$$E_{FLL}^{dc} = \lim_{n_s=1 \text{ or } 0} E_0^{\mathrm{U}}. \tag{3.16}$$

The FLL double counting term can be derived by introducing the following identities which are valid for integer occupation numbers in Eq. (3.15)

$$\sum_{\mu\eta\in s} n_\mu^\sigma n_\eta^{-\sigma} = N^\sigma N^{-\sigma} \quad \text{and} \quad \sum_{\mu\neq\eta\in s} n_\mu^\sigma n_\eta^\sigma = N^\sigma(N^\sigma - 1), \tag{3.17}$$

where n_μ^σ are the spin-specific occupation numbers of the orbitals of the shell s and N^σ is the total number of electrons of the spin type σ defined as

$$\sum_{\mu\in s} n_\mu^\sigma = N^\sigma. \tag{3.18}$$

Thus the FLL double counting term can be written as

$$E_{FLL}^{dc} = \frac{1}{2}\overline{U}\sum_\sigma N^\sigma N^{-\sigma} + \frac{1}{2}\left(\overline{U} - \overline{J}\right)\sum_\sigma N^\sigma(N^\sigma - 1). \tag{3.19}$$

Finally the total DFT + U correction term, in the FLL approximation can be given by using Eq. (3.19) and Eq. (3.15) in Eq. (3.3)

$$E_{FLL}^U = E_0^U - E_{FLL}^{dc}, \tag{3.20}$$

where the two terms in the r.h.s. cancel each other in the integer occupation limit and only in the non-integer occupation limit, a non-zero correction is provided. An explicit form of Eq. (3.20) can be given by subtracting Eq. (3.3) from Eq. (3.15) as

$$E_{FLL}^U = \frac{1}{2}\left(\overline{U} - \overline{J}\right)\sum_\sigma\sum_{\mu\in s}\left[n_\mu^\sigma\left(1 - n_\mu^\sigma\right)\right]. \tag{3.21}$$

The difference between spherically averaged onsite Coulomb and exchange parameters $\overline{U}$ and $\overline{J}$ can be substituted by a single *onsite-effective Coulomb repulsion* parameter U_{eff} which also simplifies as the DFT + U functional as a semi-empirical correction term that depends on a single parameter

$$E_{FLL}^U = \frac{1}{2}U_{\mathrm{eff}}\sum_\sigma\sum_{\mu\in s} n_\mu^\sigma\left(1 - n_\mu^\sigma\right). \tag{3.22}$$

It is interesting to note that the r.h.s. of the above expression has the same form as the penalty functional introduced by Yang et al. [64] as a component of an exchange functional which is

needed to provide self-interaction cancellation for fractional occupation numbers, Eq. (2.40). The FLL-DFT + U functional according to Eq. (3.21) is the most widely used DFT + U functional. This functional has been implemented in the program PARAGAUSS as a part of this thesis work and all the applications have been performed using this correction term.

Modified FLL DFT + U functional form

D. Seo proposed [81] a modified version of the FLL (mFLL) DFT + U functional form where the double counting term takes the form

$$E^{dc}_{mFLL} = \frac{1}{2}\overline{U}\sum_{\sigma} N^{\sigma}N^{-\sigma} - \frac{1}{2}\left(\overline{J}\right)\sum_{\sigma}(N^{\sigma})^2. \tag{3.23}$$

The full form of the DFT + U correction term according to the mFLL double counting term is given by

$$E^{U}_{mFLL} = -\frac{1}{2}\left(\overline{U}-\overline{J}\right)\sum_{\sigma}\sum_{\mu\in s}\left(n^{\sigma}_{\mu}\right)^2. \tag{3.24}$$

The above correction term has also been implemented in PARAGAUSS by introducing the definition $\overline{U}-\overline{J} = U_{\text{eff}}$

$$E^{U}_{mFLL} = -\frac{1}{2}U_{\text{eff}}\sum_{\sigma}\sum_{\mu\in s}\left(n^{\sigma}_{\mu}\right)^2. \tag{3.25}$$

The DFT + U functional form according to Eq. (3.25) is not commonly used and this functional was only used for exploratory calculations and for the applications discussed in this thesis, this functional was not used.

Rotationally invariant DFT + U functional forms

The DFT + U functionals according to Eq.(3.22) and Eq.(3.25) which are given in natural orbital representation are usually implemented in a *rotationally invariant* form. In a rotational invariant form, the DFT + U correction term will be invariant with respect to a unitary basis transformation. For this purpose the orbital occupation numbers n^{σ}_{μ} are introduced in the DFT + U energy correction terms, Eq.(3.22) and Eq.(3.25), in the form of an orbital occupation matrix $\mathbf{N}^{\sigma}$ which in general need not be diagonal hence accounts for overlap effects in a non-orthogonal basis:

$$\mathbf{n}^{\sigma} = \mathbf{A}^{T}\cdot\mathbf{N}^{\sigma}\cdot\mathbf{A} \tag{3.26}$$

where $\mathbf{n}^{\sigma}$ is a diagonal matrix whose diagonal elements are the occupation numbers n^{σ}_{μ} and $\mathbf{A}$ is an orthogonal transformation matrix. The orbital occupation matrix $\mathbf{N}^{\sigma}$ which enters into Eq. (3.26) is actually defined as the sub-matrix of a global orbital occupation matrix $\mathbf{P}^{\sigma}$. In other

words, the matrix $\mathbf{P}^{\sigma}$ is the orbital occupation matrix computed for the whole system and $\mathbf{N}^{\sigma}$ is the sub-section of $\mathbf{P}^{\sigma}$ that corresponds to the orbitals of the shell *s*. This can be represented as

$$\mathbf{N}^{\sigma} \Leftarrow \texttt{extract}(\mathbf{P}^{\sigma}, s). \tag{3.27}$$

The dimension of the matrix $\mathbf{N}^{\sigma}$ is the same as the number of orbitals that belong to the shell *s* which is $N_{eq}(2l+1)$, Eq. (3.2). The expression for the occupation numbers n_{μ}^{σ} can now be given in terms of the elements of $\mathbf{N}^{\sigma}$ as

$$n_{\mu}^{\sigma} = \sum_{\nu}\sum_{\eta} A_{\mu\nu}^{T}\, N_{\nu\eta}^{\sigma}\, A_{\eta\nu}. \tag{3.28}$$

The above equation is used in Eq.(3.22) and Eq.(3.25) to arrive at the rotationally invariant form of the DFT + U functionals

$$E_{FLL}^{U} = -\frac{1}{2}U_{\text{eff}} \sum_{\sigma} [\text{Tr}(\mathbf{N}^{\sigma}\cdot\mathbf{N}^{\sigma}) - \text{Tr}(\mathbf{N}^{\sigma})] \tag{3.29}$$

and

$$E_{mFLL}^{U} = -\frac{1}{2}U_{\text{eff}} \sum_{\sigma} \text{Tr}(\mathbf{N}^{\sigma}\cdot\mathbf{N}^{\sigma}). \tag{3.30}$$

3.1.2 Orbital Occupation Matrix

The DFT + U energy correction term is an orbital dependent term. Thus the magnitude of the DFT + U energy correction depends on the definition of the orbital occupation matrix **P**. The orbital occupation matrix **P** is not uniquely defined, hence various definitions of **P** have been made. This is due to the fact that there is no well defined operator for measuring the charge of an atom in a molecule. In the present implementation of the DFT + U methodology in PARAGAUSS, four definitions of **P** were considered. In the following a brief description of the various definitions of **P** are summarized followed by a comparison of the performance of these matrices.

Full occupation matrix

The *first order density matrix* is defined as

$$\rho(\mathbf{r};\mathbf{r}') = \sum_{\mu}\sum_{\nu} D_{\mu\nu}\phi_{\mu}(\mathbf{r})\phi_{\nu}^{*}(\mathbf{r}'), \tag{3.31}$$

where $\phi_{\mu}(\mathbf{r})$ is a basis function centered at position $\mathbf{r}$ and $D_{\mu\nu}$ are the elements of the density matrix as defined in Eq. (3.5). The *full occupation matrix*, $\mathbf{P}^{full}$, is defined in terms of the first order density matrix [82]

$$P_{\mu\nu}^{full} = \int\int \phi_{\mu}^{*}(\mathbf{r})\rho(\mathbf{r};\mathbf{r}')\phi_{\nu}(\mathbf{r}')d^{3}\mathbf{r}d^{3}\mathbf{r}'. \tag{3.32}$$

By substituting Eq. (3.31) in Eq. (3.32) one arrives at

$$\begin{aligned} P_{\mu\nu}^{full} &= \sum_{\eta}\sum_{\chi} D_{\eta,\chi} \int\int \phi_{\mu}^{*}(\mathbf{r})\phi_{\eta}(\mathbf{r})\phi_{\chi}^{*}(\mathbf{r}')\phi_{\nu}(\mathbf{r}')d^{3}\mathbf{r}d^{3}\mathbf{r}' \\ &= \sum_{\eta}\sum_{\chi} D_{\eta\chi} \int \phi_{\mu}^{*}(\mathbf{r})\phi_{\eta}(\mathbf{r})d^{3}\mathbf{r} \int \phi_{\chi}^{*}(\mathbf{r}')\phi_{\nu}(\mathbf{r}')d^{3}\mathbf{r}' \\ &= \sum_{\eta}\sum_{\chi} D_{\eta\chi}S_{\mu\eta}S_{\chi\nu} \\ &= \sum_{\eta}\sum_{\chi} S_{\mu\eta}D_{\eta\chi}S_{\chi\nu} \\ &= (\mathbf{S}\cdot\mathbf{D}\cdot\mathbf{S})_{\mu\nu}, \end{aligned} \tag{3.33}$$

where **S** is the overlap matrix. The full occupation matrix defined as the matrix product $\mathbf{S}\cdot\mathbf{D}\cdot\mathbf{S}$ is commonly used in DFT + U calculations [83]. The full occupation matrix is also used in the natural atomic orbital (NAO) analysis [84]. The inclusion of the overlap matrix ensures the applicability of this occupation matrix in the framework of a non-orthogonal basis functions. All the applications discussed in the present work have been done by employing the full occupation matrix.

Other definitions

When the basis functions $\{\phi_{\mu}\}$ are orthonormal, the overlap matrix **S** becomes the unit matrix. In this limit, the full occupation matrix is the density matrix **D** which in the DFT + U literature is called as the onsite occupation matrix [85]

$$\mathbf{P}^{onsite} = \mathbf{D}. \tag{3.34}$$

Both the onsite and full occupation matrices do not satisfy the sum rule that the trace of the occupation matrix is equal to the number of electrons [77]. This sum rule is satisfied by Mulliken $\mathbf{P}^{M}$ and Löwdin $\mathbf{P}^{L}$ population matrices which are defined [55] as

$$\mathbf{P}^{M} = \frac{1}{2}(\mathbf{D}.\mathbf{S} + \mathbf{S}\cdot\mathbf{D}) \tag{3.35}$$

and

$$\mathbf{P}^{L} = \mathbf{S}^{(1/2)}\cdot\mathbf{D}\cdot\mathbf{S}^{(1/2)}, \tag{3.36}$$

where the Mulliken population matrix $\mathbf{P}^{M}$, which is usually written as the matrix product $\mathbf{D}.\mathbf{S}$ is presented in the symmetrized form, Eq. (3.35).

Comparison of various orbital occupation matrices

The definition of the orbital occupation matrix restricts the applicability of the DFT + U methodology to a wide-range of systems. The DFT + U methodology is usually employed for systems

with highly localized $3d$ or $4f$ orbitals. While the restriction to $3d$ or $4f$ orbitals is motivated by the observation that LDA and GGA tend to destabilize these orbitals resulting in smaller band gaps, the physical reason for the DFT + U methodology to *work* is the localized behavior of the orbitals for which DFT + U methodology is employed. Thus one can employ the DFT + U methodology also to systems such as atoms or molecules at dissociation limit where the orbitals will be localized on atomic centers. In these cases the various definitions of the orbital occupation matrix **P** are equivalent. This restricts the applicability of the DFT + U methodology to the orbitals which form strong overlaps with the other orbitals such as $1s$ orbitals of H atom in molecules like H_2 at the equilibrium geometry.

The performance of the various definitions of **P** can be understood through some example cases. Table 3.1 presents the value of *partial traces* of **P** and $\mathbf{P}\cdot\mathbf{P}$ (that are traces of **N** and $\mathbf{N}\cdot\mathbf{N}$) that enter into the DFT + U energy correction expression, Eq. (3.22) for the molecules H_2, NH_3 and GdF_3. These partial traces were computed by extracting the sub-matrix that corresponds to the $1s$, $2p$ and $4f$ shells of H, N and Gd atoms in H_2, NH_3 and GdF_3 respectively. The first quantity which is the trace of the submatrix of **P** can be interpreted as total the number of electrons in the corresponding shells. For the number of $1s$ electrons located on the quasi-H atoms in the H_2 molecule, the Löwdin population matrix $\mathbf{S}^{(1/2)}\cdot\mathbf{D}\cdot\mathbf{S}^{(1/2)}$ gives a reasonable value of 1.8 e while the electron count using the density (onsite-occupation) matrix **D** gives 1.2 e. It is known that the total number of electrons in H_2 molecule is 2.0, hence both Löwdin and onsite-occupation matrices can possibly be accepted. For H_2, the Mulliken population matrix $\mathbf{D}\cdot\mathbf{S}$ (after symmetrization) and the full occupation matrix $\mathbf{S}\cdot\mathbf{D}\cdot\mathbf{S}$ give the total electron count as 2.1 and 3.4 respectively, where both the values are larger that the maximum possible value 2.0. The overall quantity which determines the DFT + U energy correction is the difference between the partial traces of **P** and $\mathbf{P}\cdot\mathbf{P}$ according to Eq. (3.22). From Table 3.1, it can be seen that for the $1s$ and $2p$ shells of H and N atoms in H_2 and NH_3, both the partial traces differ in various definitions of **P**. The discrepancies between various definitions of orbital occupation matrices are due to the contributions of the overlap matrix, hence it is easy to understand that for atoms, all the four definitions of **P** are equivalent.

The $4f$ orbitals of the lanthanide system GdF_3 have very short radial extensions, hence they are localized on the Gd atom. In this case, all the four definitions of **P** are equivalent, hence the partial traces computed using these matrices are identical. A systematic study of the performance of various definitions of **P** is beyond the scope of the present work. However some remarks about the natural occupation numbers given by various definitions of **P** can be made. The quality of the natural occupation numbers will certainly depend on the quality of the basis set employed. Hence if possible, one must employ basis sets that use contractions coefficients obtained from the

eigenvectors (atomic contractions) computed at the same level of theory. In the applications, if the absolute value of the DFT + U energy correction is not of important, but only relative energies are important, one can relax the strict criteria regarding the use of atomic contractions. In order to arrive at a global definition of natural atomic orbitals to use in the DFT + U methodology for a wide range of systems it is perhaps important to consider the ideas employed in related studies such as *natural orbital functional theory* [86] or other semi-empirical orbital occupation methods [87, 88].

Table 3.1: Comparison of the values of the traces that enter into the DFT + U energy correction expressions, Eq. (3.29) and Eq. (3.30) according to various definitions of orbital occupation matrices.

Molecule	Atomic shell s	$\mathbf{P}$	$\sum_\sigma \mathrm{Tr}(\mathbf{N}^\sigma)$	$\sum_\sigma \mathrm{Tr}(\mathbf{N}^\sigma \cdot \mathbf{N}^\sigma)$
H_2	H $1s$	$\mathbf{D}$	1.19	1.43
		$\frac{1}{2}(\mathbf{D}.\mathbf{S}+\mathbf{S}\cdot\mathbf{D})$	2.13	4.55
		$\mathbf{S}\cdot\mathbf{D}\cdot\mathbf{S}$	3.41	11.62
		$\mathbf{S}^{(1/2)}\cdot\mathbf{D}\cdot\mathbf{S}^{(1/2)}$	1.79	3.13
NH_3	N $2p$	$\mathbf{D}$	3.83	4.98
		$\frac{1}{2}(\mathbf{D}.\mathbf{S}+\mathbf{S}\cdot\mathbf{D})$	4.56	6.97
		$\mathbf{S}\cdot\mathbf{D}\cdot\mathbf{S}$	5.44	9.89
		$\mathbf{S}^{(1/2)}\cdot\mathbf{D}\cdot\mathbf{S}^{(1/2)}$	2.52	2.14
GdF_3	Gd $4f$	$\mathbf{D}$	7.08	6.99
		$\frac{1}{2}(\mathbf{D}.\mathbf{S}+\mathbf{S}\cdot\mathbf{D})$	7.11	6.97
		$\mathbf{S}\cdot\mathbf{D}\cdot\mathbf{S}$	7.16	6.99
		$\mathbf{S}^{(1/2)}\cdot\mathbf{D}\cdot\mathbf{S}^{(1/2)}$	7.08	6.89

[a] For H_2 and NH_3, non-relativistic spin-restricted calculations were performed and for GdF_3 relativistic (DKH) spin-unrestricted calculations were performed. For all the systems single point calculations were performed at the corresponding PBE equilibrium geometries.

3.2 DFT + U Hamiltonian Matrix and Analytic Gradients

In order to compute the DFT + U energy correction in a self-consistent way, the DFT + U potential has to be defined. The DFT + U potential enters in the form of a Hamiltonian correction matrix which is added to the Kohn–Sham Hamiltonian matrix which when diagonalized gives the Kohn–Sham eigenvalues. In order to provide DFT + U corrections to molecular geometries, the DFT + U gradient correction is needed. The DFT + U gradients can be numerically computed

through several single point calculations which however is prohibitively time consuming for larger systems. In order to perform efficient geometry optimizations analytic expressions for DFT + U gradient corrections are needed. The expressions for both DFT + U Hamiltonian matrix and DFT + U gradient corrections have been derived and implemented in PARAGAUSS. In the following a brief procedure to derive these expressions will be given in the form of set of mathematical rules followed by a list of these expressions that are specific for the DFT + U functional forms and the definition of the orbital occupation matrix.

It should be noted that for a single point energy evaluation, it sufficient to have only the DFT + U Hamiltonian correction matrix elements. In the present section, the expressions for the DFT + U potential correction matrix elements are presented along with the DFT + U gradient correction terms in order to exploit the similarities in their derivation and the common intermediate terms that enter into these expressions.

3.2.1 Some Useful Expressions

The derivation of DFT + U Hamiltonian and gradient corrections involve extensive usage of chain rules of partial differentiation. The derivation of these expressions are not presented in this work and only the final expressions are listed. In the derivation of these expressions, the following rules were systematically used while differentiating a summation or to simplify an expression. These rules are only presented here in order to aid a future worker who might encounter similar derivations.

Rule 1 The partial derivative of the element of a matrix $\mathbf{X}$ with respect to another element of the same matrix is given by

$$\frac{\partial X_{i,j}}{\partial X_{k,l}} = \delta_{i,k}\delta_{j,l}. \tag{3.37}$$

The above equation is often encountered in the following form when dealing with a spin-specific orbital occupation matrix $\mathbf{P}^{\sigma}$

$$\frac{\partial P^{\sigma}_{\mu,\nu}}{\partial P^{\sigma'}_{\mu',\nu'}} = \delta_{\sigma,\sigma'}\delta_{\mu,\mu'}\delta_{\nu,\nu'}, \tag{3.38}$$

where δ_{ij} is the Kronecker delta function.

Rule 2 An expression involving a summation with several dummy indices can be simplified as follows.

$$\sum_{\sigma}\sum_{\mu}\sum_{\nu} P^{\sigma}_{\mu,\nu}\delta_{\sigma,\sigma'}\delta_{\mu,\mu'}\delta_{\nu,\nu'} = \sum_{\mu}\sum_{\nu} P^{\sigma'}_{\mu,\nu}\delta_{\mu,\mu'}\delta_{\nu,\nu'} = \sum_{\nu} P^{\sigma'}_{\mu',\nu}\delta_{\nu,\nu'} = P^{\sigma'}_{\mu',\nu'}. \tag{3.39}$$

Rule 3 The product of two Kronecker delta functions that share a common index can be simplified as

$$\delta_{\mu,\mu'}\delta_{\mu,\nu'} = \delta_{\mu',\nu'}. \tag{3.40}$$

3.2.2 DFT + U Hamiltonian Correction Matrix

The DFT + U Hamiltonian matrix is a sum of the KS Hamiltonian matrix and the DFT + U correction matrix. The general spin-specific form of the DFT + U Hamiltonian is given by

$$\mathbf{h}^{\sigma,\mathrm{DFT+U}} = \mathbf{h}^{\sigma,\mathrm{DFT}} + \mathbf{h}^{\sigma,\mathrm{U}}, \tag{3.41}$$

where $\sigma, \mathbf{h}^{\mathrm{DFT}}$ is the spin-specific KS Hamiltonian matrix and $\mathbf{h}^{\sigma,\mathrm{U}}$ is the spin-specific DFT + U Hamiltonian correction matrix. The general expression for the matrix elements of $\mathbf{h}^{\mathrm{U}}$ is the variational derivative of the energy term with respect to the corresponding matrix elements of the density matrix:

$$h^{\sigma,\mathrm{U}}_{\mu,\nu} = \frac{dE^{\mathrm{U}}}{dD^{\sigma}_{\mu,\nu}}, \tag{3.42}$$

which is evaluated using the chain rule for partial differentiation as

$$h^{\sigma,\mathrm{U}}_{\mu,\nu} = \sum_{\sigma'}\sum_{\mu'}\sum_{\nu'} \frac{\partial E^{\mathrm{U}}}{\partial P^{\sigma'}_{\mu',\nu'}} \frac{\partial P^{\sigma'}_{\mu',\nu'}}{\partial D^{\sigma}_{\mu,\nu}}. \tag{3.43}$$

In the above equation, the energy functional dependent term which is the first factor inside the summation on the r.h.s. can be computed using the rules Eqs. (3.38–3.40) as

$$v^{\sigma'}_{\mu',\nu'} = \frac{\partial E^{\mathrm{U}}}{\partial P^{\sigma'}_{\mu',\nu'}} = -U_{\mathrm{eff}}\left[P^{\sigma'}_{\nu',\mu'} - \frac{1}{2}\delta_{\mu',\nu'}\right]. \tag{3.44}$$

The above expression is the formal definition of the *symmetric matrix* $\mathbf{v}^{\sigma}$ which is used as an intermediate matrix both in the derivation and in the implementation of various expressions. The size of the matrix $\mathbf{v}^{\sigma}$ is the same as the Hamiltonian matrix. In the present implementation, $\mathbf{v}^{\sigma}$ is constructed from the much smaller matrix $\mathbf{u}^{\sigma}$ that corresponds to the shell index $[U,L,C]$ which is defined as

$$u^{\sigma}_{\mu,\nu} = \frac{\partial E^{\mathrm{U}}}{\partial N^{\sigma}_{\mu,\nu}}. \tag{3.45}$$

The procedure to construct $\mathbf{v}^{\sigma}$ from $\mathbf{u}^{\sigma}$ is the reverse of the procedure which is used to extract $\mathbf{N}^{\sigma}$ from $\mathbf{P}^{\sigma}$ which can be briefly mentioned as adding the elements of $\mathbf{u}^{\sigma}$ at the appropriate places of an empty matrix $\mathbf{v}^{\sigma}$.

In Eq. (3.43), the orbital occupation matrix dependent term, which is the second factor inside the summation on the r.h.s. of Eq. (3.43) is dependent on the definition of the orbital occupation

matrix. For the various definitions of orbital occupation matrix, this term is given as

$$\frac{\partial P^{\sigma'}_{\mu',\nu'}}{\partial D^{\sigma}_{\mu,\nu}} = \delta_{\sigma,\sigma'}\delta_{\mu,\mu'}\delta_{\nu,\nu'} \quad \text{where} \quad \mathbf{P}^{\sigma} = \mathbf{D}^{\sigma}, \tag{3.46}$$

$$\frac{\partial P^{\sigma'}_{\mu',\nu'}}{\partial D^{\sigma}_{\mu,\nu}} = \frac{1}{2}\left[\delta_{\sigma,\sigma'}\delta_{\mu,\mu'}S_{\nu,\nu'} + S_{\mu',\mu}\delta_{\sigma,\sigma'}\delta_{\nu,\nu'}\right] \quad \text{where} \quad \mathbf{P}^{\sigma} = \frac{1}{2}\left[\mathbf{D}^{\sigma}\cdot\mathbf{S} + \mathbf{S}\cdot\mathbf{D}^{\sigma}\right] \tag{3.47}$$

and

$$\frac{\partial P^{\sigma'}_{\mu',\nu'}}{\partial D^{\sigma}_{\mu,\nu}} = T_{\mu',\mu}\delta_{\sigma,\sigma'}T_{\nu,\nu'} \quad \text{where} \quad \mathbf{P}^{\sigma} = \mathbf{T}\cdot\mathbf{D}^{\sigma}\cdot\mathbf{T} \quad \text{where} \quad \mathbf{T} = \mathbf{S} \text{ or } \mathbf{S}^{(1/2)}. \tag{3.48}$$

Using Eqs. (3.44 – 3.48) in Eq. (3.43), expression for the DFT + U Hamiltonian correction matrix $\mathbf{h}^{\sigma,\mathrm{U}}$ for the various definitions of orbital occupation matrix can be given as follows

$$\mathbf{h}^{\sigma,\mathrm{U}} = \mathbf{v}^{\sigma} \quad \text{for} \quad \mathbf{P}^{\sigma} = \mathbf{D}^{\sigma}, \tag{3.49}$$

$$\mathbf{h}^{\sigma,\mathrm{U}} = \frac{1}{2}\left[\mathbf{v}^{\sigma}\cdot\mathbf{S} + \mathbf{S}\cdot\mathbf{v}^{\sigma}\right] \quad \text{for} \quad \mathbf{P}^{\sigma} = \frac{1}{2}\left[\mathbf{D}^{\sigma}\cdot\mathbf{S} + \mathbf{S}\cdot\mathbf{D}^{\sigma}\right] \tag{3.50}$$

and

$$\mathbf{h}^{\sigma,\mathrm{U}} = \mathbf{T}\cdot\mathbf{v}^{\sigma}\cdot\mathbf{T} \quad \text{for} \quad \mathbf{P}^{\sigma} = \mathbf{T}\cdot\mathbf{D}^{\sigma}\cdot\mathbf{T} \quad \text{where} \quad \mathbf{T} = \mathbf{S} \text{ or } \mathbf{S}^{(1/2)}. \tag{3.51}$$

3.2.3 DFT + U Analytic Gradients

The DFT + U gradient due to the displacement of the nuclear coordinate q_i is given as the sum of contributions due to the DFT gradient and a gradient correction term:

$$\frac{dE^{\mathrm{DFT+U}}}{dq_i} = \frac{dE^{\mathrm{DFT}}}{dq_i} + \frac{dE^{\mathrm{U}}}{dq_i}. \tag{3.52}$$

The DFT + U gradient correction term is evaluated using the chain rule for partial differentiation as

$$\frac{dE^{\mathrm{U}}}{dq_i} = \sum_{\sigma}\sum_{\mu}\sum_{\nu}\frac{\partial E^{\mathrm{U}}}{\partial P^{\sigma}_{\mu\nu}}\frac{\partial P^{\sigma}_{\mu\nu}}{\partial q_i}. \tag{3.53}$$

The first factor on the r.h.s. of the above equation can be identified as the element of the matrix $\mathbf{v}^{\sigma}$ which is a symmetric matrix, Eq. (3.44). Thus Eq. (3.53) can be written as

$$\frac{dE^{\mathrm{U}}}{dq_i} = \sum_{\sigma}\sum_{\mu}\sum_{\nu}v^{\sigma}_{\mu\nu}\frac{\partial P^{\sigma}_{\mu\nu}}{\partial q_i} = \sum_{\sigma}\sum_{\mu}\sum_{\nu}v^{\sigma}_{\nu\mu}\frac{\partial P^{\sigma}_{\mu\nu}}{\partial q_i} = \sum_{\sigma}\mathrm{Tr}\left[\mathbf{v}^{\sigma}\cdot\frac{\partial \mathbf{P}^{\sigma}}{\partial q_i}\right]. \tag{3.54}$$

For all definitions of $\mathbf{P}^{\sigma}$, the total gradient according to Eq. (3.54), is given as the sum of two gradient terms, due to the Hellmann–Feynman force and Pulay force [55, 89].

$$\frac{dE^{\mathrm{U}}}{dq_i} = \left[\frac{dE^{\mathrm{U}}}{dq_i}\right]_{HF} + \left[\frac{dE^{\mathrm{U}}}{dq_i}\right]_{Pulay} \tag{3.55}$$

The gradient term due to the Pulay force arises from the change in the density matrix $\mathbf{D}^\sigma$ due to the displacement of the nuclear coordinates q_i. This term is common for all the definitions of $\mathbf{P}^\sigma$ and can be derived as

$$\left[\frac{dE^{\mathrm{U}}}{dq_i}\right]_{Pulay} = \sum_\sigma \mathrm{Tr}\left[\mathbf{h}^{\sigma,\mathrm{U}} \cdot \frac{\partial \mathbf{D}^\sigma}{\partial q_i}\right]. \tag{3.56}$$

It should be noted that the above expression need not be coded separately. When the DFT + U Hamiltonian correction matrix is added to the DFT Hamiltonian matrix, this term will be computed along with the similar contribution due to the DFT Hamiltonian matrix [89].

The gradient term due to Hellmann-Feynman force arises due to the dependency of the overlap matrix $\mathbf{S}$ on the nuclear coordinates q_i. For the onsite occupation matrix $\mathbf{P}^\sigma = \mathbf{D}^\sigma$ where there is no overlap dependence, the Hellmann-Feynman force vanishes hence the corresponding term is zero. For the Mulliken population matrix and for the full-occupation matrix, the gradient correction term due to the Hellman-Feynman force can be derived as

$$\left[\frac{dE^{\mathrm{U}}}{dq_i}\right]_{HF} = \mathrm{Tr}\left[\frac{d\mathbf{S}}{dq_i} \cdot \mathbf{A}\right] \tag{3.57}$$

where the intermediate matrix $\mathbf{A}$ which is dependent on the definition of $\mathbf{P}^\sigma$ is given as

$$\mathbf{A} = \frac{1}{2}\sum_\sigma [(\mathbf{D}^\sigma \cdot \mathbf{v}^\sigma + \mathbf{v}^\sigma \cdot \mathbf{D}^\sigma)] \quad \text{for} \quad \mathbf{P}^\sigma = \frac{1}{2}[\mathbf{D}^\sigma \cdot \mathbf{S} + \mathbf{S} \cdot \mathbf{D}^\sigma] \tag{3.58}$$

and

$$\mathbf{A} = \sum_\sigma [(\mathbf{D}^\sigma \cdot \mathbf{S} \cdot \mathbf{v}^\sigma + \mathbf{v}^\sigma \cdot \mathbf{S} \cdot \mathbf{D}^\sigma)] \quad \text{for} \quad \mathbf{P}^\sigma = \mathbf{S} \cdot \mathbf{D}^\sigma \cdot \mathbf{S}. \tag{3.59}$$

In the present implementation, analytic DFT + U gradient corrections are not available when the orbital occupation matrix is defined as the Löwdin population matrix. In this case, the difficulty in arriving at an expression for DFT + U gradient correction is due to a term which involves derivative of the square root of the overlap matrix with respect to the nuclear coordinates. It is perhaps possible to derive this term by following the technique given by Nasluzov and Rösch in the context of relativistic analytic gradients [90–92].

3.3 Implementation

In the implementation of the DFT + U methodology in PARAGAUSS the main quantities involved are orbital occupation matrices according to Eqs. (3.33–3.36), the DFT + U energy correction terms according to Eqs. (3.29,3.30), DFT + U Hamiltonian correction matrices according to Eq. (3.49–3.51) and analytic gradient corrections according to Eq. (3.58, 3.59). These quantities were implemented n almost the same way as they are defined in the previous section in a separate module `dft_plus_u_module` within the main program.

3.3.1 Intermediate Procedures

Essential for the implementation of the main quantities are two routines namely `get_block` and `add_block`. The routine `get_block` is needed in order to extract a sub-matrix that corresponds to the specified shell s i.e.$[U,L,C]$ from a full matrix and `add_block` is needed to perform the reverse task i.e., to add the elements of a submatrix to a full matrix at the appropriate indices that corresponds to the shell $[U,L,C]$. These two routines are used to extract $\mathbf{N}^\sigma$ from $\mathbf{P}^\sigma$ and to add $\mathbf{u}^\sigma$ to the empty matrix $\mathbf{v}^\sigma$ respectively.

Extracting the submatrix $\mathbf{N}^\sigma$ from $\mathbf{P}^\sigma$ is performed in the `dft_plus_u_module` by calling the subroutine `get_block`.

$$\mathbf{N}^\sigma \Leftarrow \texttt{get\_block}(\mathbf{P}^\sigma, s) \tag{3.60}$$

In PARAGAUSS, basis functions are ordered by four nested indices U (unique atom index), L (angular momentum), C (contraction number), N (independent functions). The size of the sub-matrix is $N_{eq}\,(2L+1)$ where N_{eq} is the number of atoms belonging to a unique type U. With in the given point group symmetry, the matrix $\mathbf{N}^\sigma$ will have off-diagonal elements only if the number of independent functions for the given shell $[U,L,C]$ is greater than 1 in any of the irreducible representations. Figure 3.1 shows the indexing of orbital basis functions for the example case H_2O.

The pseudo code to extract the sub-matrix $\mathbf{N}^\sigma$ for an arbitrary shell index $[U,L,C]$ from the full matrix $\mathbf{P}^\sigma$ is given in Figure 3.2. Adding the submatrix $\mathbf{u}^\sigma$ to an empty matrix $\mathbf{v}^\sigma$ at the indices corresponding to $s = [U,L,C]$ is performed in the `dft_plus_u_module` of PARAGAUSS by calling the subroutine `add_block`.

$$\mathbf{u}^\sigma \Rightarrow \texttt{add\_block}(\mathbf{v}^\sigma, s) \tag{3.61}$$

The general looping structure of the procedure `add_block` is same as that of `get_block`.

3.3.2 Parallelization of Gradient Computation

The main data involved in the evaluation of DFT + U analytic gradient corrections is the derivative of the overlap matrix with respect to the nuclear coordinates. The computation of the trace according to Eq. (3.57) is handled by the subroutine `dftpu_grad` with in the `dft_plus_u_module`. The structure of the subroutine `dftpu_grad` and the other procedures called with in this subroutine is based on the scheme of integral storage in PARAGAUSS which is employed especially during gradient computations [93]. The two-center integrals are grouped in packages that are individually described by the quadruples (U_1, L_1, U_2, L_2). DFT gradients are computed in batches of contributions that correspond to these quadruples (U_1, L_1, U_2, L_2). Thus these quadruples

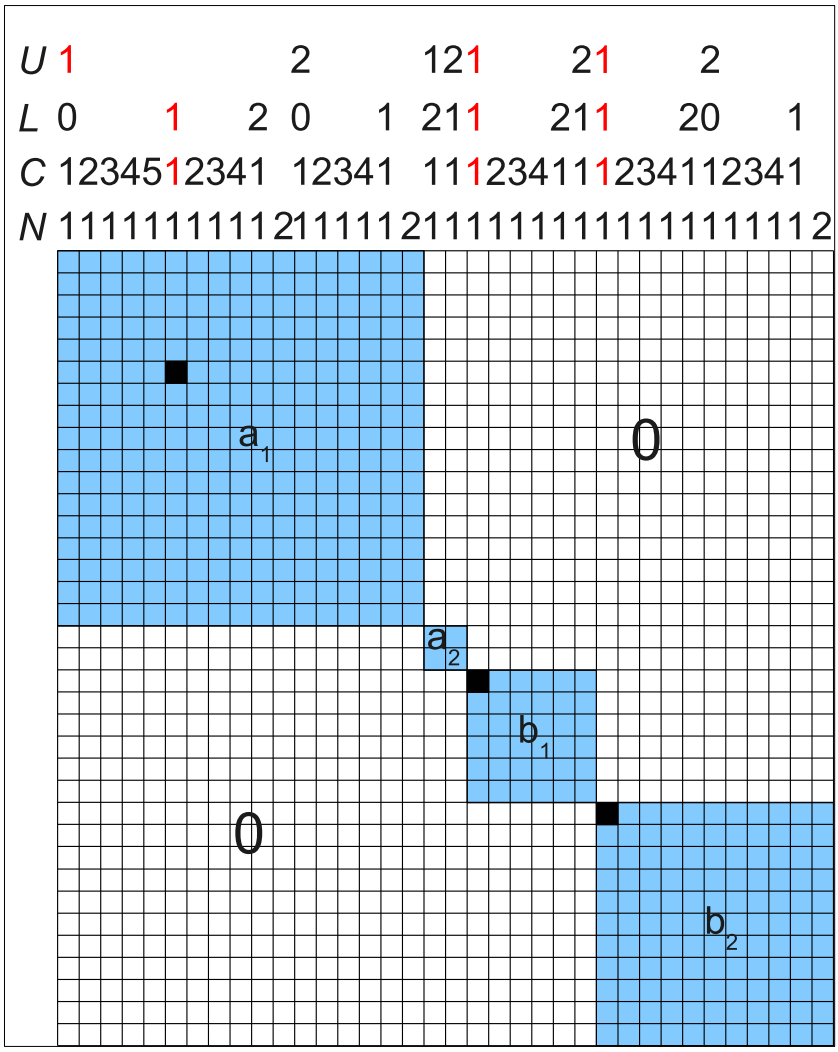

Figure 3.1: Orbital occupation matrix **P** for H_2O in C_{2v} point group symmetry. The non-zero elements of **P** are along the diagonal blocks (blue) in the order of a_1, a_2, b_1 and b_2 irreducible representations. The dark squares along the diagonal correspond to the diagonal elements of the sub-matrix **N** corresponding to the $2p$ shell of O atom, (U = 1, L = 1, C = 1, in red). Here the number of independent functions (N) is not greater than 1 for any of the irreducible representations, hence **N** is a diagonal matrix. The basis sets used are O: $(14s, 9p, 4d) \rightarrow [5s, 4p, 3d]$, H: $(8s, 4p, 3d) \rightarrow [4s, 3p, 2d]$.

```
N_cont = get_N_cont(U,L)      ! Get the no. of contractions
k = 0
do irr = 1, N_irr
  N_ind = get_N_ind(U,irr,L)  ! Get the no. of independent fns
  N_par = get_N_par(U,irr,L)  ! Get the no. of partners
  off   = get_off(U,irr,L)    ! Get offset of (U,irr,L) in the full matrix
  do i = 1, N_ind
    do j = 1, N_ind
      ii = off + N_cont * (i - 1) + C
      jj = off + N_cont * (j - 1) + C
      do s = 1, N_spin
        N(k+i, k+j, s) = P(irr)%m(ii,jj,s)/N_par
      enddo
    enddo
    k = k + N_ind
  enddo
enddo
```

Figure 3.2: Pseudo code for get_block

are passed to the subroutine `dftpu_grad` one set at a time along with the two-center integrals `symadapt_int_2cob_ol_grad` that correspond to the gradient of overlap matrix elements. For a given set of (U_1, L_1, U_2, L_2), relevant elements of `symadapt_int_2cob_ol_grad` are used along with the corresponding elements of the matrix **A**, Eq. (3.58, 3.59) to compute a subtrace that contributes to the total trace given in Eq. (3.57). In the following, this procedure is briefly described.

The data `symadapt_int_2cob_ol_grad` is a pointer with the full shape

```
symadapt_int_2cob_ol_grad(1:N_gradients, 1:N_irr)%int(:,:,:,:)
```

which has one 4-D array per irreducible representation, per gradient and matrix **A** which is also a pointer has the full shape

```
A(1:N_irr)%m(:,:)
```

which is block diagonalized similar to **P** in Figure 3.1 and has one square matrix (2-D array) per irreducible representation. The procedure to compute the subtrace for a given set of quadruple indices (U_1, L_1, U_2, L_2) is given by the pseudo code in Figure 3.3.

All the intermediate data that are needed for the computation of DFT + U analytic gradient corrections are allocated at beginning of the process and deallocated at the end of the process by the main or the *master* processor. Among the two data needed for the DFT + U gradient evaluation, distribution of blocks of `symadapt_int_2cob_ol_grad` to various processors is done outside

```
subtrace = 0
do grad = 1, N_gradients
  do irr = 1, N_irr
    times = 1 if diagonal quadruple (U1, L1, U1, L1)
          = 2 if off-diagonal quadruple (U1, L1, U2, L2)
    N_par = No. of partners of irr     % degeneracy index
    N_C1   = size(symadapt_int_2cob_ol_grad(grad,irr)%int, 1)
    N_C2   = size(symadapt_int_2cob_ol_grad(grad,irr)%int, 2)
    N_ind1 = size(symadapt_int_2cob_ol_grad(grad,irr)%int, 3)
    N_ind2 = size(symadapt_int_2cob_ol_grad(grad,irr)%int, 4)
    L_bound_1 = fn_of(irr, L1, U1)
    U_bound_1 = fn_of(L_bound_1, N_C2, N_ind2)
    L_bound_2 = fn_of(irr, L, U2)
    U_bound_2 = fn_of(L_bound_2, N_C1, N_ind1)
    submat_A  = A(irr)%m(L_bound_1:U_bound_1, L_bound_2:U_bound_2)
    subsubtrace = fn_of(submat_A,symadapt_int_2cob_ol_grad(grad,irr)%int)
    subtrace = subtrace + subsubtrace * times * N_par
  enddo
enddo
```

Figure 3.3: Pseudo code for compute subtrace for gradients

the `dft_plus_u_module`. Within the `dft_plus_u_module`, different blocks of **A** that correspond to various irreducible representations are distributed to various processors by the master processor.

3.4 FLL-DFT + U corrections

In the present work, all the applications have been performed using the FLL-DFT + U correction method. The FLL-DFT + U energy correction term and the potential or Hamiltonian correction matrix elements are formally written in the rotationally invariant form involving traces of **N** or **P** matrices. However during the analysis of results it has been found easier to work with the functional form in the natural orbital representation. In the natural orbital representation, the spin-specific FLL-DFT + U energy correction for a single orbital can be given as

$$E^U = \frac{1}{2} U_{\text{eff}}\, n_i^\sigma \,(1 - n_i^\sigma) \tag{3.62}$$

which provides a positive energy correction when n_i^σ is fractional and no corrections when $n_i^\sigma = 0$ or 1. Individual contributions due to all the natural orbitals of a given shell s then provides the total FLL-DFT + U energy correction. The nature of FLL-DFT + U correction in the total energy is shown in Figure 3.4 for the example system C atom.

The FLL-DFT + U potential correction is given by

$$v_i^{\sigma,U} = U_{\text{eff}} \left(\frac{1}{2} - n_i^{\sigma} \right). \tag{3.63}$$

According to the above equation, for a spin-specific natural orbital with occupation number n_i^{σ}, the FLL-DFT + U potential provides appropriate correction to the corresponding orbital energy ε_i^{σ}. Thus if the occupation number n_i^{σ} equals 1 (occupied natural orbital), the potential correction shifts down the corresponding orbital energy by $-U_{\text{eff}}/2$ and if the natural orbital is empty, the potential correction shifts up the corresponding orbital energy by $U_{\text{eff}}/2$. The nature of FLL-DFT + U correction in the orbital energy shown in Figure 3.5 for the example system C atom.

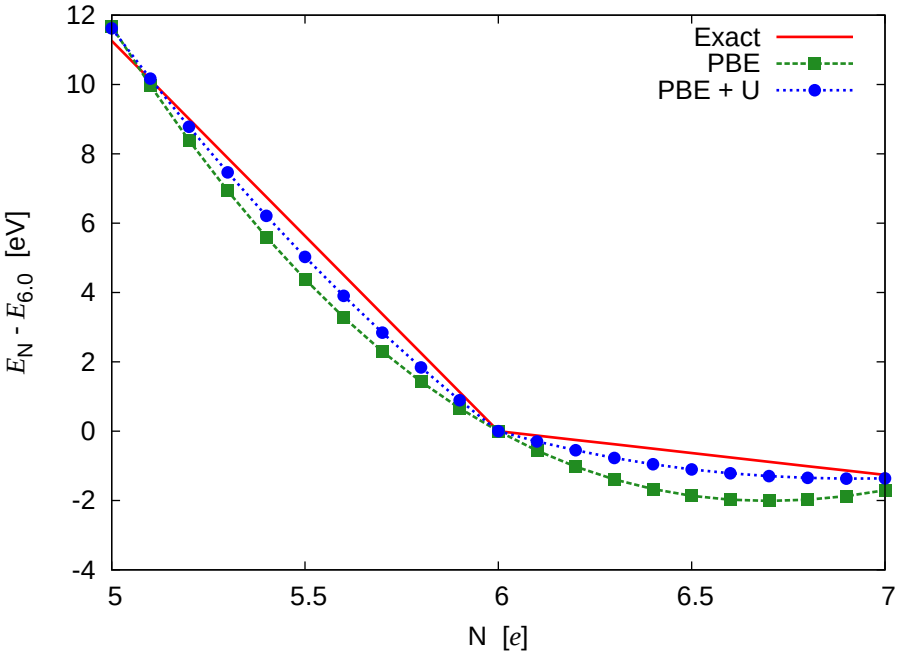

Figure 3.4: FLL-DFT + U energy correction for C atom: The relative energy $E_N - E_{6.0}$ (in eV) is plotted a function of total number of electrons N in the range $5 \leq N \leq 7$. The exact line is obtained by interpolating between the ionization potential of C atom (11.26 eV) and negative of the electron affinity of C atom (-1.26 eV). DFT calculations were performed at the PBE-GGA level. In the PBE + U calculation, an arbitrary value of $U_{\text{eff}} = 5$ eV was used for the $2p$ shell of C atom.

Orbital occupation dependent energy functionals such as the FLL-DFT + U term Eq. 3.62 which involve a penalty functional often perform differently when various symmetry restrictions are employed.

This is illustrated in Figure 3.6 for the FLL-DFT + U energy correction for C atom with I_h (spherically symmetric) C_1 (no symmetry) point group symmetry restrictions. The spherically

symmetric situation is described in the DFT + U literature as an around mean field (AMF) approximation [79, 94] where the total number of electrons of a shell s is distributed to all the orbitals of the shell by spherically averaging i.e. $n_i = N/(2L+1)$. As shown in Figure 3.6, for a simple case of C atom with 1, the energy correction is 0 when electron is located on a single orbital (FLL) and when the single electron is distributed spherically i.e. 1/3 e per $2p$ orbital (AMF), the energy correction is positive. An exception to this situation is a completely filled system (or empty system), where both FLL and AMF limits are equivalent, hence FLL-DFT + U correction will be the same. It is also the case for arbitrary symmetry restrictions when the degenerate orbitals are either completely filled or empty. When spherical symmetry restrictions are employed, the orbital-specific FLL-DFT + U penalty functional according to Eq. (3.62) becomes a shell-specific penalty functional which provides no contribution when the shell population is 0 or N and provides a positive correction when the shell population is between 0 and N.

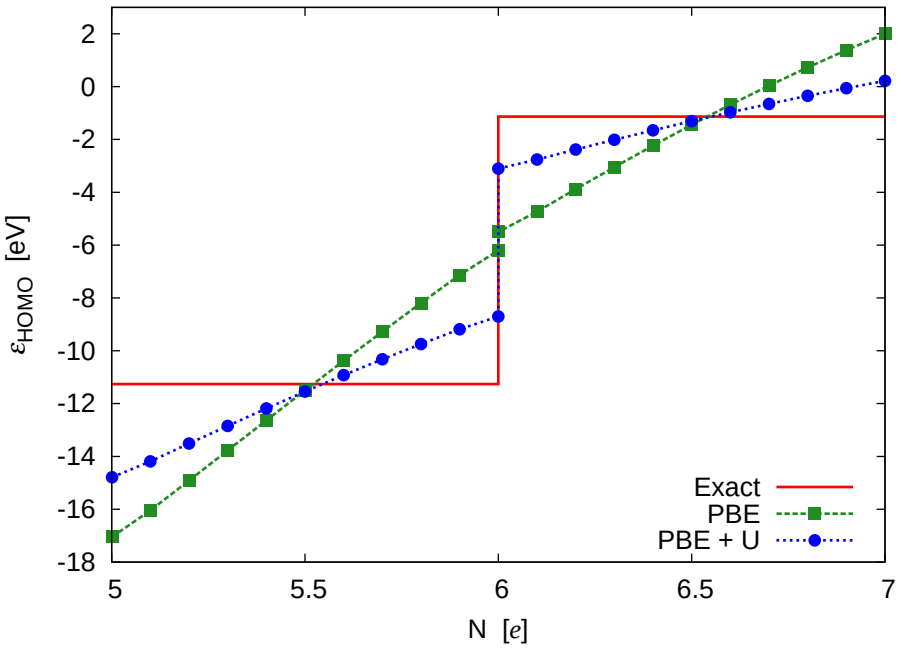

Figure 3.5: FLL-DFT + U correction for ε_{HOMO} of C atom: ε_{HOMO} (in eV) is plotted a function of total number of electrons N in the range $5 \leq N \leq 7$. The exact line is obtained by interpolating between the negative of ionization potential of C atom (-11.26 eV) and negative of the electron affinity of C atom (-1.26 eV). DFT calculations were performed at the PBE-GGA level. In the PBE + U calculation, an arbitrary value of $U_{\text{eff}} = 5$ eV was used for the $2p$ shell of C atom.

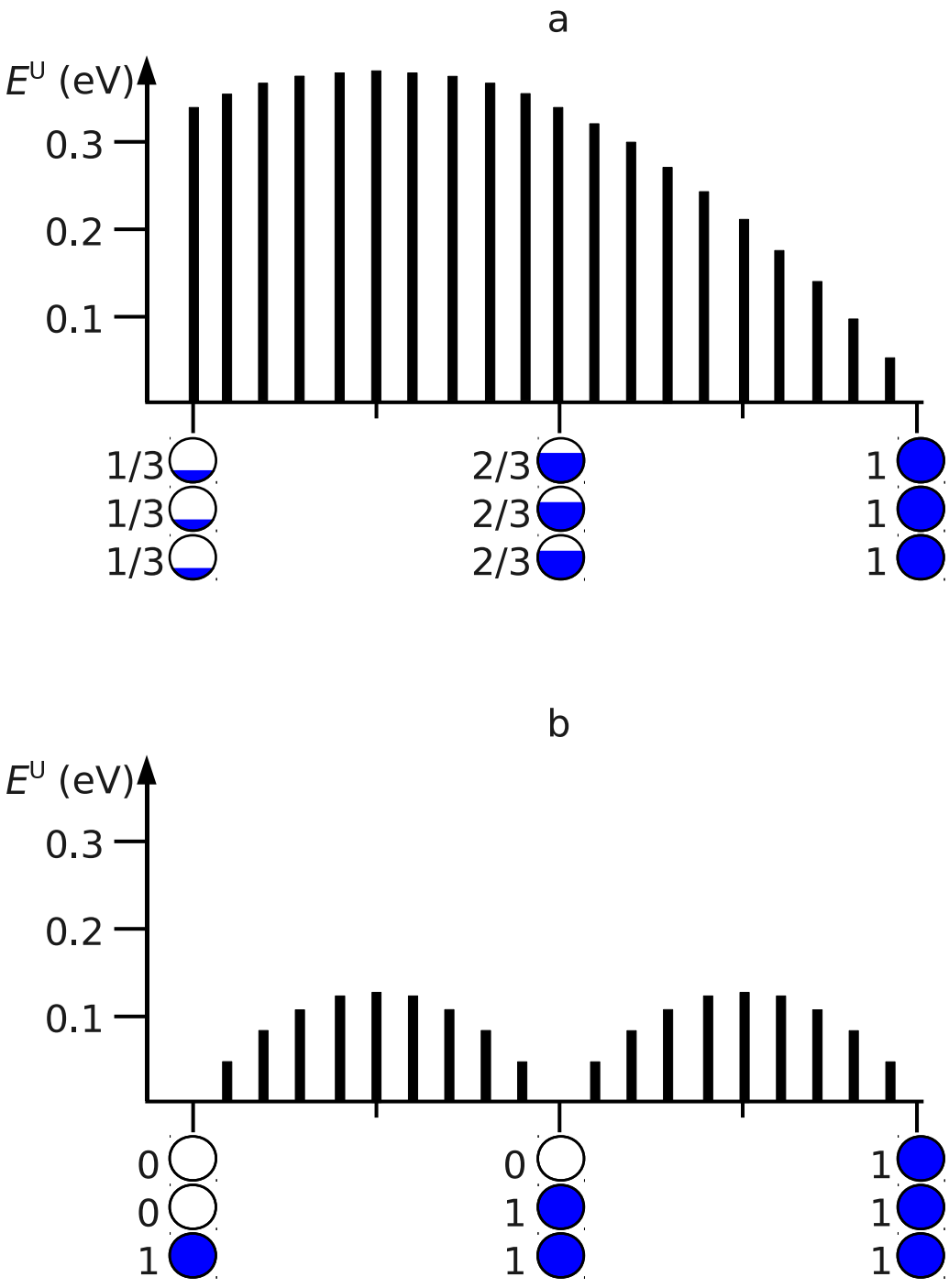

Figure 3.6: FLL-DFT + U energy correction for C atom in a. I_h, b. C_1 point group symmetry restrictions. In the PBE + U calculation, an arbitrary value of $U_{\text{eff}} = 1$ eV was used for the $2p$ shell of C atom.

Chapter 4

Computational Details

the Computational details of all the applications performed in the present thesis are presented in this chapter. In section 4.1, computational details regarding the choice of DFT methods, basis sets, etc., are summarized. Section 4.2, exclusively deals with the estimation of the effective onsite-Coulomb parameter used in the DFT + U calculations.

4.1 Method

All the calculations were performed at the scalar relativistic level using the all-electron Douglas-Kroll-Hess (AE-DKH) approximation [24] in the linear combination of Gaussian-type orbitals fitting-functions density functional (LCGTO-FF-DF) method [103] as implemented in the parallel code PARAGAUSS [21, 22]. Spin-orbit effects were not included in any of the calculations. Both LDA and GGA exchange correlation functionals were employed. For the lanthanide systems, PBE-GGA [46] XC functional was employed for the lanthanide trihalide systems LnF_3 (Ln = La, Ce, Gd, Lu) and for the ceria nano-particles VWN-LDA [40] XC functional was employed. For the uranyl dication molecule all the calculations were performed using the PBE-GGA XC functional. DFT + U calculations were performed using the FLL-DFT + U scheme with the full occupation matrix $\mathbf{P} = \mathbf{S} \cdot \mathbf{D} \cdot \mathbf{S}$.

Table 4.1 presents the details of the orbital basis sets, polarization functions used in all the calculations. In Table 4.1, only the size of the basis sets and polarization functions are given. The exponents and the contraction coefficients of the basis sets with their references are presented separately in Appendix I. The auxiliary basis sets used in the LCGTO-FF-DF method to evaluate the Hartree part of the electron-electron interaction was derived from the orbital basis set in a standard fashion [103].

Numerical grids were used to numerically integrate the XC contributions to the one-electron

Table 4.1: Basis sets and polarization functions employed in the calculations. N_Bas: the contraction scheme of the atomic orbital basis sets, and N_Pol: number of polarization functions.

System	Atom	N_Bas	N_Pol
LnF_3	La	$(24s,21p,15d,5f) \rightarrow [9s,8p,6d,4f]$	$(5p,5d,5f)$
	Ce	$(25s,22p,15d,11f) \rightarrow [9s,8p,6d,4f]$	$(5p,5d,5f)$
	Gd	$(25s,22p,15d,11f) \rightarrow [9s,8p,6d,4f]$	$(5p,5d,5f)$
	Lu	$(25s,22p,15d,11f) \rightarrow [9s,8p,6d,4f]$	$(5p,5d,5f)$
	F	$(14s,9p,4d,3f) \rightarrow [5s,4p,3d,2f]$	$(5p,5d)$
Ceria	Ce	$(25s,22p,15d,11f) \rightarrow [9s,8p,6d,4f]$	$(5p,5d,5f)$
	O	$(9s,5p,1d) \rightarrow [5s,4p,1d]$	$(5p,5d)$
UO_2^{2+}	U	$(24s,19p,16d,11f) \rightarrow [10s,7p,7d,4f]$	$(5p,5d,5f)$
	O	$(9s,5p,1d) \rightarrow [5s,4p,1d]$	$(5p,5d)$
$[UO_2(H_2O)_5]^{2+}$	U	$(24s,19p,16d,11f) \rightarrow [10s,7p,7d,4f]$	$(5p,5d,5f)$
	O	$(9s,5p,1d) \rightarrow [5s,4p,1d]$	$(5p,5d)$
	H	$(6s,1p) \rightarrow [4s,1p]$	$(5p,5d)$
UO_2OH^+	U	$(24s,19p,16d,11f) \rightarrow [10s,7p,7d,4f]$	$(5p,5d,5f)$
	O	$(9s,5p,1d) \rightarrow [5s,4p,1d]$	$(5p,5d)$
	H	$(6s,1p) \rightarrow [4s,1p]$	$(5p,5d)$

potential and the total energy. For the clusters of ceria, the grid settings used is locally accurate up to angular momentum L = 17 and contained 135 and 48 radial shells for Ce and O atoms respectively. For all other systems *fine* grids were employed which are locally accurate up to angular momentum L = 29. The number of radial shells in the chosen grids are 197, 189, 185, 180, 180, 68, 58, and 61 for La, Ce, Gd, Lu, U, O, F and H atoms, respectively. The details of symmetry constraints, geometry constraints employed in the calculations are given along with the discussions of the results. Similarly details of geometry optimization, frequency calculations are discussed along with results.

4.2 Effective Onsite-Coulomb Parameter

In the DFT + U calculations, the effective onsite-Coulomb parameter, U_{eff} was used as an empirical parameter chosen by fitting the DFT + U results of some observable target quantity. It is often the case that an approximate value or a narrow range of values seems to be U_{eff} in the DFT + U applications. The empirically fitted U_{eff} provides theoretical justification for the DFT + U cor-

Table 4.2: Estimation of U_{eff} to fit the 1s orbital energy, ε_{1s} of H atom in PBE approximation to the negative of experimental IP (-13.60 eV) by fitting a straight line.

U_{eff}	ε_{1s}
0.00	-7.58
2.00	-8.52
4.00	-9.47
6.00	-10.43
8.00	-11.39
10.00	-12.35
12.00	-13.32
14.00	-14.30
12.56 (optimum)	-13.60

rections. However, in the present work all the calculations were performed both for an optimum empirical value of U_{eff} and for a range of U_{eff} values. For all the systems, experimental ionization potential (IP) of the system was used as the target quantity. Vertical IP calculated as the difference of two total energies (ΔSCF approach) or the energy of the relevant orbital are fitted against the target quantity in choosing the approximately optimum value for U_{eff}.

The straightforward procedure to empirically fit a set of data is to compute data for a wide range of U_{eff} values and fit them with a straight line to get the optimal value of U_{eff} at which the observed value is reproduced. In Table 4.2, the results of this procedure is described for the example case H atom where the property of interest is the energy of the 1s orbital and the target quantity is the experimental IP of H atom. However, if the nature of the DFT + U correction is qualitatively known, an iterative method can be employed which leads to better insight and converges to an optimal U_{eff} value in a few steps. The FLL-DFT + U potential correction term shifts the energy of an occupied orbital by -U_{eff}/2 and an unoccupied orbital by +U_{eff}/2. Thus an optimum value of U_{eff} in which the orbital energy reproduces the experimental IP can be approximated in successive iterations as

$$U_{\text{eff}}^{k+1} = U_{\text{eff}}^{k} + 2\left(\text{IP} + \varepsilon_{1s}^{k}\right). \tag{4.1}$$

Table 4.3 presents the result of an iterative estimation of U_{eff} to to fit the energy of the 1s orbital of H atom to the experimental IP.

The $4f$ orbitals of lanthanide systems are highly localized. For the Ln $4f$ levels optimal U_{eff} values for the corresponding (Ln III) ions were obtained by fitting the $4f$ orbital energies ε_{4f} to the experimental IP [104]. In LnF_3 molecules, the actual oxidation state of the Ln ions need not necessarily be III. Hence, optimal U_{eff} values suitable for the $4f$ levels in the LnF_3

Table 4.3: Estimation of U_{eff} to fit the 1*s* orbital energy, ε_{1s} of H atom in PBE approximation to the negative of experimental IP (-13.60 eV) by the iterative method.

k	U^k_{eff}	ε^k_{1s}	IP+ε^k_{1s}
1	0.00	-7.58	6.02
2	12.04	-13.34	0.25
3	12.55	-13.59	0.01
4	12.56	-13.60	0.00

molecules were obtained by fitting the weighted center of the density of the $4f$-like states of these systems to the experimental IPs from photo-electron spectroscopy of these systems [105]. Table 4.4 presents the atomic and molecular U_{eff} values for these systems, where for the Lu $4f$ shell where the atom like localization is high in the LuF_3 molecule, the molecular U_{eff} value of 18.78 eV is very close to the atomic/ionic U_{eff} value 17.55 eV. As a compromise between these two, a U_{eff} value of 18.0 eV was used in the application of the DFT + U methodology for LuF_3. The U_{eff} values of ions were used only in exploratory calculations.

Table 4.4: Estimate of U_{eff} for the $4f$ shell of Ln (Ce, Gd, Lu) in LnF_3. Atomic U_{eff} values were obtained by fitting ε_{4f} of the Ln III ions to experimental IPs. Molecular U_{eff} values were obtained by fitting the weighted center of the density of states (DOS) of the $4f$ levels in LnF_3 molecules to the experimental IP from photo-electron spectroscopy. These values were estimated from AE-DKH-PBE+U calculations. All values are in eV.

System	Configuration	Atomic U_{eff}	Molecular U_{eff}
CeF_3	$4f^1$	12.88	6.28
GdF_3	$4f^7$	16.35	10.21
LuF_3	$4f^{14}$	17.55	18.78

It is important to note that these U_{eff} values were estimated to use in the AE-DKH-PBE level with the basis set and grid settings given in Table 4.1. However these values can be used in other GGA or LDA calculations employing as a first approximation. It has been found in test calculations that these values are not much dependent on the methodology. For example, in various LDA and GGA approximations, the optimal U_{eff} value for the $4f$ shell of LuF_3 was found to lie in the narrow range of $17-19$ eV. This is perhaps due to the fact the SIE in orbital energies in LDA and GGA calculations are of similar magnitude.

Unlike the $4f$ orbitals of lanthanides, $5f$ orbitals of uranium are semi-localized and they

participate in bonding. Thus estimating U_{eff} based on orbital energies is rather difficult. In the DFT + U applications to uranium systems, various U_{eff} values have been employed that are available in the literature. Based on the formal oxidation state of the U atom in these systems, all these values lie in the range of 1–5 eV. In a solid state calculation of uranium oxide [106], the optimal value of $U_{\text{eff}} = 4.3$ eV was used to reproduce the experimental band gap of 2 eV. A U_{eff} value of 1.5 eV was employed in the solid state calculation of UPd_3 [107]. The methodology employed in the above mentioned studies are slightly different from one another and from the methodology used in the present work. One of the reasons for the remarkable success of the DFT + U methodology so far in the solid state calculations lies in the fact that these U_{eff} values used for a specific system in a chosen method is meaningful, hence the U_{eff} used in a method can be used as a starting point in a different calculations and then the value can be fine tuned.

Table 4.5: Estimate of U_{eff} of the U $5f$ shell in uranyl complexes using first and second vertical ionization potentials (IP) of UO [a] and UO_2 [b] from ΔSCF [c] PBE, PBE+U calculations in comparison to experiment. All energies in eV.

		IP					
	Formal		PBE + U				
System	configurations of U	Exp.	U_{eff}	0	1	2	3
UO	$5f^3 7s^1 \rightarrow 5f^3$	6.03 [d]		6.27	6.28	6.29	6.32
UO^+	$5f^3 \rightarrow 5f^2$	12.7±0.8 [e]		13.33	12.72	12.08	11.41
UO_2	$5f^1 7s^1 \rightarrow 5f^1$	6.13 [d]		6.22	6.23	6.23	6.24
UO_2^+	$5f^1 \rightarrow 5f^0$	14.6±0.4 [e]		15.08	14.84	14.60	14.36

[a] UO_2 and its cations: D_{8h} point group symmetry.
[b] UO and its cations: C_{8v} point group symmetry.
[c] Spin multiplicity was fixed in all spin-unrestricted calculations.
[d] Ref. [108]
[e] Ref. [109]

In the present work, for the application of the DFT + U methodology to uranium systems, U_{eff} of the U $5f$ level was estimated reproducing the experimental ionization potentials of the molecular species UO^+ and UO_2^+ through Δ SCF calculations. This procedure covers the formal oxidation states U(III) to U(VI). Table 4.5 presents the U_{eff} values estimated for the U $5f$ level is UO^+ and UO_2^+. With the error margins of the experimental results as well as the relatively weak dependence of the target quantities on U_{eff} and the low value of the latter quantity, a value from 1.0 eV to 2.0 eV seems acceptable, depending on the oxidation state and the coordination of the uranium center. In the DFT + U applications of U(VI) systems that are based on the UO_2^{2+} moiety i.e. uranyl the narrow range of 1.0 eV to 2.0 eV was considered as an optimal range.

However, as previously mentioned, DFT + U calculations were performed for a range of U_{eff} values that covers the optimal value.

Chapter 5

DFT + U Application to Lanthanides

The third group of the periodic table contains the metals scandium (Sc), yttrium (Y), lanthanum (La) and actinium (Ac). The family of metals called the *lanthanides* form an inner transition series (atomic number 57-71) which lie inside the principal transition series. The valence electronic configuration of the lanthanide atoms is given as $[\mathrm{Xe}]\ 4f^n\ 6s^2\ 5d^1$. Sc, Y along with the lanthanides are also called *rare earth metals*. The valence assignments of lanthanides are largely deduced from experimental atomic volume data [110]. Starting from the first member of the lanthanides (La) until the last member (Lu) there is a gradual decrease in atomic volume from La to Lu which indicates that most of the lanthanides have same oxidation state (Ln^{3+}). Thus going from La to Lu, the atomic radii decreases from 187.7 pm for La to 173.4 pm for Lu (and ionic radii from 103.2 pm for La^{3+} to 86.1 pm for Lu^{3+}) and this phenomenon is known as *lanthanide contraction* [111]. Exceptions to this trend are Eu and Yb which show anomalously large volume, hence large atomic/ionic radii because of their tendency to be stabilized in a divalent state. The lanthanide contraction is attributed to the poor shielding of nuclear charge by $4f$ electrons. In many-electron atoms, as electrons are added in an outer shell, electrons already present in the same shell and those present in the inner shells, shield the newly added electrons from the nuclear charge. This *shielding effect* decreases with the increase in the angular quantum number (l) of the orbitals in the order $s > p > d > f$. Thus the $4f$ orbitals which show more directionality (*i.e.* increase in the angular quantum number) provide poor shielding to outer electrons ($5d^1\ 6s^2$, hence the decrease in atomic radii) and to f orbitals of the same shell (hence decrease in ionic radii). At this point one should note that with increasing atomic number Z, *relativity* has a *direct effect* of radial contraction of s and p orbitals which increases the shielding due to these orbitals. This increase in shielding or screening of the nuclear charge due to s and p electrons has an *indirect effect*: it induces a radial expansion of d and f orbitals [112–114].

A number of lanthanide (Ln^{3+}) complexes are colored, where the color arises from f-f tran-

sitions. The metallic conductivity of the rare earth metals arises from the delocalized 6*s* and 5*d* electrons but the magnetic moment results from the localized $4f$ electrons. Except for La^{3+} and Lu^{3+} which are diamagnetic all other Ln^{3+} ions with unpaired $4f$ electrons are paramagnetic. In a lanthanide complex or molecule, the $4f$ orbitals do not participate directly in bonding thus the ligand environment only slightly influences the spectroscopic and magnetic properties of lanthanide complexes, in contrast to transition metal compounds where the effect of the *ligand field splitting* is substantial. In fact the $4f$ orbitals of lanthanides are buried deeply below the 5*s* and 5*p* shells of the [Xe] core and provide very little overlap with the ligand orbitals [111].

The main objective of the present chapter is to discuss the application of the DFT + U methodology to lanthanide complexes both to understand the role of $4f$ electrons in lanthanide complexes and to provide an improved DFT description of $4f$ electron systems. The chapter is organized into two sections.

Section 5.1 focusses on the application of the DFT + U methodology as a tool to probe self-interaction artifacts in KS-DFT calculations and to understand bonding aspects of lanthanide trifluorides. Within this section, Subsection 5.1.1 focuses particularly on the role of $4f$ orbitals in the bonding of lutetium trifluoride (LuF_3) [25]. In Subsection 5.1.2 the role of 5*d* orbitals in the bonding of LaF_3, GdF_3 and LuF_3 is briefly outlined.

In Section, 5.2 preliminary results of a DFT + U investigation to model ceria nano-particles are presented.

5.1 Lanthanide Trifluorides

The molecular properties of lanthanide (Ln) complexes have been the subject of intense discussions in quantum chemistry [115]. Understanding the properties of lanthanide molecules in the gas phase is crucial for appreciating the behavior of Ln complexes in the solid state and of actinide complexes. For this purpose, the trifluorides of lanthanides LnF_3 are representative systems. They have been subjected to a number of experimental [116–118] and theoretical investigations, the latter ranging from semi-empirical calculations [119] to DFT-based studies [120–123] and high-level *ab initio* [124–126] works. Two major physical effects that challenge the theoretical modeling of Ln complexes are relativistic effects and dynamic correlation. As further complication, spin-orbit interaction arises in a proper relativistic description, but it can be neglected in a first approximation, at least if one focuses on structures, especially for the systems with the Ln $4f$ shell empty (La $4f^0$), half-filled (Gd $4f^7$), or completely filled (Lu $4f^{14}$) [127]. An important feature of the LnF_3 molecules is the geometry. It is of considerable interest [117] to know the role of participation of $4f$ and 5*d* orbitals in the appearance of pyramidal rather

than planar geometries of lanthanide trihalides. The molecular structure of lanthanide trihalides is often related to the ionic nature of the Ln-X bond [121] which exhibits some covalent contributions of Ln 5*d* and 6*s* orbitals [117]. Early pseudo-potential studies were quite successful, even without explicitly treating the $4f$ shell [115]. However, a simple model related the asphericity of an incompletely filled $4f$ shell to the preference for planar or pyramidal shape of Ln trihalides [128]. Such simple models are possible due to the semi-core nature of the compact $4f$ shell in lanthanide atoms. Furthermore, the radial extent of the $4f$ shell and, to a lesser degree, the atomic radii of the lanthanides are subject to the *lanthanide contraction* [112].

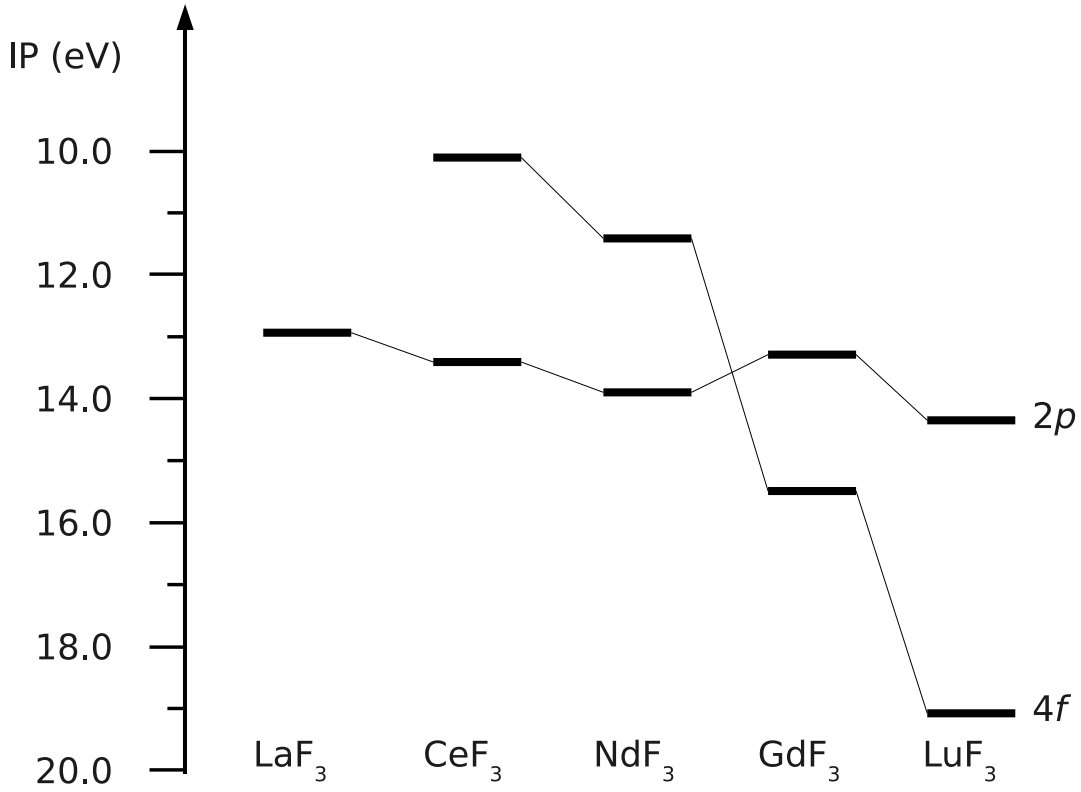

Figure 5.1: Trend of the ionization potential, IP (in eV) of the weighted center of the density of states of the Ln $4f$ and F $2p$ shells in LnF_3 where Ln = La(f^1), Ce(f^2), Nd(f^3), Gd(f^7) and Lu(f^{14}) based on photoelectron spectra [105].

5.1.1 Role of $4f$ Orbitals in the Bonding of LuF_3

The compact and completely filled $4f$ shell of *lutetium* (Lu) represents a challenge for standard exchange-correlation functionals in regard to the self-interaction error [131, 132]. The well-known underestimation (by absolute value) of eigenvalues in standard Kohn-Sham (KS) calcu-

lations [133] due to the insufficient cancellation of the self-interaction energy, accompanied by the relativistic destabilization of the $4f$ orbitals [134], places the Lu $4f$ orbital energies of LuF_3 in the same range as the $2p$ orbitals of the F ligands. Yet, in the photo-electron spectrum of LuF_3 [105], the F p-like ionization energies, 13.7–14.9 eV, are well separated from the Lu f-like ionization potentials (IPs), 18.4–20.1 eV (see Figure 5.1).

A recent all-electron (AE) zero-order relativistic approximation (ZORA) DFT study [123] of LnX_3 complexes (X = F, Cl, Br, I) yielded highly pyramidal structures for GdF_3 and LuF_3 which in the case of LuF_3, in part, was related to a considerable mixing of Lu $4f$ orbitals with the F $2p$ orbitals. Yet, the increasing pyramidal shape of Ln trifluorides with F-Ln-F bond angles of 113.6°, 106.8° and 101.4° for Ln = La, Gd, and Lu, respectively, is at variance with the results of other calculations where the F-Ln-F angle increases toward the end of the Ln series, approaching 120° of a planar structure [118].

The quasi-resonance condition between the Lu $4f$ and the F $2p$ levels, though apparently an artifact of conventional KS methods, may be the reason for pronounced f-covalency, observed by Clavaguéra et al. [123]. Even in that case, from a simplified view of the bonding, one would expect the interaction between the closed $4f$ shell of Lu(III) and the closed $2p$ shells of three F^- centers to be at most non-bonding, if not repulsive. Interestingly Dolg et al. noted in KS calculations of GdF that the Gd $4f$ orbitals mix with F orbitals and they related this mixing as a consequence of an artificial quasi-resonance condition due to high-lying Gd $4f$ levels as result of an insufficient self-interaction cancellation in standard exchange-correlation functionals [135].

Thus the case of LuF_3 forms an ideal case to demonstrate that the Lu $4f$-F $2p$ orbital mixing in KS calculations of LuF_3 is not relevant to the chemical bonding by showing that removal of this spurious orbital mixing does not affect the important experimentally observable molecular properties.

5.1.1.1 Results and Discussion

Molecular Properties of LuF_3

The AE DKH PBE and AE DKH PBE + U geometrical parameters of LuF_3 along with the atomization energy, the vertical IP, and the energy of the HOMO are collected in Table 5.1. Results from other calculations such as the semi-empirical INDO method [119], the PBE method (with an effective core potential for Lu) [120], the AE ZORA PBE method [123], the hybrid DFT methods PBE0 [120] and B3LYP [121], as well as results from wave function based methods such as CISD + Q [124], CCSD(T) [125], and CASSCF/CASPT2 [126] are reported, along with experimental results [105, 116, 129]. Although all high-level calculations predict the equilibrium

Table 5.1: Calculated properties of LuF_3 at AE DKH PBE and AE DKH PBE + U levels[a] along with results from other methods: Hubbard parameter U_{eff}, equilibrium bond length r_e (pm), F-Lu-F angle θ (°), atomization energy D_e (eV), ΔSCF vertical ionization potential IP (eV), and the negative of the energy ε_{HOMO} of the HOMO (eV).

Method	U_{eff}	r_e	θ	D_e	IP	$-\varepsilon_{HOMO}$
AE DKH PBE[b]		196.9	117.0	21.29	12.06	8.50
AE DKH PBE + U[b]	1.0	197.0	117.1	21.29	12.09	8.57
	2.0	197.0	117.2	21.29	12.11	8.61
	5.0	197.0	117.3	21.28	12.16	8.68
	10.0	197.1	117.5	21.27	12.19	8.72
	15.0	197.2	117.6	21.26	12.21	8.73
	18.0	197.2	117.7	21.25	12.21	8.74
	20.0	197.2	117.7	21.25	12.21	8.74
INDO[c]		204.5	107.4			
PBE[d]		199.5	118.0			
PBE0[d]		198.3	119.0			
B3LYP[e]		199.1	118.9			
AE ZORA PBE[f]		196.9	101.4			
CISD+Q[g]		196.5	120.0	18.21		
CCSD(T)[h]		197.4	120.0			
CASPT2[i]		196.1	120.0	20.52		
Exp.[j]		196.8	120.0	18.44	13.75	

[a] Point group symmetry of the molecule: C_{3v}.
[b] This work.
[c] Ref. [119].
[d] Ref. [120].
[e] Ref. [121].
[f] Ref. [123].
[g] Ref. [124].
[h] Ref. [125].
[i] Ref. [126].
[j] r_e and θ - Ref. [116], IP - Ref. [105], D_e - Ref. [129].

bond length in the range 196.1–197.4 pm, which is very close to the experimental value, 196.8 pm, one notes some interesting differences. All *ab initio* wave function based methods predict a planar geometry, with the bond angle F-Lu-F at 120° [124–126]. Most DFT based methods [120, 121], including the present work, predict a pyramidal geometry for LuF_3, with the F-Lu-F bond angle 2-3° smaller than 120°; that decrement is slightly smaller, 1°, with the hybrid DFT methods PBE0 and B3LYP [120, 121]. In that regard, the PBE calculations by Clavaguéra et al. form a singular exception where this decrement is as large as 19° [123]. In this context, it is

interesting to note that in the present calculations the energy barrier between the two equivalent pyramidal configurations through the planar transition state was less than 1 kcal/mol, in close agreement with other DFT calculations [120]. The AE DKH PBE structure of LuF_3 is a rather flat pyramid, with the Lu-F bonds forming an angle of 101° against the normal (C_3 axis) of the F_3 plane. Clavaguéra et al. [123] related the strong pyramidalization to the participation of $4f$ orbitals in metal-ligand bonding due to Lu $4f$-F $2p$ mixing. In contrast, a very recent CASSCF/CASPT2 study [126] yielded a planar structure of LuF_3 with an inert Lu $4f$ core. Further support for the essential planarity of LuF_3, is provided by other recent theoretical studies (Table 5.1); for a discussion of general geometric trends of metal halides, see Ref. [136].

From Table 5.1, one notes that an increase of U_{eff} up to 20 eV does not affect the structure and the calculated energetics in a chemically significant way. When comparing the results from a standard PBE calculation (U_{eff} = 0 eV) and a PBE + U calculation with the optimum value U_{eff} = 18 eV, very small changes of key parameters already suggest that Lu $4f$ contributions to the MOs will not play an important role in the bonding. Results from these two calculations differ only by 0.3 pm for the Lu-F bond length of 197.2 pm and 0.7° for the F-Lu-F bond angle of 117°. Likewise, the atomization energy D_e = 21.3 eV at U_{eff} = 0 eV decreases by a mere 0.05 eV on going to U_{eff} = 18 eV; the experiment suggests a significantly lower value of 18.4 eV. Similarly, the ΔSCF result for the first vertical ionization energy, 12.2 eV, and the negative of the energy of the HOMO, 8.7 eV, increase by 0.15 and 0.24 eV, respectively, in the PBE + U calculation. The experimental estimate for the IP of LuF_3 is 13.75 eV [129]. Whether or not Lu $4f$ and F $2p$ contributions mix in the MOs of LuF_3 does not seem to affect the calculated structural parameters of the molecule.

Atomic Charges and Orbital Analysis of LuF_3

In the following, the nature of the Lu-F bond and the role of $4f$ electrons in particular is discussed. First the atomic charges from PBE and PBE + U calculations are compared to identify possible consequences of the atomic localization of the Lu $4f$ orbitals. Table 5.2 lists Mulliken (q^M) and potential derived charges (q^{PD}) along with the populations of the valence atomic orbitals.

The Mulliken charge of Lu, 1.57 e, does not change in the PBE + U calculation. The potential derived charge (q^{PD}) of Lu and the population of the f shell increase by a negligible amount, 0.01 e. The $4f$ orbitals contribute 13.98 e to the total population of 14.10 e of the f shell; the excess is from Lu $5f$ and higher lying contractions. In summary, enforcing localization with the help of a Hubbard term does not change the overall picture regarding the charge on the Lu atom and the effective occupations of the Lu f shell and the F p shell. This finding further strengthens the

assertion that the spurious mixing of Lu $4f$ and F $2p$ orbitals in a standard KS calculation does not affect the character of the Lu-F bonds.

As the most notable effect of the Hubbard term, the one-electron energies of the Lu $4f$-like orbitals are significantly shifted downward and the Lu $4f$-F $2p$ mixing is removed (see Figure 5.2 and Table 5.3). The average energy of the Lu $4f$ manifold drops from approximately -10 eV at the PBE level to -18.5 eV at the PBE + U level.

Figure 5.2 shows the partial DOS of LuF3 in the range from -8 to -20 eV, resolved for the Lu $4f$ and F $2p$ contributions. The figure covers the manifolds of MOs with Lu $4f$ and F $2p$ character; there is also a slight Lu $5d$ contribution to the F $2p$ band. In the total DOS obtained from the AE DKH PBE calculation (U_{eff} = 0 eV) at the equilibrium geometry, the Lu $4f$ and the F $2p$ levels fall in the same narrow range of about -8.5 to -10.5 eV. The sharp peak from -10.0 to -10.4 eV corresponds to the Lu $4f$ orbitals. When the U_{eff} value is raised to 18 eV in the AE DKH PBE + U calculation, as expected, the center of the $4f$ band moves downward by 8.5 eV (Figure 5.2). With the introduction of the Hubbard term, the F $2p$ band shifts down, now ranging from -8.7 to -9.7 eV as compared to originally from -8.5 to -9.5 eV (Table 5.3). Figure 5.2 graphically indicates that the mixing of Lu $4f$ and F $2p$ states, as obtained in the AE DKH PBE calculation, is removed in the AE DKH PBE + U calculation.

Table 5.3 quantifies the mixing of Lu $4f$ and F $2p$ orbitals upon formation of the MOs of LuF_3. In C_{3v} symmetry the seven $4f$ orbitals of the central Lu atom reduce as $2a_1 + 1a_2 + 2e$ and the nine $2p$ orbitals of three F ligands split as $2a_1 + 1a_2 + 3e$. The Lu $4f$-F $2p$ mixing in the MOs of LuF_3 is essentially removed for the physically meaningful value U_{eff} = 18 eV. However, the Lu $4f$ orbitals undergo a very significant localization, to 90-95 %, already for the very small value U_{eff}. This observation strongly suggests that a very small reduction of the remaining $4f$ self-interaction error, affected by the Hubbard term with U_{eff} = 1 eV, suffices to lift the near degeneracy of Lu $4f$ and F $2p$ levels and to cancel their mixing. The whole situation in a standard KS calculation of LuF_3 indeed is very characteristic of an accidental degeneracy of two

Table 5.2: Mulliken charge q^M and potential derived charge q^{PD} of Lu in LuF_3 as well as orbital populations per atom (in e).

Method	q^M	q^{PD}	Lu					F	
			5*s*	5*p*	4*f*	5*d*	6*s*	2*s*	2*p*
AE DKH PBE	1.57	1.81	1.98	5.95	13.98	0.96	0.24	1.79	5.70
AE DKH PBE + U[a]	1.57	1.82	1.98	5.95	13.98	0.95	0.24	1.79	5.70

[a] U_{eff} = 18.0 eV for the $4f$ shell of Lu.

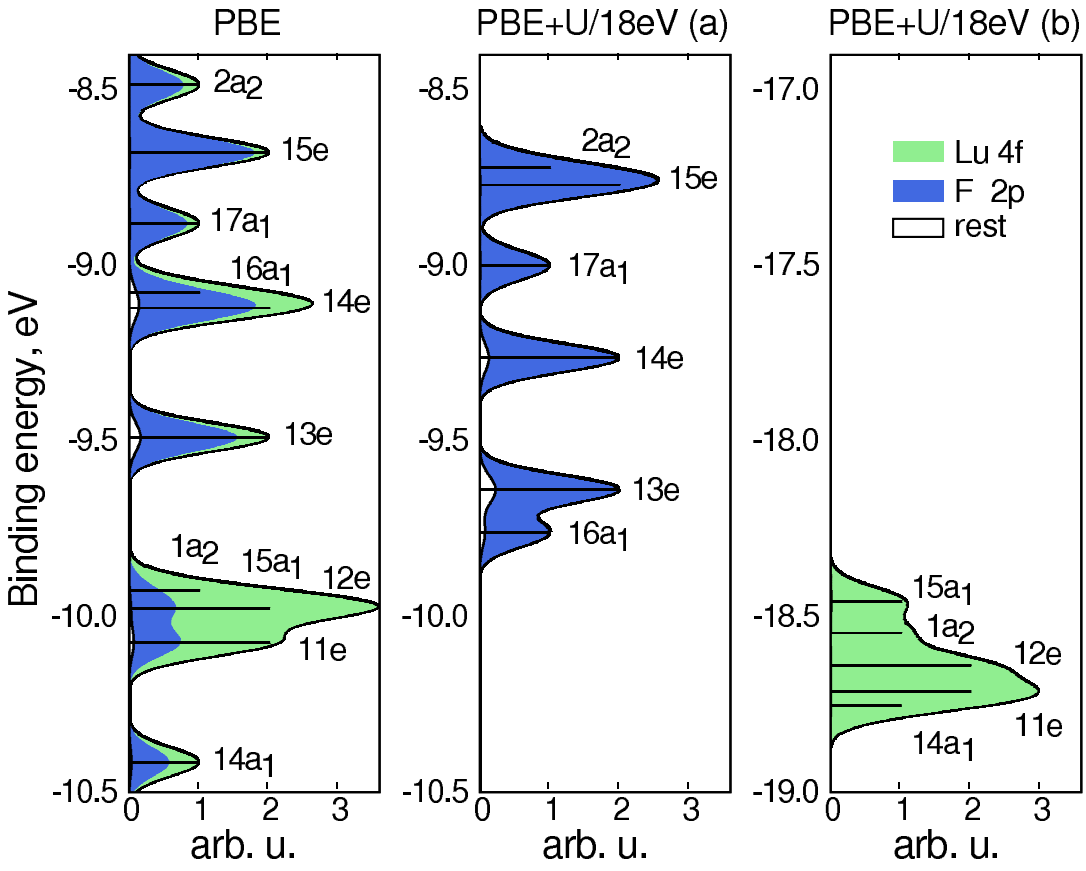

Figure 5.2: Partial density of states (DOS) for Lu $4f$ (green), F $2p$ (blue), and other orbitals (white) of LuF_3 in the energy range -8 to -20 eV as obtained from AE DKH PBE and AE DKH PBE + U calculations, the latter with U_{eff} = 18.0 eV for the $4f$ shell of Lu. The absolute positions of the levels and their degeneracies are given by the horizontal lines. For easier comprehension, this line spectrum is broadened into a DOS by folding with a Gaussian distribution with a full width at half maximum of 0.09 eV.

Table 5.3: Orbital mixing of the valence molecular orbitals (MOs) of LuF_3:[a] energies ε_i (eV) and Mulliken atomic gross populations (as %).

MO	AE DKH PBE				AE DKH PBE + U[b]			
	ε_i	Population			ε_i	Population		
		Lu *d*	Lu *f*	F *p*		Lu *d*	Lu *f*	F *p*
$2a_2$	-8.49		22.5	77.9	-8.73		2.2	97.9
15e	-8.69	0.2	10.2	89.1	-8.78	0.1	0.3	99.1
$17a_1$	-8.89	0.1	16.9	81.7	-9.01	0.5	0.5	98.0
$16a_1$	-9.09	2.3	54.0	41.3	-9.77	3.6	1.2	91.0
14e	-9.13	5.5	22.7	71.5	-9.27	6.4	0.5	92.8
13e	-9.50	7.6	22.6	69.1	-9.65	10.2	0.2	88.3
$1a_2$	-9.94		79.0	20.9	-18.56		99.3	0.6
$15a_1$	-9.99	0.3	86.2	13.3	-18.47	0.1	97.9	0.8
12e	-9.99	0.7	80.0	19.0	-18.65	0.0	99.5	0.3
11e	-10.09	2.8	64.6	32.0	-18.72	0.0	99.5	0.3
$14a_1$	-10.42	1.5	42.8	53.7	-18.76	0.0	99.6	0.2

[a] Point group symmetry of the molecule: C_{3v}.
[b] U_{eff} = 18.0 eV for the $4f$ shell of Lu.

completely filled manifolds, here the Lu $4f^{14}$ and the F $2p$ band which is formally completely filled with 18 electrons. For the MOs of the symmetry type a_1, the removal of Lu $4f$-F $2p$ mixing is illustrated in Figure 5.3 where at the PBE + U level, almost complete localization of the two f-like orbitals can be seen. These two f orbitals are the f_{z^3} and the $f_{x(x^2-3y^2)}$ orbitals both transform according to the a_1 irreducible representation of the C_{3v} point group (here the C_3 axis of LuF_3 coincides with the z-axis).

Table 5.4: Relative radial expectation value ($\Delta\bar{r}$, in pm) of quasi-atomic $4f$-like molecular orbitals (MOs) of LuF_3 w.r.t the radial expectation value $\bar{r}$ of $4f$ orbitals of Lu^{2+} cation[a].

MO	AE DKH PBE	AE DKH PBE + U[b]
$14a_1$	1.00	0.39
$15a_1$	0.58	0.05
$1a_2$	0.82	0.28
11e	0.55	0.36
12e	0.62	0.31

[a] $\bar{r}$ of Lu, Lu^+, Lu^{2+} and Lu^{3+} are 38.35, 38.17, 38.06 and 37.92 pm respectively.
[b] U_{eff} = 18.0 eV for the $4f$ shell of Lu.

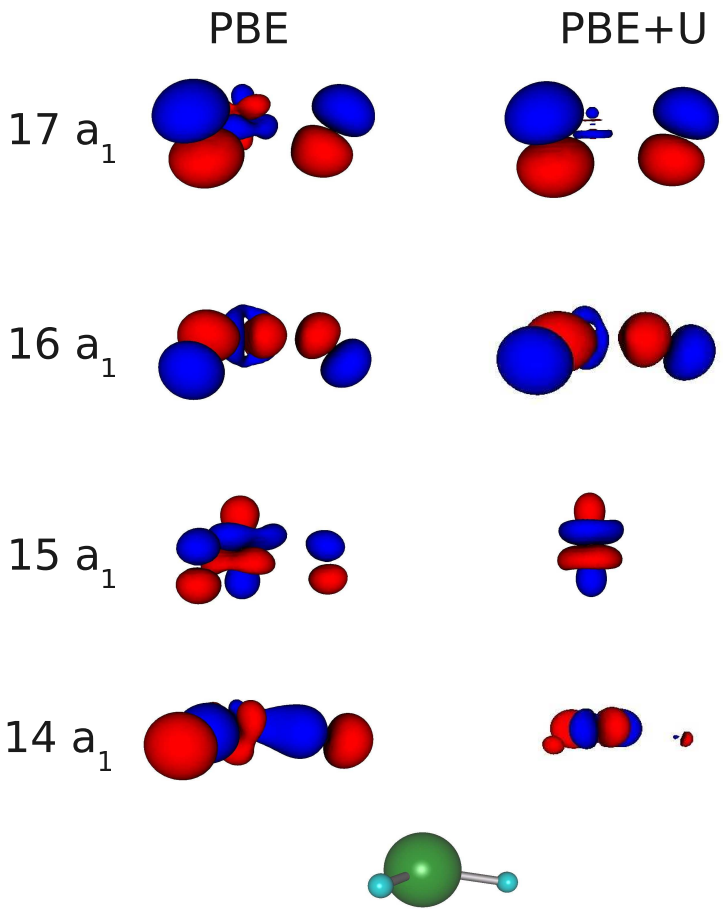

Figure 5.3: Lu $4f$-F $2p$ mixing in the AE DKH PBE calculation and its removal in the AE DKH PBE + U calculation (U_{eff} = 18.0 eV) shown for the MOs of the symmetry type a_1. The pyramidal structure of the LuF_3 molecule (bottom) is shown for reference.

Finally, to exemplify the concept of spatial localization of the $4f$ orbitals as enforced by the the Hubbard parameter U_{eff}, radial extension of the quasi Lu $4f$-type orbitals is LuF_3 is discussed. To quantify this (small) effect, the radial extension of the Lu $4f$-type orbitals of the Lu^{2+} cation is used as reference because the potential derived charge (q^{PD}) of the Lu center (see Table 5.2) in LuF_3 is close to +2. The radial expectation value of the $4f$ shell of this ion is $\bar{r}$ = 38.1 pm. The penalty of the Hubbard term for fractional populations makes the intra-atomic $4f$-$5f$ hybridization less favorable in a molecule. From Table 5.4 it can be seen that: in the AE DKH PBE calculation of LuF_3 the radial expectation values of the quasi-atomic $4f$ contributions are 0.62–1.00 pm larger than the reference. At the AE DKH PBE + U level, size and range of the deviations from the reference decrease as expected, to 0.06–0.39 pm.

5.1.1.2 Conclusions

Incomplete cancellation of self-interaction due to an approximate density functional of the standard variety results in Kohn-Sham eigenvalues lying too high in energy which, in LuF_3, leads to a metal-ligand orbital mixing owing to an accidental near-degeneracy. Care should be taken when interpreting such orbital mixing as a bonding situation. The DFT + U methodology proved to be a suitable tool for tuning the population and localization of orbitals and thus to probe the bonding situation. The Hubbard term included in the DFT + U scheme provides a simple procedure for exploring self-interaction artifacts such as those shown by the quasi-atomic Lu $4f$ orbitals. This scheme allows one to enforce orbital localization and thus to remove the spurious orbital mixing present in a calculation of LuF_3 with a standard gradient-corrected exchange-correlation functional. Overall it has been shown through this study that the presence or absence of the spurious mixing of Lu $4f$ and F $2p$ orbitals does not affect any of the observable molecular properties or formal atomic charges and previous claims of Lu $4f$ orbitals participating in the chemical bonding of LuF_3 cannot be uphold.

5.1.2 Role of 5*d* Orbitals in the Bonding of LnF_3

5.1.2.1 Results and Discussions

In Subsection 5.1.1, it has been shown how to interpret the Lu $4f$ - F $2p$ orbital mixing situation as seen in a standard KS calculation. Further it has been demonstrated that the $4f$ orbitals of Lu do not influence the structural and bonding features of LuF_3 significantly. However, both the DFT and DFT + U calculations predicted pyramidal structure for LuF_3 and in the present subsection, it will be shown that artifacts involving the Lu 5*d* orbitals are responsible for the pyramidal structures of LnF_3 where Ln = La, Gd and Lu.

The possible influence of the Ln 5*d* orbitals on the geometry of LuF_3 has been discussed in Refs. [117, 121, 130]. The situation of Ln 5*d* - F $2p$ mixing in LnF_3 is different from the Lu $4f$ - F $2p$ orbital interaction. Here the mixing of the formally unoccupied Ln 5*d*-like orbitals can also occur because of poor modeling of the wavefunction due to an incomplete basis set or poor choice of level of theory. Thus it should be noted that in the present context, the Ln 5*d* - F $2p$ mixing need not arise due to incomplete self-interaction cancellations but may also be a result of insufficient modelling of the Ln 5*d* orbitals which places the energy levels of Ln 5*d* orbitals close to the F $2p$ levels resulting in hybridization. Table 5.5 lists the geometry properties of LaF_3, GdF_3 and LuF_3 in AE DKH PBE and AE DKH PBE + U calculations along with results from the hybrid DFT methods PBE0 [120] and B3LYP [121] as well as from the wave function based methods MP2 [137] and CISD+Q [124]. In the AE DKH PBE + U calculation, a value of 2.0 eV

was used for the Hubbard parameter U_{eff} of the Ln 5*d* shell. From Table 5.5, one can clearly see a slight elongation of Ln-F bond lengths in the AE DKH PBE + U level when compared to the AE DKH PBE level for all the three molecules. This is a characteristic of the Hubbard term which disfavors weak ionic interactions that lead to fractional occupation numbers. From the values of the angle of deviation of the Ln-F bond from planarity, it is clear that at the most accurate level of theory considered here i.e. CISD + Q [124], the geometry of the LnF_3 molecules is planar. At the PBE level, all the three lanthanide fluorides have non planar geometry. From the PBE values

Table 5.5: Structural properties of LnF_3 where Ln = La, Gd, Lu at PBE and PBE + U [a] levels along with results of other methods: equilibrium bond length r_e (pm), F-Ln-F angle θ (degree) and the angle between the Ln-F bond and the plane orthogonal to the three-fold axis ϕ (degree)[b].

System	Method	r	θ	ϕ
LaF_3	AE DKH PBE	212.1	113.4	15.2
	AE DKH PBE + U	215.3	120.0	0.0
	PBE0 [c]	217.4	113.9	14.6
	B3LYP [d]	216.1	115.1	13.0
	MP2 [e]	215.0	112.9	15.8
	CISD+Q [f]	215.9	120.0	0.0
GdF_3	AE DKH PBE	203.3	115.2	12.9
	AE DKH PBE + U	206.2	120.0	0.0
	PBE0 [c]	205.8	117.0	10.1
	B3LYP [d]	205.6	117.7	8.8
	MP2 [e]	206.0	117.8	8.6
	CISD+Q [f]	205.6	120.0	0.0
LuF_3	AE DKH PBE	196.9	117.0	10.1
	AE DKH PBE + U	199.2	120.0	0.0
	PBE0 [c]	197.7	119.3	4.8
	B3LYP [d]	199.1	118.9	6.1
	MP2 [e]	198.0	120.0	0.0
	CISD+Q [f]	196.5	120.0	0.0

[a] U_{eff} = 2.0 eV for the 5*d* shell of Ln.

[b] The angle of deviation of the Ln-F bond from planarity ϕ was calculated for a given value of θ as
$\phi = 90 - (180/\pi)\arccos\left[\left[\{2\cos(\pi\theta/180)+1\}/3\right]^{(1/2)}\right]$

[c] Ref. [120].

[d] Ref. [121].

[e] Ref. [137].

[f] Ref. [124].

of the F-Ln-F bond angles or from the angle between the Ln-F bond and the plane orthogonal to the three-fold axis ϕ, one notes that, going from LaF_3 to LuF_3, the structures approach a planar configuration. This trend is also followed by the high level methods such as the hybrid-DFT methods PBE0 and B3LYP, as well as the wavefunction based method MP2. At the MP2 level, only LuF_3 is predicted to be planar while LaF_3 and GdF_3 are predicted to be pyramidal. It is interesting to note that at the PBE + U level, for U_{eff} = 2.0 eV, all the three structures are predicted to be planar in agreement with the CISD + Q results.

Myers et al. [130] pointed out that the interaction between the metal $5d_{z^2}$ orbitals and the fluorine $2p$ orbitals is notably enhanced in the pyramidal configuration in LnX_3; this interaction is also discussed in Ref. [121]. For a more general discussion regarding the role of d orbitals as π-bonding acceptors see Ref. [138]. With the energy of the Ln $5d$ shell and F $2p$ favorable to interact, this situation in LnF_3 is similar to pyramidalization of NH_3 which can be explained as a consequence of second-order Jahn-Teller (SOJT) interaction (see Figure 5.4). A brief overview of the Jahn-Teller interactions and related structural distortions is discussed in the next chapter in Section 6.1. For a general discussion of orbital-interaction concepts related to geometric perturbations as in the case of second-order Jahn-Teller situations in small molecules one is referred to the works of Burdett and others [139–141].

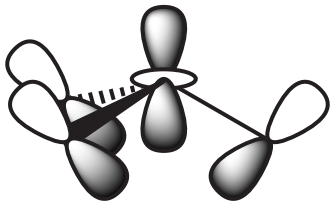

Figure 5.4: Ln($5d_{z^2}$)-F($2p$) interaction in the C_{3v} configuration

The Mulliken charge q^M on Ln (Ln=La, Gd and Lu) and the populations of the valence atomic orbitals of LnF_3 are listed in Table 5.6. Here one notes that for all three molecules, the Mulliken charge of Ln decreases by 0.1 e in the PBE + U calculation. This change in charge can be related to the population of the $5d$ orbitals which decreases by the same amount i.e. 0.1 e (Table 5.6) by shifting the (unoccupied) Ln $5d$ orbitals up in energy due to the Hubbard term, which in turn significantly removes the Ln $5d$ - F $2p$ mixing.

5.1.2.2 Conclusions

The above analysis identified an artificial second-order Jahn–Teller type artifact due to insufficient delocalization of the $5d$ orbitals resulted in a mixing with the ligand $2p$ orbitals which resulted in the pyramidalization of the LnF_3 molecules. The main objective of this section was

Table 5.6: Mulliken charge q^M of Ln (= La, Gd, Lu) in LnF_3 as well as orbital populations per atom (in e) from PBE and PBE + U calculations [a].

System	Method	q^M	Ln				F	
			5*s*	5*p*	4*f*	5*d*	2*s*	2*p*
LaF_3	PBE	1.76	1.96	5.97	0.21	0.89	1.87	5.68
	PBE + U	1.85	1.96	5.99	0.22	0.75	1.89	5.69
GdF_3	PBE	1.79	1.92	5.88	7.11	0.89	1.85	5.66
	PBE + U	1.86	1.92	5.89	7.13	0.75	1.86	5.69
LuF_3	PBE	1.57	1.98	5.95	13.98	0.95	1.79	5.70
	PBE + U	1.63	1.98	5.96	13.99	0.84	1.80	5.71

[a] U_{eff} = 2.0 eV for the 5*d* shell of Ln.

mainly to bring to attention the applicability of the DFT + U methodology as a probe tool to tune the orbital energies hence to tune the occupation of a particular shell of orbitals and to follow the results to gain more insight into the bonding aspects. The applications discussed in this subsection and the previous subsection illustrate the applicability of the DFT + U methodology to investigate structural and bonding aspects of lanthanide complexes. However, the DFT + U scheme is equally applicable to larger realistic systems. More often than not the prediction of reaction energies and excitation energies are of prime interest in real systems.

Theoretical modelling of $4f \rightarrow 5d$ excitations of lanthanide ions is both challenging and prospective. Accurate modelling of these excitations is important to study the photo-active properties of certain material which are doped with lanthanide ions. While modelling such systems is difficult even for high-level wavefunction based methods, modelling a realistic large-scale nanocluster is prohibitively expensive by wavefunction based methods. As discussed in the previous subsection 5.1.1, self-interaction artifacts complicate accurate modelling of $4f$ orbitals while delocalization artifact due to poor modelling also lightly affects the 5*d* orbitals. To identify and quantify both such artifacts and to provide an accurate description, the DFT + U methodology forms an suitable model.

5.2 Ceria Nanoparticles

Ceria or cerium oxide is widely used as a supporting metal in heterogeneous catalysis. The advantages of ceria over other materials, specifically over other lanthanide materials are due to the ability of the Ce $4f^1$ electron to show valence transitions as discussed in Chapter 1. There is

an enormous amount of literature on the theoretical and experimental study of ceria [143–148]. This section will serve the purpose of both reviewing the basic concepts as explored during the course of this thesis project and to summarize the results of a preliminary DFT + U investigation to model ceria nanoparticles. In the following introductory review only properties and other details related to Ce $4f$ electron will be discussed.

CeO_2 or Ce(IV) oxide is the most stable phase of ceria at room temperature and under atmospheric conditions [147]. Another commonly discussed form of ceria is the fully reduced form which is represented by the stoichiometric formula Ce_2O_3 [1] (see for example Ref. [147]). Oxygen vacancy on the surface of ceria often play a vital role in large-scale applications of ceria. The concept of oxygen vacancy in ceria is related to the Ce^{3+}/Ce^{4+} redox process of Ce atom as follows: In the stoichiometric cerium oxide CeO_2, all valence Ce states (i.e. $4f^1 6s^2 5d^1$) are empty implying a Ce^{4+} oxidation state. The partially reduced form of ceria Ce_nO_{2n-x} is formally created by removing oxygen atoms. In other words, for every removed lattice oxygen ion, two electrons are left behind to create two Ce^{3+} centers close to the site of the vacancy [143, 146]. In CeO_2, the empty Ce $4f$ band is located between occupied O $2p$ band and the unoccupied Ce $5d$ band while in the partially reduced ceria, a localized partially-occupied $4f$ band is located below the unoccupied $4f$ band [143].

The number of oxygen vacancy centers in ceria is directly related to the ratio between the numbers of Ce^{3+} and Ce^{4+} centers. The ability of ceria to store and release oxygen is related to its ability to change the oxidation states of the cerium centers between III and IV by accepting of releasing the $4f$ electron. This property has its effect in improving catalytic converters where for the efficient conversion of the harmful gases such as CO to CO_2 the level of oxygen should be maintained optimally. Reactions involving catalysis by *gold* (Au) nanoparticles [143–145], such as room temperature oxidation of CO have been observed to be more efficient when the Au nanoparticles (npAu) are supported on ceria [148]. An oxidized form of Au has been known to be important in the chemisorption of CO on gold nanoparticles, npAu. Ceria nanoparticles ($npCeO_2$) as support stabilize the positive charge density on Au. X-ray photoelectron spectroscopy (XPS) of npAu/$npCeO_2$ indeed reveals the presence of Au in its common oxidation states I and III along with neutral gold species [148] which have been found to grow near the oxygen vacancy sites.

[1] The bulk properties of reduced ceria indicate that the actual stoichiometric formula is CeO_x where x=1.50 to 1.53.

5.2.1 Model Nanoparticles

Loschen et al. [149] designed a series of octahedral ceria nanoparticles and studied them using the plane wave DFT + U method. In their work they discussed the properties of the three nano-dimensional model clusters with the molecular formula $Ce_{19}O_{32}$, $Ce_{44}O_{80}$ and $Ce_{85}O_{160}$. Some of these particles were designed during the course of this thesis work and in the present subsection, the procedure adopted to design them will be briefly summarized.

Investigations using transmission electron microscopy (TEM) investigation showed that ceria nanoparticle single crystals with a dimension of a few nm have either an octahedral shape with eight(111) surfaces or with an additional (200) surface they acquire a truncated octahedral shape with a dimension of a few nm [150]. Thus one way to construct these nanoparticles will be to build an extended cubic CeO_2 framework and cut along the 8 (111) planes of the cube at various radial distance from the center of the cube to arrive at octahedral particles of various dimensions. By an experimental mathematical procedure a general molecular formula for these particles was invented during the present work as $Ce_{x_i}O_{y_i}$ where:

$$x_i = \frac{1}{3}\left(2(i+1)^3 + (i+1)\right); \quad y_i = \frac{4}{3} i\,(i+1)\,(i+2) \tag{5.1}$$

and i represents the number of shells of octahedral symmetry. Using the above equation a possible series of $npCeO_2$ clusters of octahedral symmetry for various values of i are listed in Table 5.7. One notes that as the particle dimension increases, the ratio between the number of O centers to the number of Ce centers approaches the bulk value of 2.0.

Table 5.7: Molecular formulae for a series of octahedral ceria nanoparticles.

i	$Ce_{x_i}O_{y_i}$	y_i/x_i
1	Ce_6O_8	1.333
2	$Ce_{19}O_{32}$	1.684
3	$Ce_{44}O_{80}$	1.818
4	$Ce_{85}O_{160}$	1.882
5	$Ce_{146}O_{280}$	1.918
6	$Ce_{231}O_{448}$	1.939
7	$Ce_{344}O_{672}$	1.953
8	$Ce_{489}O_{960}$	1.963
9	$Ce_{670}O_{1320}$	1.970
10	$Ce_{891}O_{1760}$	1.975
Bulk	Ce_nO_{2n}	2.000

The 6 Ce centers of the first cluster, if assumed to be symmetrically equivalent, exhibit a formal oxidation state of $+2.67$, implying the average configuration $f^{1.33}$. In the larger members

Ce^{3+} and Ce^{4+} centers can be symmetrically distributed: for example in the second member of this series, $Ce_{19}O_{32}$ a combination of 7 Ce^{4+} ions (1 at the center and 1 per each of the 6 vertices of an octahedron) and 12 Ce^{3+} centers (1 per each of the 12 edges of an octahedron) may result in a cluster as shown in Figure 5.5.

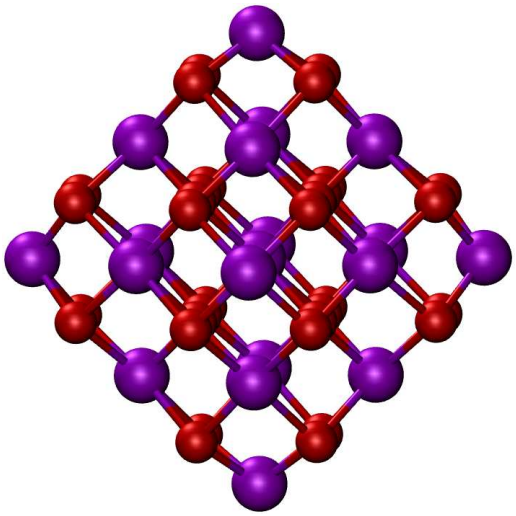

Figure 5.5: AE DKH VWN equilibrium configuration of the octahedral $Ce_{19}O_{32}$ nanoparticle (Ce-violet, O-red) with dimension 1.0 nm.

5.2.2 Results and Discussions

5.2.2.1 Exploratory Investigations

In preliminary DFT + U investigations, small molecules such as Ce_2O_3, Ce_5O_8 were studied to gain experience with convergence-related issues in DFT calculations of these systems. Modelling of these systems present difficulties of various types. Although modelling a delocalized state is not a problem for DFT, modelling a mixed-valence type state is more of a many-determinant problem where schemes like *broken-symmetry* DFT (BS-DFT) can partially alleviate the problem [152, 153]. In the DFT + U calculations however one can localize the f electrons in order to prevent converging to a delocalized state, but to do that very high, physically improper values for U_{eff} have to be chosen. A few useful conclusions which were drawn from exploratory calculations of model systems will be presented in this section which will be followed by the results and discussions of some successful calculations.

In the first implementation of the DFT + U methodology, a DFT + U mixing scheme was used where a fraction of the DFT + U potential of the $(i-1)^{th}$ iteration was added to the potential calculated at the $(i)^{th}$ iteration:

$$\tilde{V}^{\sigma}_{U,i} = w \cdot V^{\sigma}_{U,i} + (1-w) \cdot V^{\sigma}_{U,i-1} \tag{5.2}$$

A default value of 0.3 was used for the weight factor *w* which was later found to slow down the SCF convergence. In the subsequent versions of the DFT + U module the default value for *w* in Eq. 5.2 was changed to 1.0 with effectively no mixing, however *w* also can be fixed in a calculation as desired.

5.2.2.2 DFT + U Investigation of Ceria Nanoparticles

The difficulties presented by DFT and DFT + U modeling of ceria nanoparticles in the application of gold catalysis has been discussed in Refs. [151] and [143]. Zhang et al. [143] have summarized various key points which are of interest and found to have aided the subsequent investigation of the present thesis work. In previous DFT + U investigations, for the choice of U_{eff} of the Ce $4f$ shell, optimum ranges of values such as 5–6 eV and 3–4 eV have been favored in LDA + U and GGA + U calculations respectively (see Ref. [143] and other references there in).

The 51-atomic ceria nanoparticle (Figure 5.5) of the molecular formula $Ce_{19}O_{32}$ was chosen as a candidate for the main investigation. For the preliminary investigation the geometry was optimized with the AE DKH VWN method followed by single point AE DKH VWN + U calculations. As a preoptimization step various equilibrium geometries with differing Ce-O bond lengths were tested and improved convergence was noted for systems with moderately larger Ce-Ce bond lengths (360 pm) than models with shorter Ce-Ce bond lengths. In the AE DKH VWN + U geometry optimization Fermi-level broadening scheme was used with a Fermi energy window of 0.1 eV between HOMO and LUMO. Through AE DKH VWN single point calculations the Fermi energy window was found to take values up to 0.07 eV below which no SCF convergence was observed. In AE DKH VWN + U calculations using various U_{eff} values, Fermi energy window below 0.1 eV did not lead to SCF convergence. Further, in AE DKH VWN geometry optimization and AE DKH VWN + U single point calculations spin-only magnetic moment was fixed to have the value 12 *e* which formally corresponds to a system with an f^1 electron on each of the 12 Ce atoms located at the 12 edges of the octahedron and octahedral symmetry constraints were used. In the AE DKH VWN + U single point calculations, the converged AE DKH VWN density was used as starting guess density to speed up the SCF convergence.

Table 5.8 presents the results of a series of spin-unrestricted AE DKH VWN + U single point calculations of $Ce_{19}O_{32}$ performed for various values of U_{eff} in the range 0 to 6 eV at the AE DKH VWN geometry. The main property of interest here is to identify Ce^{3+} and Ce^{4+}-like centers. For this purpose the total population of $4f$ electrons on the Ce centers along with the energy of the Ce $3d$-like orbitals were studied. While the population of the Ce centers on a bulk system can be expected as f^0 in CeO_2 and nearly f^1 in the fully reduced Ce_2O_3, an indirect effect of the net charge of the Ce centers on the corresponding $3d$ shell has been found to aid the

identification of the character of Ce-atoms [149]. In the stoichiometric species CeO_2 where the Ce centers carry a formal +4 charge, the energy of the $3d$ orbitals (ε_{3d}) was found to be -867.0 eV from a projected augmented wave (PAW) method [149] and in the fully reduced ceria i.e. Ce_2O_3, with the decrease in the formal charge to +3, this energy ε_{3d} is shifted to -861.8 eV. It should be noted that $Ce_{19}O_{32}$ is only a small-scale representative of octahedral npCeO_2 but here one can clearly expect an approximate modeling of a npCeO_2.

From Table 5.8 one clearly notes that at the AE DKH VWN level (U_{eff} = 0.0 eV), a severe unphysical delocalization renders all three Ce-center to be identical. Although N^{α}, N^{β} and N^{α}+N^{β} were populated to various extents, the net spin population (N^{α}-N^{β}) was found to be $0.6\,e$ on all three types of Ce centers. The indirect effect of the charge of the Ce center on $-\varepsilon_{3d}$ clearly indicates that at the AE DKH VWN level all three Ce centers are identical with the corresponding $3d$ of about 865 eV for all three unique types of Ce centers located at the center, at edges and vertices of the octahedron. With increasing value of U_{eff}, the results have not systematically affected but one notes that sharply at U_{eff} = 5.0 eV, 12 f^1 electrons were localized at the 12 Ce centers located at the edges. It is also interesting to note that for the value of U_{eff} = 5.0 eV, the Ce centers at the center of the cluster and at the vertices are predicted to be in the oxidation state IV with no net spin polarization. However, the total $4f$ population of approximately 0.5 e of both spin type at the Ce atoms at the vertices indicate Ce-O covalent bonding. Again $-\varepsilon_{3d}$ serves as an excellent indicator of the oxidation states of the Ce centers. With increasing U_{eff}, to 6.0 eV, one can see that the Ce centers at the vertices tend to attain a +3 oxidation state by partially localization of $4f$ electrons which subsequently affects the $4f$ localization at the other centers. At this point it will only be pointed out that the DFT + U implementation in the LCGTO methodology of the code ParaGauss forms a suitable tool to investigate the ceria nanoparticles where the localization as modelled by the LCGTO framework may have certain advantages over other frameworks such as those based on plane wave basis.

Table 5.9 compares the net spin $4f$ populations and ε_{3d} of $Ce_{19}O_{32}$ from AE DKH VWN and AE DKH VWN + U calculations along with available results for $Ce_{19}O_{32}$, $Ce_{44}O_{80}$ and $Ce_{85}O_{160}$ systems and bulk ceria from Ref. [149]. From a comparison of results from AE DKH VWN + U and PAW VWN + U [149] calculations, it is clear that the PAW VWN + U calculation predicted a delocalized state where the Ce atoms at the edges (E) and vertices (V) are of similar oxidation states but the AE DKH VWN + U calculation (correctly) predicted 12 localized Ce centers at the edges. In general, for all three clusters $Ce_{19}O_{32}$, $Ce_{44}O_{80}$ and $Ce_{85}O_{160}$, the PAW VWN + U calculations predicted the number of Ce^{4+} centers correctly but for the Ce^{3+} centers, only partial localization was obtained. With the success of the AE DKH VWN + U methodology in the description of the $Ce_{19}O_{32}$ nanoparticle one can hope for an improved modelling of ceria

Table 5.8: AE DKH VWN, AE DKH VWN + U Spin specific Mulliken population of $4f$ orbitals per Ce atom in $Ce_{19}O_{32}$ (in e) [a] along with the negative of energy of the $3d$ orbitals -ε_{3d} (in eV): Populations of $4f$ electrons of majority spin-type N^{α}, population of $4f$ electrons of minority spin-type N^{β}, total population of $4f$ electrons N^{α} + N^{β}, net spin population of $4f$ electrons N^{α} - N^{β} were given along with various U_{eff} [b] values.

U_{eff}	Position [c]	N^{α}	N^{β}	N^{α} + N^{β}	N^{α} - N^{β}	$-\varepsilon_{3d}$
0.0	C	0.39	-0.24	0.16	0.64	865.8
	E	1.02	0.39	1.41	0.63	865.2
	V	0.99	0.38	1.37	0.61	865.2
1.0	C	0.22	-0.24	-0.03	0.46	866.9
	E	1.01	0.36	1.38	0.65	865.4
	V	0.99	0.34	1.33	0.65	865.3
2.0	C	0.03	-0.23	-0.20	0.26	868.1
	E	1.00	0.34	1.34	0.66	865.7
	V	0.97	0.31	1.29	0.66	865.5
3.0	C	-0.12	-0.25	-0.37	0.13	869.0
	E	0.98	0.31	1.30	0.67	866.0
	V	0.95	0.29	1.24	0.66	865.9
4.0	C	-0.26	-0.29	-0.54	0.03	869.8
	E	0.97	0.29	1.26	0.68	866.3
	V	0.93	0.26	1.19	0.67	866.3
5.0	C	0.01	-0.01	-0.01	0.02	869.6
	E	1.20	0.22	1.42	0.98	863.4
	V	0.49	0.48	0.97	0.01	869.8
6.0	C	-0.33	-0.29	-0.62	-0.04	870.9
	E	0.99	0.24	1.23	0.75	866.1
	V	0.77	0.25	1.02	0.52	868.1

[a] The equilibrium geometry as obtained from an AE DKH VWN calculation was used in all calculations.

[b] U_{eff} for the $4f$ shell of Ce.

[c] C - center (1 Ce atom), E - edge (1 Ce atom in the middle of each of the 12 edges), V - vertex (1 Ce atom at each of the 6 vertices).

nanoparticles using the methodology implemented in the this thesis in the framework of Para-Gauss.

Table 5.9: AE DKH VWN, PAW VWN + U and AE DKH VWN + U spin specific Mulliken population of $4f$ orbitals per Ce atom in various ceria models, along with the negative of energy of $3d$ orbitals -ε_{3d} (in eV) and results from other methods: Number of equivalent Ce atoms of each type n_i, net spin population of $4f$ electrons N^{α} - N^{β} (in e) are given.

System	Method	Position [a]	n_i	$-\varepsilon_{3d}$	N^{α} - N^{β}
$Ce_{19}O_{32}$	AE DKH VWN	C	1	865.8	0.64
		E	12	865.2	0.63
		V	6	865.2	0.61
$Ce_{19}O_{32}$	AE DKH VWN + U [b]	C	1	869.6	0.02
		E	12	863.4	0.98
		V	6	869.8	0.01
$Ce_{19}O_{32}$ [c]	PAW VWN + U [b]	C	1	868.0	0.01
		E	12	863.8	0.68
		V	6	863.6	0.69
$Ce_{44}O_{80}$ [c]	PAW VWN + U [b]	C	6	867.8	0.03
		E	24	864.6	0.56
		V	6	865.1	0.47
		F	8	867.7	0.02
$Ce_{85}O_{160}$ [c]	PAW VWN + U [b]	C	19	866.3	0.04
		E	36	863.2	0.41
		V	6	860.7	0.70
		F	24	866.2	0.03
CeO_2 [c]		bulk		867.0	0.00
Ce_2O_3 [c]		bulk		861.8	0.96

[a] C - center, E - edge, V - vertex, F - facet.
[b] U_{eff} = 5.0 eV for the $4f$ shell of Ce.
[c] Ref. [149].

Chapter 6

DFT + U Application to Actinides

The *actinide* series of metals belongs to the seventh period (atomic number 89-103) of the periodic table. The valence electronic configuration of the actinide series is $[\mathrm{Rn}]\ 5f^n\ 6d^1\ 7s^2$. When compared to the $4f$ orbitals of lanthanides, the $5f$ orbitals of actinides are relatively less compact. Localization of the $5f$ electrons gradually increases with the atomic number of the actinide element due to poor shielding of the nuclear charge by $5f$ orbitals and experimental studies indicate that starting from *americium* (Am, $5f^6$) the $5f$ orbitals become localized [110]. The $5f$ electrons of the early actinide elements such as *protactinium* (Pa, $5f^2$), *uranium* (U, $5f^3$), *neptunium* (Np, $5f^4$), plutonium (Pu, $5f^5$) are semi-localized (localized or more delocalized). Along with the valence $6d^1$ and $7s^2$ electrons, the $5f$ electrons of these elements can be easily removed or readily transferred to ligands, thus early actinides exhibit various oxidation states. In the present thesis, only uranium complexes with U oxidation state VI ($5f^0$) are considered. The purpose of this chapter is to discuss the application of DFT + U methodology to some U (VI) complexes.

Section 6.1 deals with the application of the DFT + U methodology to the UO_2^{2+} ion, an important ion; as a model study, the species will be treated in the gas phase. The main objective of this section is to discuss the essential geometric and electronic properties of UO_2^{2+} in KS-DFT and DFT + U descriptions. In this section, the nature of orbital interactions in UO_2^{2+} will be discussed with special emphasis on the role of U $5f$ orbitals in the bonding of UO_2^{2+}. The ideas developed in this section are then be used in the remainder of this chapter to rationalize the DFT description of related complexes and improvements provided by the DFT + U treatment. Both Sections 6.2 and 6.3 deal with the role of self-interaction error in the structural features of actinide complexes. In Section 6.2, results of a DFT + U study of the penta aqua uranyl complex are presented. Finally, in Section 6.3, results of a systematic study of the uranyl monohydroxide cation are summarized.

6.1 Uranyl Dication

The molecular species uranyl (UO_2^{2+}) has been studied with wide range of theoretical methods ranging from the simple extended Hückel method [154] to highly accurate coupled cluster calculations [155]. The uranyl dication is a very stable species exhibiting a linear geometry with a formal U-O bond order 3. The role of $5f$ orbitals in the linearity of uranyl is partly supported by the fact that the isoelectronic transition metal species MoO_2^{2+} is bent [159]. However, the isoelectronic actinyl ion ThO_2 (*thorium*, Th, Z = 90) is also bent ($\theta_{exp.} = 122^\circ$) [159] which indicates the role of factors other than $5f$ orbitals. The preference of the uranyl ion for linear geometry has been discussed by several authors (for a review see Ref. [156]).

In the earliest of these studies, Tatsumi and Hoffmann [154] based on extended Hückel calculations suggested that the sub-valence $6p$ orbitals [1] play a role in activating the O $p\sigma$ orbitals to form σ bonds with U $5f$ orbitals. Later in a relativistic Hartree–Fock–Slater study [157], this effect which is referred to as "pushing-from-below" [158], has been shown to be less significant in uranyl bonding. In a Hartree-Fock study employing a RECP, in order to explain the bent geometry of ThO_2, Wadt [159] suggested that the relative ordering of the $5f$ and $6d$ levels and not the $6p$ orbitals are important to describe the geometry. Subsequent investigations [160–162] established the ordering of the MOs of UO_2^{2+} and approximate contributions of uranium $5f$ and $6d$ atomic orbitals to these MOs. The near degeneracy of U $5f$ and $6d$ levels is understandable considering the relativistic destabilization of these orbitals to different extents [163] and it is this effect which energetically puts the U $5f$ orbitals at a suitable place to be involved in bonding with the O $p\sigma$ orbitals. Further, a situation similar to lanthanide contraction results in the decrease in ionic radii with increasing atomic number from Th (Z = 90) to Lr (Z = 103) which results in a net stabilization of the $5f$ orbitals with increasing atomic number (see Figure 5.1 for an analogous situation in the lanthanides).

In the following, the ground state electronic structure, equilibrium geometry and harmonic vibrational frequencies from AE DKH PBE and AE DKH PBE + U calculations will be discussed. Finally it will be shown that a second-order Jahn–Teller type situation exists in the UO_2^{2+} cation that is enhanced in KS-DFT calculations by the self-interaction artifacts related to the U $5f$ orbitals which are responsible for *softening* the uranyl bending mode.

[1] The electronic configuration of neutral U atom is [Rn] $5f^3\ 6d^1\ 7s^2$, where the $6p$ orbitals form the highest occupied MO of the [Rn] core.

6.1.1 Results and Discussions

Molecular properties of UO_2^{2+}

The coupled-cluster CCSD(T) and the hybrid-DFT B3LYP values [155] of the equilibrium uranyl bond length fall in the narrow range of 169.0–169.4 pm (Table 6.1). The PBE and PBE + U values are somewhat longer, 171.9–171.4 pm, and the GGA-BP value [164] is close to the PBE result (Table 6.1). Comparing the results of the PBE calculations to those obtained with the PBE + U method and U_{eff} = 2.0 eV, the uranyl bond distances are shortened by 0.5 pm so that the PBE + U value reproduces the B3LYP and CCSD(T) results better than the PBE value. In the PBE calculation, the energy of the highest occupied molecular orbital (HOMO) is -22.07 eV which decreases by approximately 0.2 eV when U_{eff} is increased by 1 eV. It will shown later that the HOMO of UO_2^{2+} represents a σ interaction between a U $5f$ orbital and the σ^* orbital of the dioxo (O_2^{4-}) $2p$ fragment. The U $5f$ orbital contributes 57 % to this bond which is slightly more than 50 %, thus the potential correction provided by the Hubbard parameter U_{eff} to this orbital will be negative. This effect will further increase the U $5f$ contribution with increasing values of U_{eff}; this is reflected in the stabilization of the $5f$ - $2p$ σ bond, hence results in a shortening of the U-O distance in PBE + U calculations. Further, in the PBE calculation, the energy of the lowest unoccupied molecular orbital (LUMO) is -19.78 eV; in the PBE + U calculations ε_{LUMO} increases by approximately 0.5 eV with U_{eff} increases by 1 eV. This is readily understood through Eq. (3.63) where the potential correction provided by the Hubbard parameter to an occupied orbital is +0.5 eV for the value of U_{eff} = 1.0 eV. Thus the HOMO-LUMO gap which is 2.29 eV in the PBE calculation (Table 6.1) increases by about 0.7 eV in the a PBE + U calculation when the the Hubbard parameter U_{eff} is enlarged by 1 eV.

The PBE values of the harmonic vibrational frequencies of the asymmetric and asymmetric stretching modes underestimate the corresponding CCSD(T) values [155] by 34 cm^{-1} and 16 cm^{-1}, respectively (Table 6.1). At the PBE + U level (U_{eff} = 2.0 eV), these frequencies are slightly corrected towards higher values, by 13 and 8 cm^{-1}. As for the structure results, one notes that PBE + U corrections tend to change in the direction of the CCSD(T) and the B3LYP predictions (Table 6.1) [155]. Quite a bit more distinct is the effect of DFT + U method on the frequency of the uranyl bending, which is 86 cm^{-1} lower at the PBE level, 92 cm^{-1}, than the CCSD(T) result of 178 cm^{-1} [155] (Table 6.1). Indeed, the PBE + U result for this quantity strongly depends on the Hubbard parameter U_{eff}. With U_{eff} = 1.0 eV, that bending frequency increases by 75 cm^{-1} compared to the PBE-GGA result, thus reproducing the B3LYP value. With U_{eff} = 2.0 eV, one obtains 211 cm^{-1} which is 119 cm^{-1} higher than the PBE result and even 33 cm^{-1} above the value of 178 cm^{-1} obtained with the CCSD(T) method [155] (Table

6.1). From these results one can conclude that U $5f$ orbitals play a role in uranyl bonding and when the localization of these $5f$ orbitals are tuned by the inclusion of a small positive Hubbard parameter U_{eff} between 1 and 2 eV, one obtains an improved description of structural properties of UO_2^{2+}.

Table 6.1: Calculated properties of UO_2^{2+} [a] at AE DKH PBE and AE DKH PBE+U levels along with results from other methods: Hubbard parameter U_{eff} (eV), equilibrium U-O bond length r (pm), energies of the the highest occupied molecular orbital (HOMO) ε_{HOMO}, lowest unoccupied molecular orbital (LUMO) ε_{LUMO} and their difference, the HOMO-LUMO gap $\Delta\varepsilon$ (eV), harmonic frequencies of the asymmetric stretching ω_a, the symmetric stretching ω_s and the bending ω_b vibrational modes (cm^{-1}).

Method	U_{eff}	r	ε_{HOMO}	ε_{LUMO}	$\Delta\varepsilon$	ω_a	ω_s	ω_b
AE DKH PBE [b]		171.9	-22.07	-19.78	2.29	1104	1001	92
AE DKH PBE + U [b]	1.0	171.7	-22.22	-19.26	2.96	1110	1005	167
AE DKH PBE + U [b]	2.0	171.4	-22.39	-18.75	3.64	1117	1009	211
AE DKH BP [c]		172.2				1091	994	93
RECP/B3LYP [d]		169.4				1137	1046	166
RECP/CCSD(T) [d]		169.0				1120	1035	178

[a] Calculations carried out with symmetry constraints according to point group D_{8h}.
[b] This work.
[c] Ref. [164].
[d] Ref. [155].

Atomic charges and orbital analysis of UO_2^{2+}

Table 6.2 lists the Mulliken charge q^M of U in UO_2^{2+} along with the populations of the valence atomic orbitals. The U center in UO_2^{2+} has a formal charge of +6 and the oxo fragments represent formally closed-shell dianionic ligand fragments. Through σ and π interactions each oxygen center donates 2.0 e (0.1 from $2s$, 1.9 from $2p$) to the U center which results in the U center having a net charge of about +2 e (Table 6.2). This is reflected in the PBE description of the Mulliken charge of the U center of UO_2^{2+}. A larger contribution of these σ and π donated electrons populates the U $5f$ orbitals (about 2.7 e) and the U $6d$ orbitals are populated by about 1.4 e which is almost half of the population of $5f$ orbitals. This reflects the different extents to which the uranium $6d$ and $5f$ orbitals involve in bonding. The $6p$ orbitals show a small deficit of about 0.2 e indicating a very small contribution to the bonding. The only change introduced in the PBE + U description is a very slight increase in the $5f$ population by 0.03 e for the U_{eff}

value 2.0 eV.

Table 6.2: Mulliken charge q^M of U in UO_2^{2+} as well as valence orbital populations per atomic center (in e).

Method	U_{eff}	q^M	U				O	
			7s	6p	6d	5f	2s	2p
AE DKH PBE		2.02	0.02	-0.16	1.38	2.73	1.91	4.08
AE DKH PBE+U	1.0	2.02	0.02	-0.17	1.38	2.74	1.91	4.08
AE DKH PBE+U	2.0	2.02	0.02	-0.17	1.38	2.76	1.91	4.08

As expected, the atomic charges and the valence orbital populations indicate the role of various orbitals in chemical bonding. The individual contribution of various atomic orbitals to molecular orbitals of UO_2^{2+} are tabulated in Table 6.3. This information is graphically illustrated in Figure 6.1 where the valence MOs of UO_2^{2+} from the PBE eigenvectors are shown along with cartoon representation of these orbitals. At the bottom of the MO diagram (Figure 6.1) one can see that the U 6p orbital which lies along the uranyl axis interacts with the σ^* 2s orbital fragment of the oxo ligands resulting in the bonding σ (7 a_{2u}, -44.6 eV) and antibonding σ^* (8 a_{2u}, -30.7 eV) orbitals. As this is a pair of bonding/antibonding MOs, the net contribution to the metal-ligand bonding is small, if not negligible. The uranium 6p orbitals which are oriented perpendicular to the uranyl axis stay non-bonding at -39 eV (6 e_{1u}). The σ 2s orbital (11 a_{1g}, -37.4 eV) fragment of the oxo ligands is very mildly stabilized by a U 6d orbital; 6d contribution is not shown in cartoon representation.

For the present discussion, the most interesting occupied MOs lie in the narrow range from -22.1 eV to -23.4 eV (Figure 6.1, Table 6.3). These orbitals represent the σ and π orbitals formed by uranium 6d and 5f orbitals with the oxo 2p orbitals. The lowest of these orbitals is the π^* $2p_x$ and $2p_y$ orbital fragments (degenerate) of the oxo ligand both which are stabilized (π-donation) through π interactions with the uranium $6d_{xz}$ and $6d_{yz}$ orbitals, respectively (4 e_{1g}, -23.4 eV). The corresponding π components of the $2p_x$ and $2p_y$ orbital fragments are stabilized (π-donation) by uranium $5f_{xz^2}$ and $5f_{yz^2}$ orbitals, respectively (7 e_{1u}, -23.1 eV). The σ $2p_z$ orbital fragment of the oxo ligands interacts through σ-donation with the U $6d_{z^2}$ orbital (12 a_{1g}, -22.7 eV). Finally, the σ^* $2p_z$ orbital fragment of the oxo ligand interacts through σ-donation with the U $5f_{z^3}$ which forms the HOMO of UO_2^{2+} (9 a_{2u}, -22.1 eV). Two pairs of unoccupied non-bonding type 5f orbitals at -19.8 eV and -19.1 eV are the ϕ (2 e_{3u}) and δ (2 e_{2u}) type U 5f orbitals respectively. The anti-bonding partners to the bonding MOs with 5f and 6d contributions lie above these 5f ϕ and δ type orbitals. A pair of unoccupied non-bonding 6d orbitals of d_{xy} and $d_{x^2-y^2}$ character

lies far above the unoccupied 5f levels; these orbitals are not shown in Figure 6.1. The overall orbital interactions involved in the U-O bonding is illustrated in Figure 6.2. In the axial ligand field of the oxo ligands, the U 5f and 6d orbitals are split to form quasi-atomic 5f and 6d orbitals (Figure 6.2) which involve in bonding with the completely filled 2p orbitals of the oxo ligands (Figure 6.2). The 5f MOs both and unoccupied, lie between the 6d occupied and unoccupied MOs indicating a stronger U 6d - O 2p bonding interaction and a relatively weaker U 5f - O 2f bonding interaction.

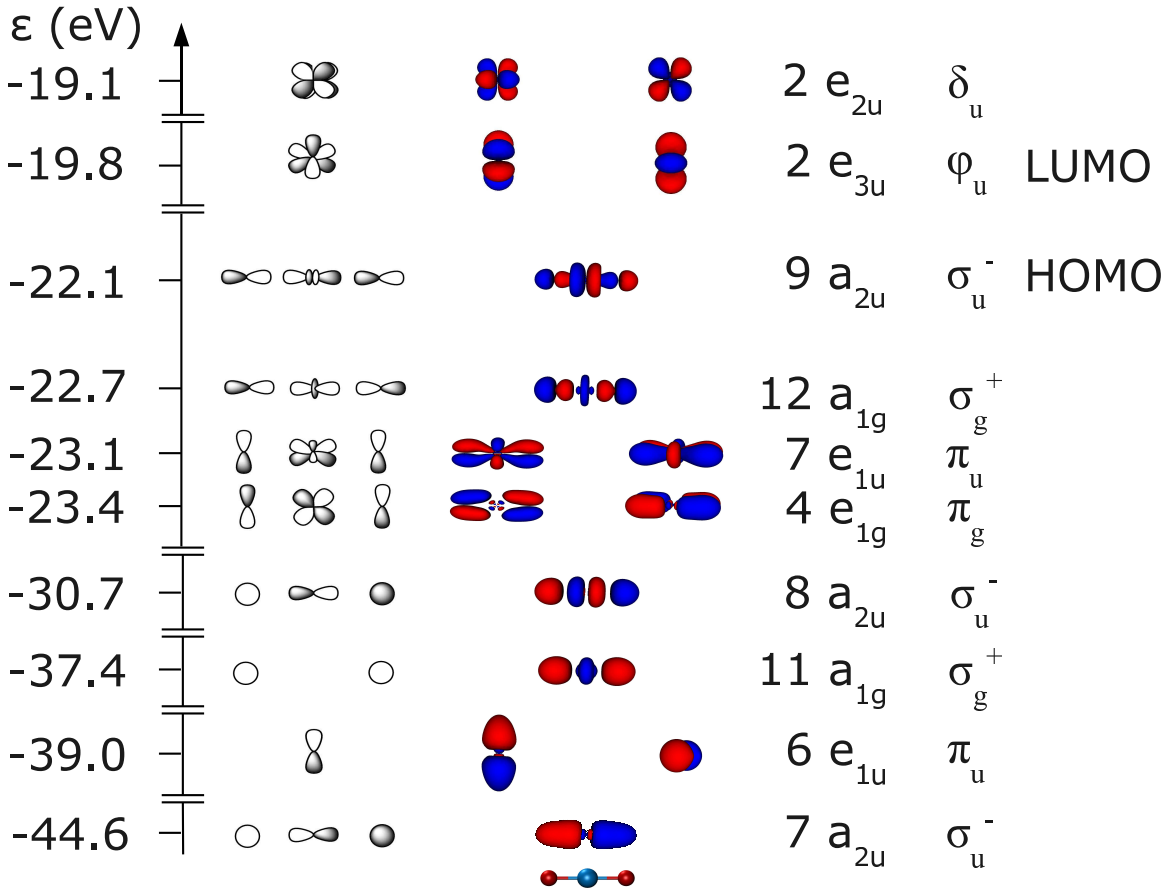

Figure 6.1: Valence MOs of UO_2^{2+} at the AE DKH PBE equilibrium geometry along with their energies ε in eV (left) and symmetry labels (right) according to D_{8h} and $D_{\infty h}$ point group symmetries. The linear structure of the UO_2^{2+} molecule (bottom) and cartoon representation of MOs (left) are shown for reference.

When comparing the orbital energies in PBE and PBE + U calculations (Table 6.3) one notes that the non-bonding unoccupied orbitals of the type ϕ (2 e_{3u}) and δ (2 e_{2u}) are shifted higher by about 1 eV with the inclusion of the Hubbard term with U_{eff} = 2.0 eV. The contribution of the U 5f_{z^3} orbital to the HOMO (9 a_{2u}) is more than 50%. Thus the energy correction provided by the Hubbard term is negative and the HOMO is stabilized by about 0.3 eV for U_{eff} = 2.0 eV. An interesting situation arises for the 7 e_{1u} orbital where the π-type 5f orbitals contribute by about

40% but in the PBE + U calculation no positive correction is obtained. This is due to the fact that the definition of orbital occupation matrix employed in the PBE + U calculation is $\mathbf{S}\cdot\mathbf{D}\cdot\mathbf{S}$ which leads to occupation numbers slightly larger than given by the Mulliken population matrix which is formally expressed as $\mathbf{D}\cdot\mathbf{S}$. Thus for the π-type $5f$ orbitals $\mathbf{S}\cdot\mathbf{D}\cdot\mathbf{S}$ leads to occupation number of about 0.5 e resulting in zero or very small corrections to the corresponding potential matrix elements. All other MOs where the contribution of U $5f$ is negligible are essentially not affected by the Hubbard term with U_{eff} = 2.0 eV included for the U $5f$ shell (Table 6.3).

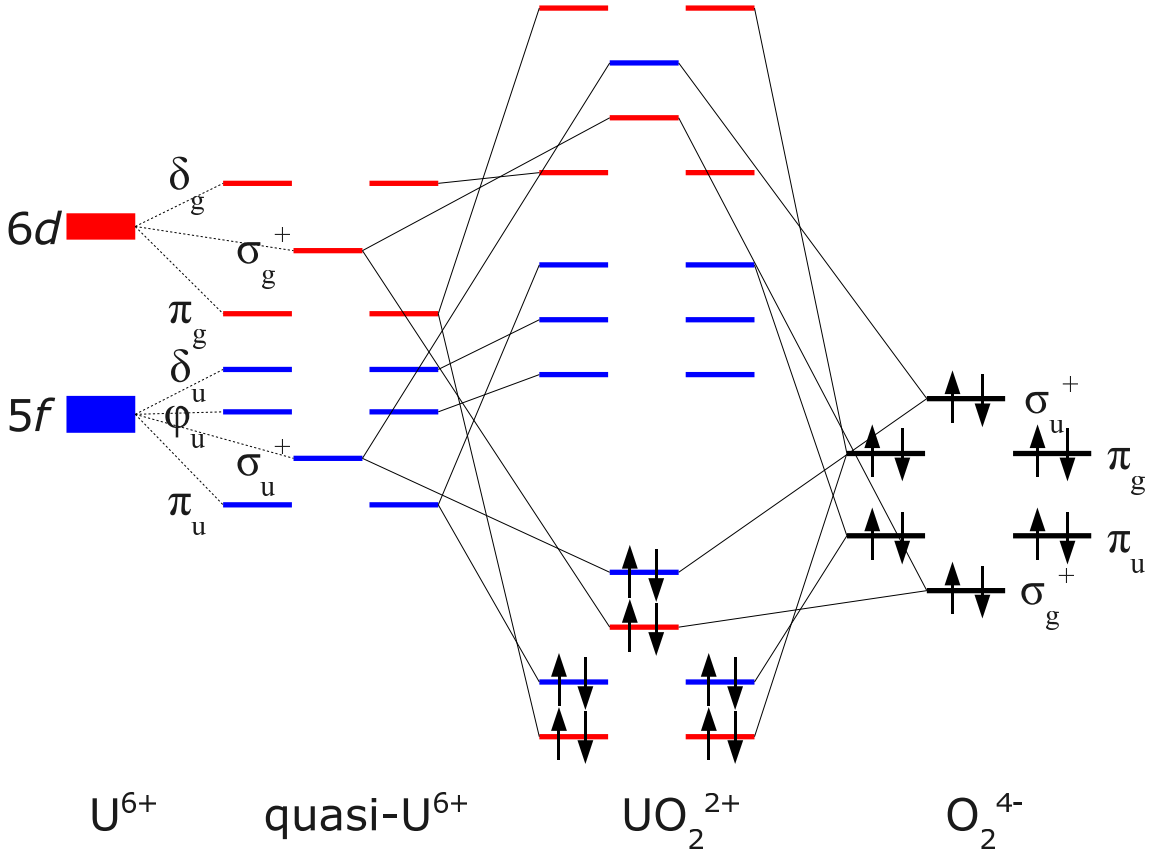

Figure 6.2: Qualitative illustration of the orbital interaction involving the U $5f$ and $6d$ shells and the $2p$ fragment orbitals of the oxo ligands. Orbitals with $5f$ contribution are shown in blue and orbitals with $6d$ contribution are shown in red. The symmetry classification is according to $D_{\infty h}$ point group symmetry where the symmetry of the MOs are the same as that of component AOs.

Second-order Jahn–Teller type interaction in UO_2^{2+}

Before proceeding to the main discussion, a brief overview of Jahn–Teller distortion is given in the following. According to Jahn–Teller theorem [165], degenerate electronic states in symmetric non-linear molecules are unstable with respect to a geometrical distortion that lifts the degeneracy hence resulting in a non-symmetric structure. Using perturbation theory, Jahn and

Table 6.3: Mulliken population analysis (in %) of the valence MOs of UO_2^{2+} [a] along with orbital energies ε_i (eV).

Method	MO	ε_i	U				O	
			7*s*	6*p*	6*d*	5*f*	2*s*	2*p*
AE DKH PBE	$2e_{2u}$	-19.05				100		
	$3e_{3u}$	-19.78				100		
	$9a_{2u}$	-22.07		9		57	6	33
	$12a_{1g}$	-22.73	3		15		7	76
	$7e_{1u}$	-23.13		2		37		62
	$4e_{1g}$	-23.37			24			76
	$8a_{2u}$	-30.71		30		5	55	10
	$11a_{1g}$	-37.45	2		8		88	2
	$6e_{1u}$	-38.96		99				1
	$7a_{2u}$	-44.63		52		1	38	9
AE DKH PBE + U [b]	$2e_{2u}$	-18.02				100		
	$3e_{3u}$	-18.75				100		
	$9a_{2u}$	-22.39		9		58	1	32
	$12a_{1g}$	-22.77	3		15		7	76
	$7e_{1u}$	-23.18		2		36		62
	$4e_{1g}$	-23.43			24			76
	$8a_{2u}$	-30.74		31		6	54	10
	$11a_{1g}$	-37.49	2		8		88	2
	$6e_{1u}$	-38.92		99				1
	$7a_{2u}$	-44.75		51		1	39	9

[a] Calculations carried out with symmetry constraints according to point group D_{8h}.
[b] U_{eff} = 2.0 eV for the 5*f* shell of U.

Teller showed [165] that the change in energy associated with the distortion is a term that is linearly dependent (first-order term) on the distortion coordinate. Further, using symmetry considerations, they showed that for the first-order term to be non-zero, the symmetry species of the distortion coordinate (or distortion mode) must be contained within the symmetric direct product of the symmetry species of the electronic ground state. Thus such distortion associated with orbitally degenerate electronic states of non-linear molecules is known as the first order Jahn–Teller (FOJT) distortion and the related concepts are collectively known as FOJT theorem. The FOJT theorem is invoked to explain the distorted geometry of molecules such as H_3^-, coordination complexes of the type MX_6 (where M = Cu(II), Ni(II) and X is a monodentate ligand such as hydroxyl) [139, 140].

The second-order Jahn–Teller (SOJT) [166] effect refers to the commonly observed trend that

a molecule with small energy gap between the occupied and unoccupied MOs is susceptible to a geometrical distortion with enables mixing between these MOs. Using the perturbation theory arguments of Jahn and Teller, the net stabilization energy associated with such a distortion can be shown to be second-order term, which is inversely proportional to the energy gap of the quasi-degenerate MOs involved [139]. Often the MOs that are involved in the SOJT effect are the HOMO and the LUMO of the molecule. The SOJT effect can be invoked to explain the bent structure of H_2O, pyramidal structure of NH_3 and so on. Davidson and Borden [167] pointed out that in practical computations, SOJT-like distortions can also result due to the inaccuracy of an approximate wavefunction leading to an artifactual SOJT distortion.

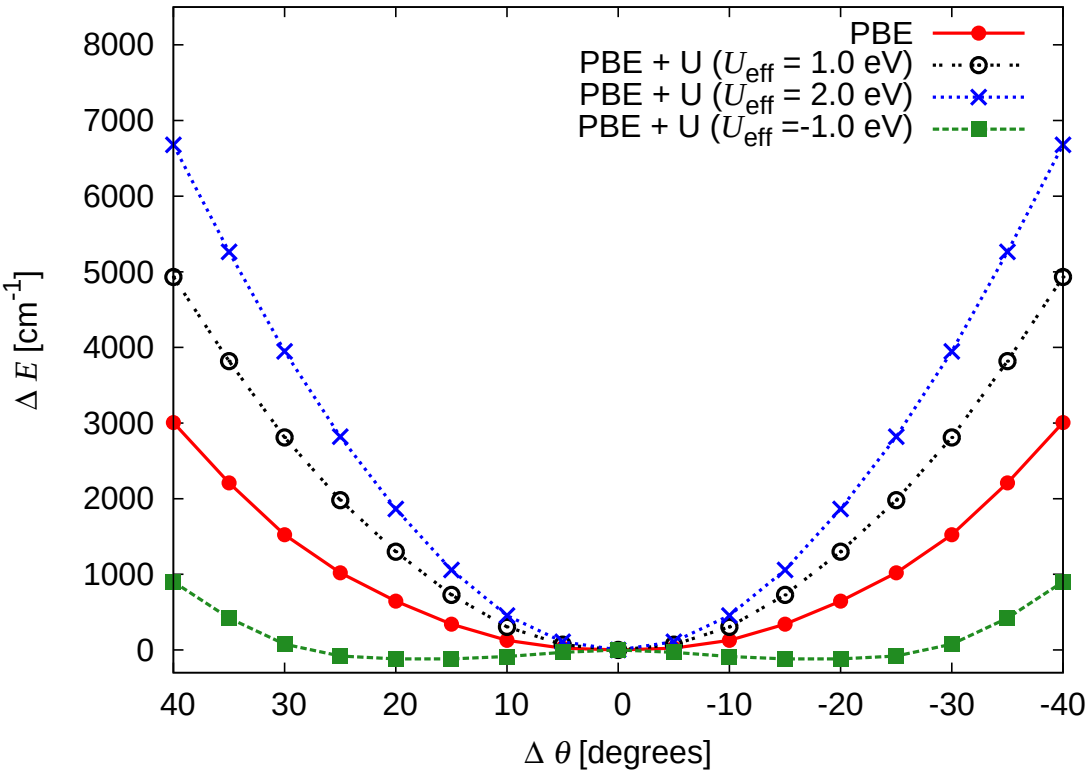

Figure 6.3: AE DKH PBE and AE DKH PBE + U potential energy profiles of UO_2^{2+} along the bending mode. In the PBE + U calculations, U_{eff} values of 1.0, 2.0 and -1.0 eV were employed. Relative energy ΔE in cm^{-1} with respect to the energy of the linear structure are plotted for various angles of deviation from linearity $\Delta\theta$ in degrees. The curve was obtained by optimizing the U-O bond length for selected values of the uranyl bond angle θ by enforcing C_{2v} point group symmetry restrictions.

The main aspects of the ground state electronic structure and geometry features of UO_2^{2+} have been discussed so far. The main objective of the subsequent discussion is to explore the reason for the low vibrational frequency of the bending mode of UO_2^{2+} as predicted by the GGA method PBE and to illustrate the sources of improvements provided by the DFT + U correc-

tion term. In the following it will shown that a weak SOJT type interaction which fractionally populates the non-bonding type U $5f$ orbitals is enhanced in the PBE calculation. KS DFT calculations overstabilize systems with fractional occupation numbers which in this case leads to an underestimation of the uranyl bending frequency.

The potential energy of UO_2^{2+} along the uranyl bond angle is shown in Figure 6.3 both at the PBE and the PBE + U levels. The PBE energy profile is flat (red line connecting solid circles) and at the PBE + U level, for U_{eff} = 1.0 eV, bent structures are less favored which results in a steeper potential (black line connecting hallow circles) representing a more rigid uranyl structure with an increased bending frequency (167 cm^{-1}, Table 6.1). With further increase, U_{eff} = 2.0 eV, bent structures are increasingly less favored, i.e. uranyl is more rigid with a larger bending frequency (211 cm^{-1}, Table 6.1). In Table 6.4, natural orbital occupation numbers of the $5f$ orbitals are given for the uranyl species with bond angles 180°, 160° and 140° from PBE calculations as used in Figure 6.3. The corresponding DFT + U corrections for the total energy and diagonal potential matrix elements are also given in Table 6.4. The estimated DFT + U energy corrections E^U for the structures with $\theta = 180°$, 160° and 140° are 0.69, 0.76 and 0.96 eV, respectively, and these values are closer to the results from DFT + U constrained optimizations with U_{eff} = 1 eV which are 0.68, 0.76 and 0.91 eV respectively [2]. One notes that for the bent structures, the positive energy corrections E^U from the DFT + U correction term is larger than that for the linear structure. For the uranyl bond angle 160° the DFT + U energy correction E^U is larger than the energy correction obtained for the linear structure by 0.07 eV. With a larger deviation from linearity, as in the case of uranyl bond angle 140°, the DFT + U energy correction is even larger. The corresponding DFT + U corrections to the potential elements v_i^U to the DFT eigenvalues are also given in Table 6.4, and these contribute to the corresponding MOs of same symmetry types based on the contributions from these quasi AOs. In the three PBE calculations with uranyl bond angles $\theta = 180°$, 160° and 140°, the total $5f$ occupation (sum of n_i, Table 6.4) is the same according to $\mathbf{D}\cdot\mathbf{S}$ and $\mathbf{S}\cdot\mathbf{D}\cdot\mathbf{S}$ matrices, but for larger deviations from linearity, due to intra-atomic $5f$ - $5f$ hybridization, these occupation numbers involve various f orbitals to different extents.

As a numerical experiment, the uranyl bending mode energy profile was probed with a negative value for the Hubbard parameter (U_{eff} = -1.0 eV), Figure 6.3. A negative U_{eff} will enhance the shortcomings of a pure KS-DFT calculation and in this case results in predicting a bent uranyl as the minimum energy structure. The bending mode potential of UO_2^{2+} at the PBE + U level with U_{eff} = -1.0 eV shows a *pseudo barrier* at the linear configuration (green line connecting solid squares) and represents a double-well potential with a barrier height of 121 cm^{-1}. From a

[2] When performing DFT calculations it turned out to be useful in some cases to set a small U_{eff} value, e.g. $<10^{-8}$ eV, to print the orbital occupation numbers which can be used to estimate the DFT + U corrections.

Table 6.4: Occupation numbers of U $5f$ atomic orbitals at various uranyl bending angles in AE DKH PBE calculations along with calculated DFT + U corrections: Uranyl bond angles (in degree), Symmetry classification of f orbitals according to $D_{\infty h}$, D_{8h} and C_{2v} point groups, natural orbital occupation numbers n_i in e are given according to the Mulliken population matrix **D**·**S** and the full occupation matrix **S**·**D**·**S**, DFT + U corrections E^U to the total energy and diagonal elements v_i^U of the potential matrix (in eV) are given for the Hubbard parameter U_{eff} = 1.0 eV.

θ	AO	Symmetry [a]			n_i		E^U	v_i^U
		$D_{\infty h}$	D_{8h}	C_{2v}	**D**·**S**	**S**·**D**·**S**		
180	f_z^3	σ_u^+	a_{2u}	b_2	1.21	1.50	0.19	-0.25
	f_{xz^2}	π_u	e_{1u}	a_1	0.76	1.03	0.25	-0.02
	f_{yz^2}			b_1	0.76	1.03	0.25	-0.02
	f_{xyz}	δ_u	e_{2u}	a_2	0.00	0.00	0.00	0.50
	$f_{z(x^2-y^2)}$			b_2	0.00	0.00	0.00	0.50
	$f_{x(x^2-3y^2)}$	ϕ_u	e_{3u}	a_1	0.00	0.00	0.00	0.50
	$f_{y(3x^2-y^2)}$			b_1	0.00	0.00	0.00	0.50
	f_{total}				2.72	3.58	0.69	
160	f_z^3	σ_u^+	a_{2u}	b_2	1.17	1.45	0.20	-0.23
	f_{xz^2}	π_u	e_{1u}	a_1	0.73	0.99	0.25	0.05
	f_{yz^2}			b_1	0.71	0.97	0.25	0.02
	f_{xyz}	δ_u	e_{2u}	a_2	0.06	0.09	0.04	0.46
	$f_{z(x^2-y^2)}$			b_2	0.06	0.10	0.05	0.45
	$f_{x(x^2-3y^2)}$	ϕ_u	e_{3u}	a_1	0.00	0.00	0.00	0.50
	$f_{y(3x^2-y^2)}$			b_1	0.00	0.00	0.00	0.50
	f_{total}				2.73	3.58	0.76	
140	f_z^3	σ_u^+	a_{2u}	b_2	1.06	1.30	0.23	-0.15
	f_{xz^2}	π_u	e_{1u}	a_1	0.68	0.90	0.25	0.05
	f_{yz^2}			b_1	0.60	0.82	0.24	0.09
	f_{xyz}	δ_u	e_{2u}	a_2	0.18	0.28	0.12	0.36
	$f_{z(x^2-y^2)}$			b_2	0.18	0.28	0.12	0.36
	$f_{x(x^2-3y^2)}$	ϕ_u	e_{3u}	a_1	0.01	0.00	0.00	0.50
	$f_{y(3x^2-y^2)}$			b_1	0.00	0.00	0.00	0.50
	f_{total}				2.70	3.56	0.96	

[a] The C_n axis (in D_{nh}) coincides with the z-axis which passes through the O and U atoms. The C_2 axis (in C_{2v}) coincides with the x-axis and is perpendicular to the O-U-O axis; in bent structures the molecule lies in the *xz* plane.

fully relaxed geometry optimization of UO_2^{2+} at the PBE + U level with the U_{eff} value -1.0 eV, the equilibrium bond angle was found to be 162.4 °. A similar trend was noted for U_{eff} = -0.5 eV where the potential is still a double well but is shallow; the equilibrium bond angle was found to be 175.6 °.

As discussed before, from Table 6.3 one sees the effect of the Hubbard term on the MOs. For U_{eff} = 2.0 eV, the unoccupied MOs which represent the ϕ and δ type non-bonding U $5f$ orbitals were shifted up by 1.0 eV (half the value of U_{eff} for zero occupation numbers) and the HOMO (9 a_{2u}) was stabilized by about 0.3 eV. From this one can estimate the corrections introduced by the negative Hubbard parameter U_{eff} = -1.0 eV. In this case the HOMO will be destabilized by about 2 eV and the unoccupied ϕ and δ type U $5f$ orbitals will be shifted down by about 0.5 eV thus decreasing the HOMO-LUMO gap [3]. A decrease in the HOMO-LUMO gap means that intra-atomic $5f$-$5f$ hybridization is more feasible. Furthermore, the uranyl HOMO represents the U $5f$ - O $2p$ σ bond which is destabilized in the case U_{eff} = -1.0 eV resulting in an elongation of the U-O bond by 0.4 pm compared to the PBE value 171.9 pm. A possible explanation of uranyl bending for a negative U_{eff} can be provided at this point. The destabilization of bonding MOs representing uranyl U $5f$ - O $2p$ σ and π bonds resulting in increased U-O bond length which overall weakens the ligand binding. This is partly compensated if the ligands move away from linearity to interact with the δ-type $5f$ orbitals which overlap better with O $2p$ orbitals in a bent configuration.

6.1.2 Conclusions

The uranyl dication UO_2^{2+} is a stable linear species. The participation of both $5f$ and $6d$ orbitals in the uranyl bonds is responsible for the stability and the linearity of the uranyl framework [156, 158]. The rigidity of this framework is also supported by the fact that the ligands in coordination complexes of uranyl are predominantly confined to the equatorial plane perpendicular to the linear uranyl moiety [169]. The hybrid-DFT approach B3LYP and wave-function based methods describe the bare uranyl cation with sufficient accuracy [155] whereas in GGA calculations the vibrational frequency of the bending mode of UO_2^{2+} is underestimated, by 70–80 cm^{-1}, which is about 40% of the value obtained with more accurate methods.

The low force constant of the uranyl bending mode in the PBE-GGA KS calculation is a consequence of the inaccurate description of the Coulomb interaction of the U $5f$ electrons. From the uranyl bending mode profiles calculated at PBE and PBE + U levels (Figure 6.3), one can note that at the PBE level, the uranyl molecule with a non-linear geometry is overstabilized.

[3] For U_{eff} = -1.0 eV, r(UO) = 172.3 pm, θ = 162.4 pm, ε_{HOMO} = -21.80 eV, ε_{LUMO} = -20.17 eV, $\Delta\varepsilon$ = 1.63 eV, see Table 6.1 for the corresponding PBE values.

In a PBE + U calculation with U_{eff} = -1.0 eV, such an overstabilization is further enhanced resulting in a uranyl equilibrium bond angle of about 162°. This situation is understood through the fractional occupation of the non-bonding δ-type quasi $5f$ orbitals of U which arises due to a second-order Jahn–Teller type interaction between the uranyl σ occupied MO (HOMO of uranyl) and the δ-type $5f$ orbitals when uranyl deviates from linearity. The nature of self-interaction error present in LDA and GGA KS calculations is such that Coulomb repulsion is underestimated for fractional electrons resulting in spurious stabilization of systems with fractionally occupied orbitals.

6.2 Penta Aqua Uranyl

The present section deals with the application of the DFT + U methodology to the uranyl penta-aqua complex $[UO_2(H_2O)_5]^{2+}$, the most frequent form in which the uranyl dication occurs in an aqueous medium. In the uranyl penta-aqua complex, the uranyl ion is coordinated by five water molecules in the equatorial plane which is oriented perpendicular to the axis of the linear uranyl moiety. B3LYP and wave function based calculations of the penta-aqua complex $[UO_2(H_2O)_5]^{2+}$ indeed suggest a linear uranyl moiety with all oxygen atoms of the ligands in the equatorial plane [170]. In contrast, LDA and GGA KS calculations yield a (slightly) bent uranyl moiety with the ligands coordinated out of the equatorial plane [171–173]. In this thesis, by applying the DFT + U methodology, the bent geometry of the uranyl moiety in the penta-aqua complex as obtained in LDA and GGA KS calculations, will be identified as a self-interaction artifact related to the Coulomb interaction of the U $5f$ electrons.

6.2.1 Results and Discussions

Structural properties of $[UO_2(H_2O)_5]^{2+}$ with D_{5h} symmetry restrictions

The effect of the equatorial ligand environment on the structural aspects of uranyl such as bond lengths and stretching frequencies can be understood by studying the complex $[UO_2(H_2O)_5]^{2+}$ with symmetry restrictions according to the point group D_{5h}, Table 6.5. At the PBE level, the uranyl bonds of the bare uranyl ion are 171.9 pm (Table 6.1); in the penta-aqua complex, these bonds are elongated by 5.3 pm (Table 6.5). This indicates a weakening of the uranyl bonds in the presence of equatorial water ligands, as expected according to the principle of bond order conservation. PBE and PBE + U calculations yield U-O_t bond lengths of the hydrated complex in the range 177.2–176.3 pm (Table 6.5). With U_{eff} = 2.0 eV, the U-O_t bonds are 0.9 pm shorter than the corresponding PBE distances. Notably, the PBE + U value (U_{eff} = 2.0 eV) for the length

of the U-O_t bond in hydrated uranyl, 176.3 pm, is close to the B3LYP value, 175.6 pm [171], and the experimental value in aqueous solution, 176 pm [174]. That good agreement may in part be fortuitous as long-range solvation effects are not included in this model where only the first ligand shell of uranyl in a aqueous medium is accounted for. These long-range effects may be estimated from the LDA values [173], (Table 6.5) without and with long-range solvent effects included via a continuum model; accordingly, these solvent effects tend to increase slightly the covalent U-O_t bond length, by 1 pm, from the LDA value 177 pm.

Table 6.5: Bond distances [a] (pm) and vibrational frequencies [a] (cm^{-1}) of the uranyl penta-aqua complex $[UO_2(H_2O)_5]^{2+}$ in the gas phase from calculations applying various computational methods and symmetry constraints. Also given is the Hubbard parameter U_{eff} (eV) for the U $5f$ shell as well as available experimental data.

Method	Symmetry	U_{eff}	U-O_t	U-O_w	ω_s	ω_a	ω_b
AE DKH PBE	D_{5h}		177.2	248.9	893	985	190
AE DKH PBE + U	D_{5h}	1.0	176.7	250.0	898	995	216
AE DKH PBE + U	D_{5h}	2.0	176.3	251.1	905	1004	234
AE DKH VWN	C_s [b]		177	241			
AE DKH VWN	C_s [b, c]		178	236			
AE DKH BP	D_{5h} [d]		177.5	248.8	886	979	190
RECP/B3LYP	C_1 [e]		175.6	251.6	908	1001	213,222
Exp.			176 [f]	241 [f]	874 [g]	963 [g]	253 [g]

[a] U-O_t–bond to terminal oxygen centers of uranyl, U-O_w–average bond length to oxygen centers in the equatorial plane of uranyl, ω_s–frequency of the symmetric stretching vibration of uranyl, ω_a–frequency of the asymmetric stretching vibration of uranyl, ω_b–frequency of the O_t-U-O_t bending vibration of uranyl.
[b] Ref. [173].
[c] Long-range electrostatic solvent effects were accounted for with the COSMO method, a polarizable continuum approach [175].
[d] Ref. [164].
[e] Ref. [171].
[f] Extended X-ray absorption fine structure (EXAFS) result for UO_2^{2+} in aqueous chloride solution, Ref. [174].
[g] IR and Raman bands of uranyl perchlorate in aqueous solution, Ref. [176].

Experiment suggests a value of 241 pm for the distance U-O_w between the uranium center and the oxygen centers of the equatorial aqua ligands [174]. A PBE calculation on the penta-aqua uranyl dication yields the value of 248.9 pm, which is very close to the results of an earlier BP calculation, 248.8 pm [164] (Table 6.5). The PBE + U value (U_{eff} = 2 eV), 251.1 pm is closer to the B3LYP result, 251.6 pm [171]. The average U-O_w distance is more sensitive to

long-range solvent effects as can be seen from the LDA value of 241 pm which decreases by 5 pm when a polarizable continuum model is invoked (Table 6.5) [173]. From this result one estimates the corresponding PBE + U value (U_{eff} = 2 eV) in a model of long-range electrostatic effects at 246 pm, still overestimating the experimental result of 241 pm (Table 6.5) [174]. For the intermediate value of the Hubbard parameter, U_{eff} = 1.0 eV, both the bond lengths U-O_t and U-O_w take intermediate values. Overall, it is interesting to note that the PBE + U parameters of the equilibrium geometry are approaching the B3LYP results; the same trend was previously noted for the bare uranyl species, discussed above.

As in the case of the bare uranyl system (Table 6.1), the uranyl vibrational frequencies of the penta-aqua complex are blue-shifted at the DFT + U level compared to the PBE results. The corrections are notable only for the larger value U_{eff} = 2.0 eV, 12 cm^{-1} for the symmetric and 19 cm^{-1} for the asymmetric mode. In contrast, the vibrational frequency of the bending mode is blue-shifted by 44 cm^{-1} (Table 6.5) at the DFT + U level.

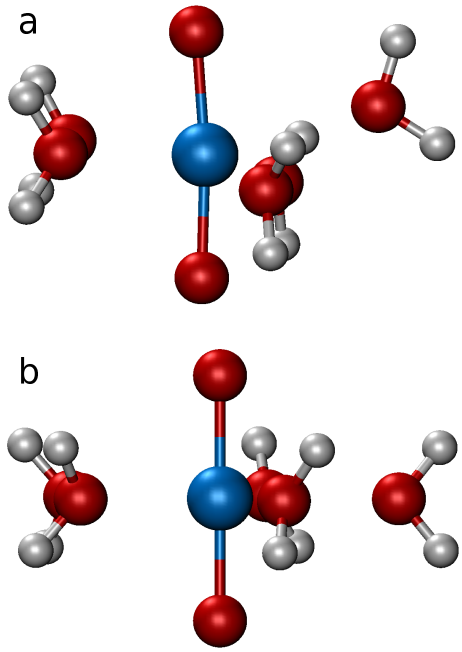

Figure 6.4: Equilibrium geometries of the complex $[UO_2(H_2O)_5]^{2+}$ optimized without symmetry constraints: (a) PBE, (b) PBE + U (U_{eff} = 2.0 eV).

Geometry distortion of the ligand shell in the penta-aqua uranyl complex

The D_{5h} structure of the penta-aqua uranyl complex has been rationalized to be unstable because of the repulsion of the lone-pairs of the water ligands in the equatorial plane [170]. At the B3LYP level, a more stable D_5 structure is reached by tilting the molecular planes of the water ligands by about 20° with respect to the uranyl axis [170]. However in LDA or GGA calculations, the

molecular planes of the water molecules are not tilted; rather, they still lie in the planes parallel to the uranyl framework as in the D_{5h} structure [170, 173]. Instead, some water ligands are asymmetrically shifted up or down with respect to the equatorial plane (Figure 6.4).

Table 6.6: Bond distances [a] (pm) and bond angle [a] (degree) of the uranyl penta-aqua complex in the gas phase from calculations applying various computational methods *without* symmetry constraints. Also given is the Hubbard parameter U_{eff} (eV) for the U $5f$ shell.

Method	U_{eff}	$\langle$U-O$_t\rangle$	$\langle$U-O$_w\rangle$	Δ(U-O$_w$)	O$_t$-U-O$_t$
AE DKH PBE		177.4	248.1	1.20	174.6
AE DKH PBE + U	1.0	176.8	249.5	0.80	177.5
AE DKH PBE + U	1.5	176.6	250.2	0.50	178.5
AE DKH PBE + U	2.0	176.2	251.3	0.06	180.0
AE DKH VWN		176.6	240.4	1.48	171.4
AE DKH BP		177.8	248.3	1.20	172.6
AE DKH PBEN		177.7	251.8	1.62	173.0
RECP/B3LYP [b]		174.8	250.0	0.00	180.0
Exp. [c]		176	241		

[a] $\langle$U-O$_t\rangle$–bond to terminal oxygen centers of uranyl, $\langle$U-O$_w\rangle$–average bond length to oxygen centers in the equatorial plane of uranyl, Δ(U-O$_w$)–absolute average of deviations of the bond lengths to oxygen centers in the equatorial plane from the average value, O$_t$-U-O$_t$ bond angle of uranyl.
[b] Ref. [170].
[c] EXAFS result (Table 6.5); Ref. [174].

Table 6.6 summarizes geometry parameters of the penta-aqua complex of uranyl from B3LYP [170, 171], as well as LDA-VWN, GGA-BP, GGA-PBE, GGA-PBEN, and GGA-PBE + U calculations [26]. The PBE equilibrium geometry of the penta-aqua uranyl dication is a distorted C_1 structure (Figure 6.4) with a bent uranyl moiety, O$_t$-U-O$_t$ = 174.6°, and the oxygen centers of the equatorial aqua ligands are shifted out of the equatorial plane. With increasing onsite-Coulomb parameter U_{eff}, the uranyl moiety tends towards linearity: O$_t$-U-O$_t$ = 177.5°, 178.5°, and 180.0° for U_{eff} = 1.0 eV, 1.5 eV, and 2.0 eV, respectively (Table 6.6). The overall PBE + U structure for U_{eff} = 2.0 eV approximately fulfills D_5 symmetry where the average value of the O$_t$-U-O$_w$-H dihedral angle is 20.7° (Figure 6.4), which is very similar to the B3LYP structure [170], where on average O$_t$-U-O$_w$-H = 20.0°. As with increasing U_{eff} the overall structure of the complex tends towards D_5 symmetry, but bond lengths are only moderately affected. With U_{eff} = 2.0 eV, the average U-O$_t$ bond length is shortened by 1.2 pm and the average U-O$_w$ distance is elongated by 3.2 pm, compared to a simple PBE calculation.

Gutowski and Dixon also reported a distorted C_1 equilibrium structure with the LDA-SVWN functional [170]. They related this distortion to both the repulsion between neighboring oxygen centers of equatorial water ligands (rationalized in turn by the short U-O_w bond lengths in the SVWN model) and the low frequency of the bending mode of isolated uranyl (about 150 cm^{-1}). Other widely used purely local or gradient-corrected xc functionals, e.g. VWN, BP, and PBEN, also predict a distorted C_1 structure with significantly different U-O_w distances. Note, for example, the difference of more than 7 pm between the VWN and PBE results (Table 6.6). However, the strong correlation of the U_{eff} values with the symmetry of the complex (and the relatively weak correlation with changes of bond lengths) suggest that the repulsion between neighboring oxygen atoms due to inaccurate U-O_w bond lengths in purely local or gradient-corrected KS calculations may be responsible only in part for the distorted structure of the ligand shell and the bent uranyl moiety. This suggestion is corroborated by the GGA U-O_w distances which are rather similar to the B3LYP results (Table 6.6).

Table 6.7: Relative energies [a] (kJ/mol), HOMO–LUMO gap [a] (eV), orbital energies [a] (eV), and populations of HOMO (percentage) of the uranyl penta-aqua complex in the gas phase from calculations applying various computational methods and symmetry constraints. Also given is the Hubbard parameter U_{eff} (eV) for the U $5f$ shell.

Symmetry	Method	U_{eff}	ΔE	$\Delta\varepsilon$	$\varepsilon_{\text{HOMO}}$	U f	O_t p	O_w p
D_{5h}	AE DKH PBE		3.4	2.86	-15.75		1	99
	AE DKH PBE + U	1.0	1.4	2.99	-15.71		1	99
	AE DKH PBE + U	2.0	1.6	3.14	-15.66		1	99
	RECP/B3LYP [b]		1.3					
D_5	AE DKH PBE		2.6	2.84	-15.76	12	9	76
	AE DKH PBE + U	1.0	0.3	3.03	-15.77	5	4	88
	AE DKH PBE + U	2.0	0.1	3.23	-15.76	3	2	93
	AE DKH SVWN [b]		3.3					
	RECP/B3LYP [b]		0.0					
C_1	AE DKH PBE			3.09	-15.94	1	0	98
	AE DKH PBE + U	1.0		3.11	-15.82	0	0	98
	AE DKH PBE + U	2.0		3.23	-15.76	3	2	93

[a] ΔE – relative electronic energy with respect to the C_1 configuration, $\Delta\varepsilon$ – difference between the energies of HOMO and LUMO, $\varepsilon_{\text{HOMO}}$ – energy of the HOMO.
[b] Ref. [170].

To quantify the preference for the nonsymmetric (C_1) structure over the D_5 structure, geometry optimizations were carried out for the penta-aqua complex with symmetry constraints

according to the point groups D_5 and D_{5h}. Table 6.7 presents the relative energies of D_{5h}, D_5, and C_1 configurations from PBE and PBE + U calculations and compares them with results from VWN and B3LYP calculations. At the PBE level, the C_1 structure is more stable by 2.6 kJ/mol than the D_5 structure, the latter turning out to be a transition state of second order. This finding is similar to the preference for C_1 at the LDA-SVWN level [170], 3.3 kJ/mol. In PBE + U (U_{eff} = 1.0 eV) calculations this margin decreases to 0.3 kJ/mol and with U_{eff} = 2.0 eV both the C_1 and D_5 structures have nearly identical energies, as calculated with the B3LYP approach.

Table 6.8: Lowest three harmonic frequencies of $[UO_2(H_2O)_5]^{2+}$ (by absolute value) from AE DKH PBE + U calculations on models in the gas phase, applying various symmetry constraints. Also given is the Hubbard parameter U_{eff} (eV) for the U $5f$ shell.

Symmetry	Method	U_{eff}	Modes		
			ω_{46}	ω_{47}	ω_{48}
D_{5h}	AE DKH PBE		43.2 i	44.6 i	124.3 i
	AE DKH PBE + U	1.0	33.9 i	36.0 i	135.5 i
	AE DKH PBE + U	2.0	43.2 i	43.2 i	146.4 i
D_5	AE DKH PBE		60.2	21.9 i	22.4 i
	AE DKH PBE + U	1.0	63.0	20.5	19.6
	AE DKH PBE + U	2.0	58.7	33.6	33.1
C_1	AE DKH PBE		105.3	52.0	10.7
	AE DKH PBE + U	1.0	78.1	46.5	11.0
	AE DKH PBE + U	2.0	56.6	32.0	31.4

In order to characterize the D_{5h}, D_5 and C_1 structures of $[UO_2(H_2O)_5]^{2+}$ as maximum or minimum energy configurations, harmonic frequency calculations were performed for the D_{5h}, D_5 and C_1 equilibrium geometries at the PBE and PBE + U levels. The values of the lowest three harmonic frequencies of $[UO_2(H_2O)_5]^{2+}$ (i.e. ω_{46}, ω_{47}, ω_{48}) at PBE and PBE + U levels are presented in Table 6.8. Structures optimized with D_{5h} constraints at the PBE level for all U_{eff} values exhibit three imaginary frequencies as in the case of a B3LYP calculation [170,171]. Both at the PBE and PBE + U levels, the weakest mode (ω_{48}) of the D_{5h} structure is characterized by an imaginary frequency of 124–146 i cm^{-1} and the penultimate modes ω_{46} and ω_{47} are degenerate. A slight symmetry breaking can be noticed in the values of ω_{46} and ω_{47}; it arises from the fact that the actual frequency calculations were performed without enforcing symmetry restrictions.

At the PBE level, the structure obtained with D_5 symmetry constraints is a second-order saddle point with two degenerate imaginary frequencies whereas at the PBE + U level, for U_{eff} >

0 the frequencies indicate a minimum structure. For increasing values of U_{eff}, the trend seen in the frequencies of D_5 and C_1 structures are similar to the trend of the geometry parameters (Table 6.6) and the energetics (Table 6.7). For U_{eff} = 1.0 eV, the frequencies of D_5 and C_1 structures are different, implying that these two structures are different. For U_{eff} = 2.0 eV, the C_1 structure is identical to the D_5 structure, and the corresponding frequencies are similar.

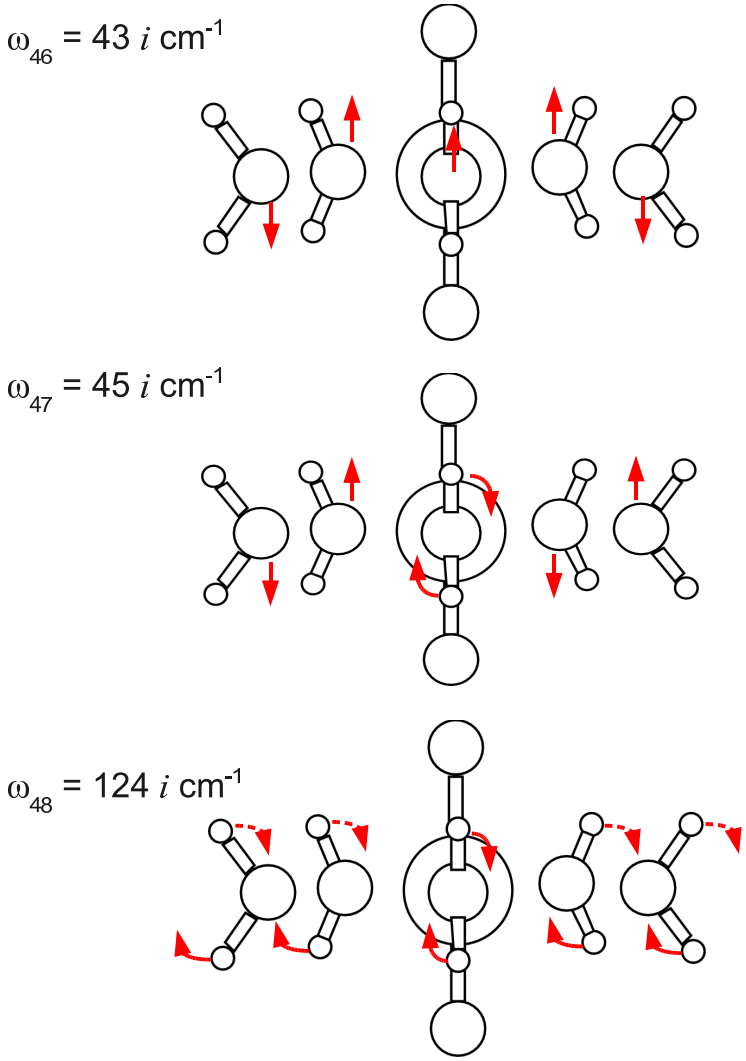

Figure 6.5: Modes corresponding to the three imaginary harmonic frequencies of $[UO_2(H_2O)_5]^{2+}$ at the AE DKH PBE level with D_{5h} symmetry restriction. Geometry relaxation of the D_{5h} structure to the D_5 structure occurs through the mode characterized by the frequency ω_{48} by tilting the molecular planes of the water ligands by about 20° with respect to the uranyl axis.

The mode vectors corresponding to the normal modes of the imaginary frequencies of the D_{5h} structure at the PBE level are shown in Figure 6.5. One notes that the geometry relaxation of the D_{5h} structure to the D_5 structure occurs through ω_{48} by tilting the molecular planes of the water ligands by about 20° with respect to the uranyl axis. The higher modes along which

the D_5 structure distorts to C_1 structure are shown in Figure 6.6. At the PBE level, these modes (ω_{47}, ω_{48}) are degenerate with the frequency value 22 i cm^{-1}. It is interesting to note that such a scheme for distortion of five coplanar water ligands in the D_5 structure through a doubly degenerate normal mode is similar to the mode of distortion of a planar cyclopentane to a more stable boat form. Indeed, by inspecting the C_1 structure at the PBE level (Figure 6.4), one notes that the equatorial oxygen atoms can be connected to form a boat-like structure.

Table 6.7 also summarizes the character of the HOMO of $[UO_2(H_2O)_5]^{2+}$ in terms of Mulliken contributions from the U $5f$ orbitals and the $2p$ orbitals of terminal and equatorial oxygen centers. The net sum of the U $5f$ populations and the $2p$ populations of the terminal oxygen atoms quantifies the contribution of the uranyl σ_u fragment orbital to the HOMO of the penta-aqua uranyl complex, the character of which is predominantly $2p$ (O_w). In the D_{5h} configuration, the uranyl σ_u MO of a_2' character and the non-bonding $2p$ (O_w) MO of a_2'' character are forbidden to interact by symmetry, hence the HOMO of the complex is purely $2p$ (O_w), both in the PBE and the PBE + U calculations. In the D_5 configuration, the corresponding MOs are allowed to interact, i.e. the uranyl σ_u MO and the non-bonding 2_p (O_w)-type MO are of a_2 character. Indeed, in the PBE calculation the uranyl fragment contributes 23% to the HOMO as shown is Figure 6.7.

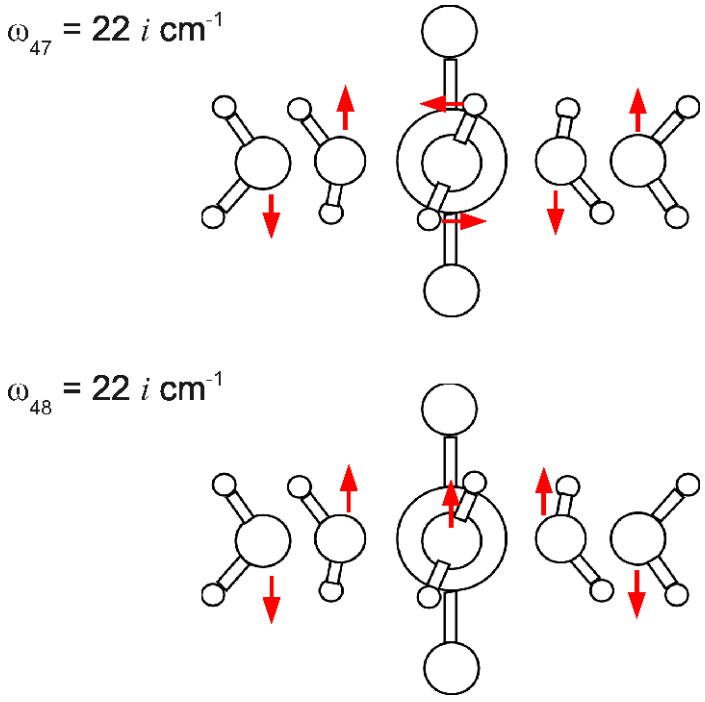

Figure 6.6: Modes corresponding to the three imaginary harmonic frequencies of $[UO_2(H_2O)_5]^{2+}$ at the AE DKH PBE level with D_5 symmetry restriction. Geometry relaxation of the D_5 structure to the C_1 structure occurs through the modes characterized by the frequencies ω_{47} and ω_{48}.

The spurious mixing between the uranyl σ-like and O_w $2p$-like MOs is a consequence of the incomplete self-interaction cancellation in the description of the Coulomb interactions of the U $5f$ orbitals which results in their insufficient localization in LDA and GGA calculations. At the PBE + U level (U_{eff} = 2.0 eV) hybridization of U $5f$ orbitals is penalized and hence the corresponding orbital mixing is suppressed although it would be allowed in D_5 symmetry: 93% of the HOMO are of O_w $2p$ character and only 5% are assigned to the uranyl fragment, mainly σ_u (Table 6.7, Figure 6.7). In the PBE results and to some extent in the PBE + U calculations with the lower Hubbard parameter U_{eff} = 1.0 eV, the oxygen centers of the water ligands leave the equatorial plane as soon as the symmetry constraints are fully relaxed. This leads to a C_1 structure; mixing of uranyl σ_u and O_w $2p$ orbitals again is avoided, this time by phase cancellation (cf. 98% Ow 2p character of the HOMO at the PBE level, Table 6.7). Relaxing the symmetry constraints at the PBE + U level, with a higher value of the Hubbard parameter, U_{eff} = 2.0 eV, has only a minor effect; the geometry and the Mulliken populations are very similar to those of the D_5 structure, Table 6.7.

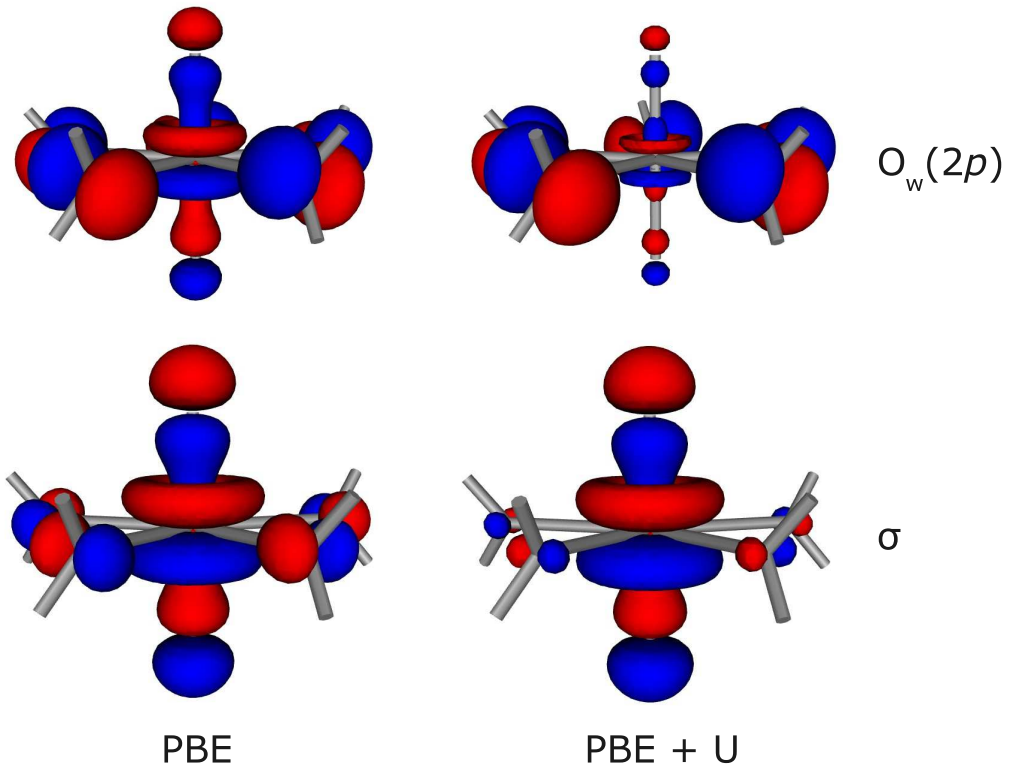

Figure 6.7: Spurious mixing of uranyl σ-like and O_w $2p$-like molecular orbitals of $[UO_2(H_2O)_5]^{2+}$ in D_5 symmetry at the PBE level and its removal at the PBE + U level (U_{eff} = 2.0 eV).

Therefore, the instability of the D_5 structure at the PBE level is related to the above discussed mixing of uranyl σ_u and O_w $2p$ orbitals. Note that this interaction between two closed shells is

repulsive in nature. The PBE data in Table 6.7 show that the HOMO is stabilized by 0.18 eV, together with a significant reduction of the uranyl contribution to the HOMO, when the symmetry is relaxed from D_5 to C_1. At the PBE + U level (U_{eff} = 1.0 eV) the stabilization is smaller and there is no net stabilization with U_{eff} = 2.0 eV. Figure 6.8 shows the repulsive orbital interaction of the HOMO, dominated by O_w $2p$ contributions, and the U $5f$-dominated σ_u MO of uranyl in the PBE structures and its removal by the Hubbard term. Note also the upward energy shift of the uranyl σ_u MO (Figure 6.8). In summary, to the degree it is observed in PBE calculations, the MO mixing is a consequence of the insufficient cancellation of the self-interaction. It induces the observed geometry distortion of the uranyl penta-aqua complex in LDA and GGA calculations. The DFT + U method is known to approximately cure the artifacts of a overly large delocalization of the f orbitals [25] and thus results in less or no tendency (depending on the value of U_{eff}) towards distortion from D_5 symmetry. The distorted structure of the water shell correlates with the uranyl bending angle, in part due to the softness of the uranyl bending mode at the LDA and GGA level. The deviation from linearity of the uranyl moiety is reduced together with the distortion of its solvation shell.

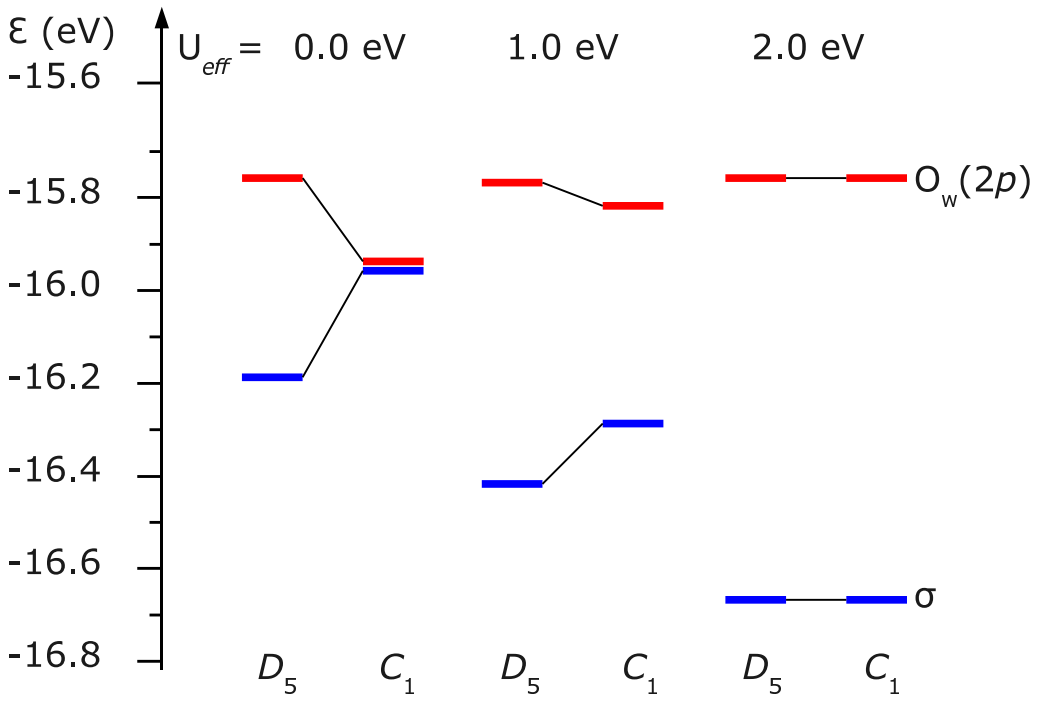

Figure 6.8: Repulsive interaction between uranyl σ-like and O_w $2p$-like molecular orbitals of $[UO_2(H_2O)_5]^{2+}$ in D_5 symmetry and its removal when symmetry is relaxed. KS eigenvalues from PBE and PBE + U calculations for various values of U_{eff} are compared for D_5 and C_1 structures.

6.2.2 Conclusions

Standard GGA functionals underestimate the rigidness of the uranyl moiety with respect to bending distortions. From a detailed analysis of DFT + U results, this has been attributed to an overestimated propensity for a second-order Jahn–Teller-like symmetry breaking. The DFT + U method is capable of correcting this artifact of LDA and GGA calculations. DFT calculations applying the local density approximation or a gradient-corrected exchange-correlation functional showed a distorted geometry of the water shell in the uranyl penta-aqua complex. The combination of this distortion of the ligand shell and too soft a uranyl bending mode results in a notably bent structure of the uranyl moiety in these calculations. The distortion of the water shell is a direct consequence of the spurious mixing of the U $5f$ orbitals with ligand orbitals which manifests itself through a repulsive interaction of two closed shells, namely an MO with substantial U $5f$ character and a non-bonding orbital of the ligand framework. Using scalar relativistic all-electron Douglas–Kroll–Hess calculations, the present study showed that inclusion of a Hubbard-like DFT + U correction with a small positive on-site repulsion parameter U_{eff}) approximately corrects for the self-interaction artifacts in the description of the valence U $5f$-like MOs, leading to a better description of properties of the uranyl (VI) aqua complex.

6.3 Uranyl Monohydroxide

Fractional occupations of the non-bonding δ_u-type quasi $5f$ orbitals of U in the uranyl molecule arise due to a second-order Jahn-Teller type interaction between the uranyl σ_u occupied MO (HOMO of uranyl) and the δ_u-type $5f$ orbitals when uranyl deviates from linearity. In LDA and GGA KS calculations Coulomb repulsion is underestimated for fractional electrons resulting in spurious stabilization of systems with fractionally occupied orbitals. In uranyl complexes with equatorial ligands fractional population of the non-bonding type quasi $5f$ orbitals of uranyl can result also from σ/π donation of electrons from the ligand donor atoms to the U atom. However such a donation is possible only when an equatorial ligand is a strong donor such as anionic ligands like a hydroxyl ion. Theoretical models predicted that the uranyl (VI) molecules of the type $UO_2^{2+}X$ with the equatorial ligands X = H_2O [177], H^- [178], F^- [179], OH^- [180] or O_2^- [181, 182] show a bent uranyl moiety where the deviation from linearity increases with the bond strength of the ligands. Therefore it is of interest to know the strength of the bond between the U center and an equatorial ligand and how much U $5f$ orbitals contribution to such a bond. In neutral aqueous solution, the uranyl ion is usually coordinated by water molecules and hydroxyl ions, solvated $[UO_2(OH)]^+$ appears as hydrolysis product of the uranyl ion in dilute solutions at acidic pH [183]. $[UO_2(OH)]^+$ has been observed in the gas-phase as a product of O_2

oxidation of $[UO(OH)]^+$ in an ion trap-secondary ion mass spectrometric experiment [184] and in an electrospray ionization (ESI) experiment of an aqueous uranyl solution [185]. Both the gas phase and hydrated uranyl monohydroxide species have been subject to a number of theoretical investigations [171, 177, 178, 186, 187]. For the gas-phase uranyl monohydroxide molecule ion, neither experimental nor highly accurate theoretical geometry parameters are known. Thus in the present work, structural aspects of the gas phase molecule $[UO_2(OH)]^+$ has been investigated through a wide range of theoretical methods such as DFT, DFT + U, hybrid-DFT methods B3LYP and PBE0, as well as wavefunction based methods such as many-body perturbation theory of second order, MP2, and a high-level coupled cluster approach, CCSD(T).

In the closed-shell species uranyl monohydroxide $[UO_2(OH)]^+$, static correlation effects are absent; therefore, CCSD(T) predictions should be quite accurate for the complex in the gas phase. For this system, $[UO_2(OH)]^+$, KS density functional calculations employing LDA or GGA level were found to predict geometries deviating from CCSD(T) results. In order to find out if these geometric deviations are related to the improper description of the Coulomb interaction of the U $5f$ orbitals, the DFT + U methodology was invoked for the partially localized $5f$ shell of the uranium atom.

The effects of the spurious self-interaction error present in KS-DFT approximations artificially stabilize delocalized states and solvent effects stabilize localized states [188]. Thus one can expect relatively large effects of self-interaction artifacts for species in the gas phase and a reduction of these effects in the presence of water due to the preference for localized states in solution. Therefore, the hydrated species $[UO_2(OH)(H_2O)_4]^+$ was also studied.

6.3.1 Results and Discussions

The major part of this subsection deals with the discussions of equilibrium geometry parameters of $[UO_2(OH)]^+$, followed by a brief discussion of harmonic vibrational frequencies. Finally the effects of self-interaction artifacts in LDA and GGA calculations on the structural aspects of $[UO_2(OH)]^+$ and the nature of correction provided by the DFT + U method are discussed through an orbital analysis.

Geometry parameters of $[UO_2(OH)]^+$

Table 6.9 summarizes the geometry parameters of the uranyl monohydroxide cation in the gas-phase calculated at different theoretical levels such as AE DKH PBE, AE DKH PBE + U, AE DKH VWN, AE DKH VWN + U, RECP/VWN [178], AE ZORA PW91 [178], RECP/B3LYP [178], RECP/PBE0, RECP/MP2 [186] and RECP/CCSD(T). Not all of these calculations could

b performed at the all-electron level. Before proceeding to the discussion of the main results (Table 6.9), it seems useful to estimate possible effects when core electrons are described by an effective-core potential. For this purpose, results of the AE DKH approach will be compared to those of calculations employing relativistic effective core potentials (RECPs). Similarly, it is appropriate to assess the quality of different basis sets used for the U atom in various calculations.

Table 6.9: Geometry parameters of $[UO_2(OH)]^+$ [a] from various computational methods: Average equilibrium U-O_t bond length $\bar{r}$(U-O_t), equilibrium U-O_h bond length r (U-O_h), uranyl bond angle θ(O_t-U-O_t), two O_t-U-O_h bond angles θ(O_t-U-O_h) and U-O_h-H bond angle θ(U-O_h-H). Bond lengths in pm and bond angles in degrees. Also given is the Hubbard parameter U_{eff} (eV) for the U $5f$ shell.

Method	U_{eff}	$\bar{r}$	r	θ		
		U-O_t	U-O_h	O_t-U-O_t	O_t-U-O_h	U-O_h-H
AE DKH VWN [b]		174.9	199.1	168.3	95.8, 95.8	180.0
AE DKH VWN + U [b]	1.0	174.4	200.1	172.2	92.4, 95.3	153.7
AE DKH VWN + U [b]	2.0	174.0	201.2	174.9	91.6, 93.5	144.5
AE DKH PBE [b]		176.5	202.1	166.7	94.9, 98.3	158.8
AE DKH PBE + U [b]	1.0	176.1	203.1	171.2	92.7, 96.0	145.6
AE DKH PBE + U [b]	2.0	175.6	204.2	174.1	92.0, 96.0	138.6
RECP/VWN [c]		174.7	198.5	167.6	96.2, 96.2	180.0
AE ZORA PW91 [c]		176.1	201.9	167.9	94.4, 97.7	151.8
RECP/B3LYP [b]		174.2	201.4	167.9	94.9, 97.2	154.2
RECP/B3LYP [c]		175.1	199.9	167.2		
RECP/PBE0 [b]		172.3	200.0	170.0	93.7, 96.3	149.4
RECP/MP2 [b]		177.7	200.3	171.8	93.7, 94.5	140.0
RECP/MP2 [d]		176.7				
RECP/CCSD(T) [b]		173.6	201.3	170.7	93.8, 95.6	148.1
RECP/CCSD(T) [b,e]		174.1	201.8	170.7	93.8, 95.6	148.1

[a] Point group symmetry C_s.
[b] This work.
[c] Ref. [178]
[d] Ref. [186]
[e] Including an estimated AE DKH core correction of +0.5 pm to the bond lengths U-O_t and U-O_h.

AE DKH correction to RECP/CCSD(T) results: As no experimental geometry is available for the gas phase $[UO_2(OH)]^+$ molecule, the equilibrium geometry calculated at the accurate CCSD(T) level is chosen as a reliable reference. To estimate the error introduced in the CCSD(T) calculation due to the RECP representation of the core electrons, results of VWN calculations

carried out with the same RECP [189] are compared with the results of the AE DKH approach using uncontracted basis sets to achieve a more accurate result (rows 2 and 3 of Table 6.10). Introduction of the RECP results in a contraction of the U-O_t bond by 0.5 pm and of the U-O_h bond by 0.6 pm, while changes in angles are smaller than 0.1 degree (Table 6.10). Similar contractions of U-X bonds have been obtained earlier for uranyl (0.7 pm) and UF_6 (0.8 pm) for the same RECP with the VWN approach [190]. A larger decrease of the uranyl bond of 1.6 pm due to this RECP has been calculated with the BP XC functional [190]. Thus, a contraction of U-X bonds by 0.5 pm and no change of bond angles seems to be a reasonable estimate for the core-correction to RECP results from CCSD(T) calculations. This leads to a reference geometry for uranyl monohydroxide with the bond lengths U-O_t = 174.1 pm, U-O_h = 201.8 pm and the same angles as obtained in the RECP/CCSD(T) calculation (Table 6.10).

Estimation of uncertainties due to various basis sets: In the B3LYP, PBE0 and MP2 calculations performed using the program Turbomole and in the CCSD(T) calculations performed using the program Molpro, aug-cc-pVTZ basis sets were used for the atoms O and H. For the U atom, the segmented contracted def-TZVP basis set used in the Turbomole calculations is of the same quality as the generalized contracted basis set used in the Molpro CCSD(T) calculation. The specific details of these basis sets are given in Chapter 4 and Appendix I. Compared with the basis sets used in the hybrid-DFT and wavefunction based methods, the basis sets used in the DFT and DFT + U calculations performed using the program PARAGAUSS are of different size and quality. Thus in order to estimate the uncertainties in geometry parameters due to various basis sets used in the present work (Table 6.9), a set of systematic calculations were performed at the RECP/VWN and AE DKH VWN levels (Table 6.10).

First of all, row 5 of Table 6.10 presents the results of a RECP/VWN calculation which employs the same basis sets as the CCSD(T) calculation (row 6 of Table 6.10). With respect to the results of row 5, changing the U basis set to an uncontracted basis set or changing the aug-cc-pVTZ to the standard basis sets for O and H atoms introduces negligible deviations. Rows 3 and 4 of Table 6.10 differ only by the basis set used for the U atom. When compared to the quality of the (14s, 13p, 10d, 8f, 6g) basis set used in the CCSD(T) calculations (row 4), the larger (24s, 19p, 16d, 11f) basis set (row 3) relaxes the U-O_t, and U-O_h bonds by 0.4 pm and 0.2 pm, respectively, and the O_t-U-O_t bond angle by 0.2° and O_t-U-O_h bond angle by 0.1°. Finally through the results of the AE DKH VWN calculations (rows 1 and 2 of Table 6.10), one notes that when compared to the quality of the uncontracted (24s, 19p, 16d, 11f) basis set, the contracted basis set (24s, 19p, 16d, 11f)→[10s, 7p, 7d, 4f] which uses AE-DKH-VWN atomic eigenvectors relaxes the U-O_t, and U-O_h bonds by 0.3 pm and 0.1 pm, respectively, leaving

all other geometry parameters unchanged. Thus variations in results due to different basis sets (uncontracted) are marginally larger than the effects due to specific basis set contraction (Table 6.10). From these results we estimate uncertainties due to specific basis sets to be at most 0.5 pm for distances and at the maximum 0.2° for bond angles. Such uncertainties are rather small indeed.

Table 6.10: Comparison of geometry parameters of $[UO_2(OH)]^+$ [a] in VWN and CCSD(T) methods employing various basis sets and pseuopotentials: Average equilibrium U-O_t bond length $\bar{r}$(U-O_t), equilibrium U-O_h bond length r(U-O_h), equilibrium O_h-H bond length r(O_h-H), uranyl bond angle θ(O_t-U-O_t), two O_t-U-O_h bond angles θ(O_t-U-O_h) and U-O_h-H bond angle θ(U-O_h-H). Bond lengths in pm, bond angles in deg.

Method	$\bar{r}$	r		θ		
	U-O_t	U-O_h	O_h-H	O_t-U-O_t	O_t-U-O_h	U-O_h-H
AE DKH VWN [b]	174.9	199.1	98.2	168.3	95.8, 95.8	180.0
AE DKH VWN [c]	174.6	199.0	98.0	168.3	95.8, 95.8	180.0
RECP/VWN [c]	174.1	198.4	98.1	168.3	95.8, 95.8	180.0
RECP/VWN [d]	173.7	198.2	98.1	168.5	95.7, 95.7	180.0
RECP/VWN [e]	173.7	198.1	98.1	168.5	95.8, 95.8	180.0
RECP/CCSD(T) [e]	173.6	201.3	96.6	170.7	93.8, 95.6	148.1
RECP/CCSD(T) [f]	174.1	201.8	96.6	170.7	93.8, 95.6	148.1

[a] Point group symmetry C_s.
[b] Basis sets U: (24s, 19p, 16d, 11f)→[10s, 7p, 7d, 4f] with AE DKH VWN contraction, O: (9$_s$, 5p, 1d)→[5s, 4p, 1d], H: (6s, 1p)→[4s, 1p].
[c] Basis sets U: (24s, 19p, 16d, 11f), O: (9s, 5p, 1d), H: (6s, 1p).
[d] Basis sets U: (14s, 13p, 10d, 8f, 6g), O: (9s, 5p, 1d), H: (6s, 1p).
[e] Basis sets U: (14s, 13p, 10d, 8f, 6g)→[6s, 6p, 5d, 4f, 3g], O: aug-cc-pVTZ (11s, 6p, 3d, 2f)→[5s, 4p, 3d, 2f], H: aug-cc-pVTZ (11s, 6p, 3d, 2f)→[5s, 4p, 3d, 2f].
[f] Including an estimated AE DKH core correction of +0.5 pm to U-O_t and U-O_h bond lengths (according to rows 2 and 3 of this table).

VWN, VWN + U results: Compared to the reference CCSD(T) value that includes an estimated core-correction to the RECP (Table 6.9), the VWN value for the U-O_t bond length is larger by 0.8 pm and the U-O_h bond length is shorter by 2.7 pm. The VWN value for the uranyl angle O_t-U-O_t is 168° which is slightly smaller than the reference value of 171°. As the most remarkable difference between CCSD(T) and DFT VWN calculations the U-O_h-H angle has to be noted, which is 180° (linear U-O_h-H) for VWN and 148° for CCSD(T). This remarkable deviation has been observed earlier in a RECP-VWN calculation [178] and is also reproduced in

the VWN-RECP calculations performed in the present work (Table 6.10). DFT + U results as obtained with the VWN functional show decreasing uranyl bond lengths and an increasing U-O_h bond with increasing value of U_{eff} (Table 6.9). The parameters calculated for U_{eff} = 2 eV, U-O_t = 174.0 pm and U-O_h = 201.2 pm agree with the reference up to the uncertainties due to basis sets (see discussions above). The uranyl angle O_t-U-O_t increases with increasing U_{eff} from 168° to 175°, finally overestimating somewhat the reference of 171°. The most prominent effect of the DFT + U method is a strong decrease of the U-O_h-H angle from 180° for U_{eff} = 0 eV to 145° for U_{eff} = 2 eV (Figure 6.10), which is in good agreement with the CCSD(T) reference of 148° (Table 6.9). Overall the DFT + U approach leads to a notable improvement of the VWN results.

PBE, PBE + U results: Comparison of PBE and PBE + U calculations reveals the same trends as obtained for the VWN calculations when varying U_{eff} (Table 6.9). The PBE value of U-O_t = 176.5 pm is overestimated compared to the reference of 174.1 pm by 2.4 pm and the corrections provided by the onsite-Coulomb parameter U_{eff} = 2.0 eV only partially improves the result by 0.9 pm. The U-O_h bond length, already overestimated at the PBE level (202.1 pm), increases further in the DFT + U calculations up to 204.2 pm. Both these changes of bond lengths due to self-interaction correction, -0.9 pm for U-O_t and +2.1 pm for U-O_h, agree with the corresponding VWN + U corrections (Table 6.9). Also the uranyl angle O_t-U-O_t increases with increasing U_{eff} from 167° (0 eV) to 174° (2 eV), slightly overestimating the CCSD(T) result of 171°. In contrast to the VWN results, PBE yields a bent OH orientation with an angle U-O_h-H of 159°, which decreases to 139° for U_{eff} = 2 eV. Thus, PBE slightly overestimates that angle and the DFT + U correction provided through the U_{eff} value of 2.0 eV leads to a comparable underestimation of about 10° (Table 6.9). Overall, comparison of VWN and PBE results reveals the same trends for the effects of the self-interaction corrections and shows the known overestimations of bond lengths of heavy elements compounds for GGA compared to LDA [190]. Similar results as obtained here with PBE have been earlier calculated with the PW91 GGA functional, applying the AE ZORA relativistic approach [178] (Table 6.9).

B3LYP, PBE0 and MP2 results: The RECP/B3LYP values for the geometry parameters of $[UO_2(OH)]^+$ are in good agreement with the CCSD(T) reference. The uranyl bond length calculated as 174.2 pm (this work) as well as the U-O_h bond length of 201.4 pm (this work) agree very well with the reference values of 174.1 and 201.8 pm, respectively. Also the bond angles O_t-U-O_t = 168° and U-O_h-H = 154° match the reference with deviations of 6° at most (Table 6.9). Slightly worse bond distances of U-O_t = 175.1 pm and U-O_h = 199.9 pm have previously been calculated by means of the B3LYP approach [178]. The bond distances determined with

Table 6.11: VWN-LDA and PBE-GGA geometry parameters of $[UO_2(OH)]^+$ [a] from constrained geometry optimizations where $\theta(O_t\text{-}U\text{-}O_t)$ is fixed to 180° along with results from corresponding DFT + U levels. Average equilibrium U-O_t bond length $\bar{r}$(U-O_t), equilibrium U-O_h bond length r(U-O_h), equilibrium O_h-H bond length $r(O_h\text{-H})$, two O_t-U-O_h bond angles $\theta(O_t\text{-U-}O_h)$ and U-O_h-H bond angle θ(U-O_h-H). Bond lengths in pm, bond angles in degree. Also given is the Hubbard parameter U_{eff} (eV) for the U $5f$ shell.

Method	U_{eff}	$\bar{r}$	r	θ	
		U-O_t	U-O_h	O_t-U-O_h	U-O_h-H
AE DKH VWN		174.7	199.4	88.9, 91.1	146.2
AE DKH VWN + U	1.0	174.3	200.4	89.1, 90.9	141.9
AE DKH VWN + U	2.0	174.0	201.4	89.5, 90.5	138.4
AE DKH PBE		176.3	202.6	89.0, 91.0	139.4
AE DKH PBE + U	1.0	176.0	203.5	89.3, 90.7	136.3
AE DKH PBE + U	2.0	175.6	204.5	89.7, 90.3	133.6

[a] Point group symmetry C_s.

the PBE0 hybrid functional employing a small-core RECP, U-O_t = 172.3 pm and U-O_h = 200.0 pm, deviate slightly more from the reference compared to the RECP/B3LYP values. On the other hand, PBE0 yields rather accurate angles, O_t-U-O_t = 170° and U-O_h-H = 149°, which agree up to 2° with the reference values. Compared to LDA and GGA results (see above), it is obvious that hybrid functionals provide better results. This improved performance is rationalized partially by the inclusion of an admixture of exact exchange in these functionals, which reduces self-interaction artifacts, especially for the PBE0 functional which includes a larger fraction of exact exchange than the B3LYP functional. Interestingly, MP2 calculations, which are free of self-interaction artifacts, yield rather long uranyl bonds, 177.7 pm (this work) and 176.7 pm [187] for uranyl monohydroxide, which are comparable to GGA results (Table 1). The U-O_h bond of 200.3 pm as obtained with the MP2 approach as well as the angles O_t-U-O_t = 172° and U-O_h-H = 140°, on the other hand, are in acceptable agreement with the CCSD(T) derived reference. Thus, relatively long bond lengths as obtained in GGA and MP2 calculations are probably not the result of unphysical self-interaction, but have to be ascribed to an insufficient representation of dynamic correlation.

Structural analysis: The DFT + U results show as essential effects of self-interaction elongation of the uranyl bond (which may be interpreted as a bond weakening) and as a consequence a contraction of the U-O_h ligand bond length due to bonding competition at the uranium center.

Due to the presence of an equatorial ligand, the uranyl moiety is slightly bent (Table 6.9). As in the case of the bare uranyl ion (Section 6.1 and see below), this effect decreases with increasing U_{eff} in line with an increased frequency for the uranyl bending vibrational mode. Constrained geometry optimizations (for a fixed, linear uranyl moiety) revealed that the strong change of the angle U-O_h-H with change in U_{eff} is an indirect effect due to the bending of uranyl. Optimizations of $[UO_2(OH)]^+$ with a fixed linear uranyl subunit as carried out with VWN, VWN + U, PBE and PBE + U approaches yield very much smaller effects (Table 6.11). In the VWN and VWN + U calculations, in unconstrained optimizations U-O_h-H decreases by 35° when U_{eff} is varied from 0 to 2 eV while for a fixed straight uranyl geometry this angle decreases only from 146.2° to 138.4° (by 8°) for the same variation of U_{eff}. A similar trend is also noted in the PBE and PBE + U calculations where in the constrained optimizations with linear uranyl, the U-O_h-H angle is less affected by U_{eff} (Table 6.11).

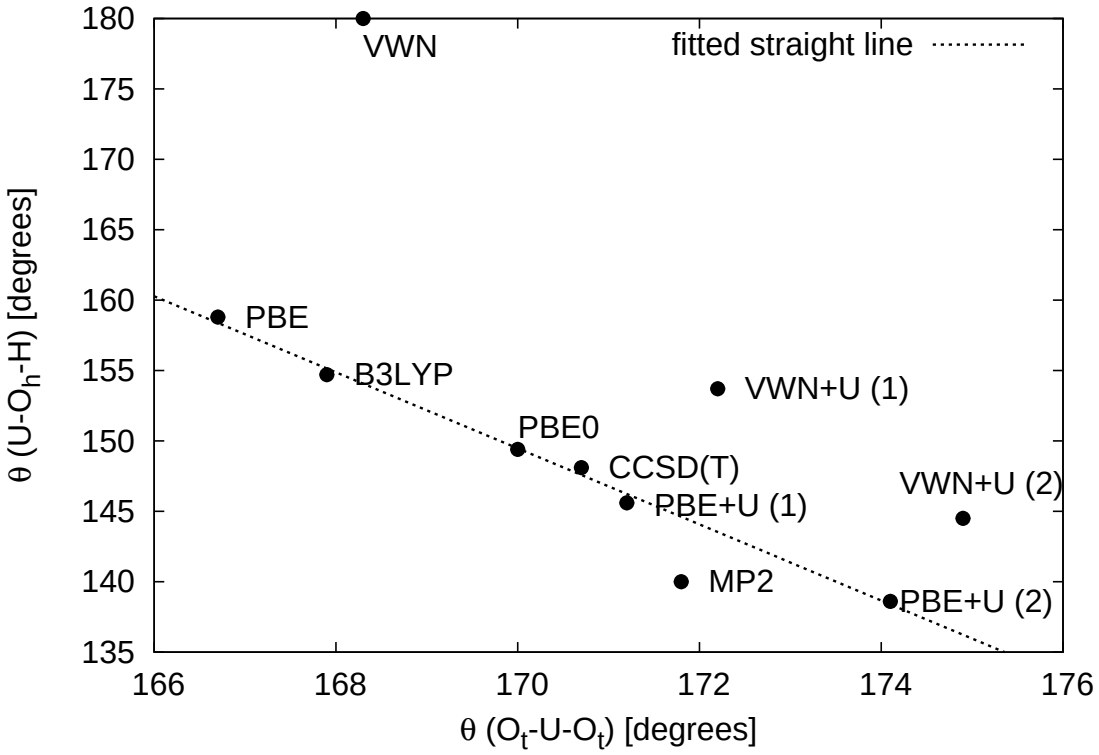

Figure 6.9: Correlation between O_t-U-O_t and U-O_h-H bond angles of uranyl monohydroxide according to various methods: While fitting the straight line, MP2, VWN and VWN + U values were ignored to give the correlation coefficient 0.998. The U_{eff} values used in the DFT + U calculations are given in the parentheses.

This finding is of special interest as it shows that indirect effects of self-interaction artifacts for geometry parameters may be sizeable for soft degrees of freedom. With the focus on the performance of various methods in describing the uranyl and U-O_h-H bond angles, the correlation

between these two angles according to various methods is illustrated in Figure 6.9. Except for the methods VWN, VWN + U and MP2, all other methods show a linear correlation between uranyl and U-O_h-H bond angles. The PBE values of O_t-U-O_t and U-O_h-H angles which approximately fall on in the fitted straight line lie farther away from the CCSD(T) values; results of both hybrid-DFT methods B3LYP and PBE0 lie on the straight line where the PBE0 values are close to the CCSD(T) values. The PBE + U (U_{eff} = 1 eV) values are also close to the CCSD(T) value but on the other side of PBE0 values. For U_{eff} = 2 eV, the deviation of the PBE + U results for O_t-U-O_t and U-O_h-H bond angles are similar in size as those of the PBE values, but of opposite sign (Figure 6.9).

Harmonic vibrational frequencies of $[UO_2(OH)]^+$

Table 6.12 summarizes the harmonic vibrational frequencies of the uranyl monohydroxide cation in gas phase, calculated at different theoretical levels such as AE DKH PBE, AE DKH PBE + U, AE DKH VWN, AE DKH VWN + U, RECP/B3LYP [178], RECP/PBE0, RECP/MP2 [187], RECP/CCSD(T) along with available experimental results in aqueous solution [183]. The largest frequency (ω_1) corresponds to O-H stretching for which the CCSD(T) reference value is 3810 cm^{-1}. The CCSD(T) reference values for the uranyl asymmetric (ω_2) and symmetric (ω_3) stretching frequencies are 1022 and 944 cm^{-1}, respectively. These frequencies are underestimated in the VWN approximation, by 12 and 16 cm^{-1} respectively. At the VWN + U level for the value of U_{eff} = 1.0 eV, these values are improved towards the CCSD(T) values by 16 and 8 cm^{-1} respectively. For the higher value U_{eff} = 2.0 eV, the VWN + U values for the asymmetric stretch frequency (ω_2) is larger than the CCSD(T) value by 17 cm^{-1} while the symmetric stretch frequency (ω_3) is identical to the CCSD(T) value (Table 6.12). At the PBE level, the values for ω_2 and ω_3 are underestimated by 46 and 49 cm^{-1} respectively. At the PBE + U (U_{eff} = 2.0 eV) these values are improved by 27 and 14 cm^{-1}, respectively. The B3LYP results for ω_2 and ω_3 (present work and [178]) are in excellent agreement with the reference values. At the PBE0 level, both the frequencies ω_2 and ω_3 are overestimated by 46 cm^{-1}, while at the MP2 level (this work), these frequencies are overestimated by 49 cm^{-1} and 66 cm^{-1}, respectively, when compared to the CCSD(T) reference value.

The next two smaller frequencies are ω_4 (U-O_h stretching) and ω_5 (torsion of the O_h-H group), which lie in the range 500–700 cm^{-1}. Both in VWN and PBE levels, inclusion of U_{eff} increases the value of ω_4 and decreases the value of ω_5. The VWN value of ω_4, 694 cm^{-1}, is very close to the CCSD(T), 683 cm^{-1}. For U_{eff}=1.0 eV, the VWN + U value of ω_4 is essentially the same as the reference value. In contrast, the PBE value of ω_4 is 660 cm^{-1} which underestimates the reference value by 23 cm^{-1}; for positive values of U_{eff}, the PBE + U results are even lower,

underestimating the reference by 33 cm^{-1} and 40 cm^{-1} for the values of U_{eff} = 1.0 and 2.0 eV, respectively. The reference value of ω_5, 553 cm^{-1}, is underestimated at the VWN and PBE levels by 40 and 53 cm^{-1} respectively. For the value of U_{eff} = 2.0 eV, VWN + U and PBE + U levels improve ω_5 by 29 and 38 cm^{-1} respectively. For both ω_4 and ω_5, on an average, the PBE0 values are closer to the reference values than B3LYP and MP2 results.

The lowest four frequencies $\omega_6 - \omega_9$ lie below 500 cm^{-1} of which the modes correspond to $\omega_6 - \omega_8$ are in-plane bending modes and ω_9 represents an out-of-plane bending or wagging mode. The description of these lower-frequency modes is perhaps more relevant to the stability of the equilibrium geometry of $[UO_2(OH)]^+$. Since the complex is planar, one can expect the magnitude of the in-plane bending modes to be more relevant to the equilibrium bond angles. The largest of these four frequencies ω_6 corresponds to the U-O_h-H bending mode and ω_7 corresponds to the rocking of the uranyl group. In the gas phase, the bending mode of uranyl is doubly degenerate corresponding to bending in two equivalent planes. In the uranyl monohydroxide molecule with the introduction of an equatorial ligand, the uranyl bending modes are split into ω_7, the O_t-U-O_t in-plane bending or scissoring mode and ω_9 O_t-U-O_t, an out-of-plane bending or wagging mode.

The normal modes corresponding to the frequencies $\omega_6 - \omega_8$ frequencies are of the same symmetry (a′), As these frequencies are quite similar in size, one can expect mixing between the corresponding normal modes. The CCSD(T) values for these modes are 340, 210 and 185 cm^{-1} respectively. Both hybrid-DFT methods B3LYP and PBE0 predict these three frequencies fairly well but the MP2 values are slightly overestimated, up to 60 cm^{-1} for ω_8. This findings perhaps allow one to rationalize why B3LYP and PBE0 methods to predict the bond angles of $[UO_2(OH)]^+$ better than the MP2 method (Table 6.9, Figure 6.9). At this point, it is important to note that an accurate prediction of all three frequencies $\omega_6 - \omega_8$ is important for describing the bond angles O_t-U-O_h and U-O_h-H, considering the fact that the normal modes of $\omega_6 - \omega_8$ may couple. For the value of U_{eff} = 1.0 eV, both VWN + U and PBE + U levels predict $\omega_6 - \omega_8$ reasonably well compared to the VWN and PBE values and the corresponding DFT + U results for the higher value U_{eff} = 2.0 eV. The coupling between these three modes can be understood through the potential energy distribution (PED) along these normal mode coordinates in terms of the three internal coordinates. The PED was performed at the PBE and the PBE + U levels; the results, given as footnotes to Table 6.12, indicate the coupling between these three normal modes ($\omega_6 - \omega_8$).

The out-of-plane uranyl bending mode ω_9 is easy to describe because it has the symmetry a″ while the other lower modes belong to the symmetry type a′ and the next higher mode of a″ symmetry corresponds to ω_5 in the planar $[UO_2(OH)]^+$ molecule. Thus ω_9 mode is well

Table 6.12: Harmonic vibrational frequencies ω [a] (in cm^{-1}) of $[UO_2(OH)]^+$ [b] from various computational methods: Also given is the Hubbard parameter U_{eff} (eV) for the U $5f$ shell along with available experimental data.

Method	U_{eff}	ω_1	ω_2	ω_3	ω_4	ω_5	ω_6	ω_7	ω_8	ω_9
AE DKH VWN [c]		3669	1010	928	694	513	269	227	95	140
AE DKH VWN + U [c]	1.0	3674	1026	936	686	530	332	219	182	170
AE DKH VWN + U [c]	2.0	3677	1039	944	648	542	381	234	217	197
AE DKH PBE [c,d,e]		3680	976	895	660	500	311	200	117	145
AE DKH PBE + U [c,d,f]	1.0	3680	989	901	650	510	374	213	204	170
AE DKH PBE + U [c,d,g]	2.0	3686	1003	909	643	538	439	240	213	195
RECP/B3LYP [c]		3769	1026	946	672	515	321	207	168	165
RECP/B3LYP [h]			1025	946	679					
PBE0/RECP [c]		3823	1068	990	691	533	350	216	193	179
MP2/RECP [c]		3770	973	878	701	587	400	219	90	164
MP2/RECP [i]			969	884						
RECP/CCSD(T) [c]		3810	1022	944	683	553	340	210	185	168
Exp. [j]				849						

[a] Assignments: ω_1 (a′) – O-H stretching, ω_2 (a″) – U-O_t asymmetric stretching, ω_3 (a′) – U-O_t symmetric stretching, ω_4 (a′) – U-O_h stretching, ω_5 (a″) – O_h-H torsion, ω_6 (a′) – U-O_h-H bending, ω_7 (a′) – O_t-U-O_t scissoring, ω_8 (a′) – O_t-U-O_t rocking, ω_9 (a″) – O_t-U-O_t wagging.

[b] Point group symmetry C_s.

[c] This work.

[d] The potential energy distribution (PED) is given only for the in-plane bending modes as sum of percentages of the three coplanar normal mode coordinates ω_6, ω_7 and ω_8 along the bond angles: U-O_h-H, O_{t_1}-U-O_h and O_{t_2}-U-O_h where O_{t_1} is the terminal oxygen atom which is *cis* w.r.t the hydroxyl H atom and O_{t_2} is the terminal oxygen atom which is *trans* w.r.t the hydroxyl H atom.

[e] PED: ω_6 (54 + 47 + 0), ω_7 (0 + 0 + 100), ω_8 (47 + 52 + 0).

[f] PED: ω_6 (75 + 26 + 3), ω_7 (18 + 49 + 33), ω_8 (5 + 20 + 70).

[g] PED: ω_6 (87 + 13 + 2), ω_7 (12 + 73 + 15), ω_8 (0 + 0 + 100).

[h] Ref. [178].

[i] Ref. [187].

[j] In aqueous solution, Ref. [183].

separated in energy from the other modes and the eigenvector of the corresponding normal mode essentially does not mix with other normal modes. The CCSD(T) value for the out-of-plane uranyl bending mode is 168 cm^{-1}; the corresponding B3LYP and MP2 results are 165 and 164 cm^{-1} respectively. The PBE0 value, 179 cm^{-1}, slightly overestimates the reference. These frequencies are identical to the bending frequency of the bare uranyl dication, 178 cm^{-1} at the CCSD(T) level and 166 cm^{-1} at the B3LYP level, (Table 6.1). At the PBE level, the frequency of the bending mode of bare uranyl ion is 92 cm^{-1} (Table 6.1) which is notably improved in $[UO_2(OH)]^+$ molecule at the VWN level, (140 cm^{-1}), and the PBE level, (145 cm^{-1}). For U_{eff} = 1.0 eV, both VWN + U and PBE + U levels predict the value of ω_9 to be 170 cm^{-1}, which is very close to the reference.

Table 6.13: Population analysis of the valence molecular orbitals (MOs) of UO_2OH^+ [a] from VWN and VWN + U calculations: orbital energies ε_i (eV) and Mulliken atomic gross populations (as percentage).

Type	MO	VWN					VWN + U [b]				
		ε_i	Population				ε_i	Population			
			U f	O_{t_1} p [c]	O_{t_2} p [c]	O_h p		U f	O_{t_1} p [c]	O_{t_2} p [c]	O_h p
a′	41	-12.94	31	12	12	38	-12.99	17	7	9	59
	40	-14.68	17	34	33	4	-15.09	25	50	4	10
	39	-14.68	34	14	14	31	-14.71	35	6	35	10
	36 [d]	-18.23	7	2	2	53	-17.84	7	5	2	52
a″	17	-14.44	10	5	5	71	-14.04	6	0	1	81
	16	-15.18	26	28	28	12	-15.39	29	31	34	1

[a] Point group symmetry C_s.
[b] U_{eff} = 2.0 eV for the U 5f shell.
[c] O_{t_1} is the terminal oxygen atom which is *cis* w.r.t the hydroxyl H atom and O_{t_2} is the terminal oxygen atom which is *trans* w.r.t the hydroxyl H atom.
[d] Both in VWN and VWN + U calculations, this MO has 15% H(1s) contribution, which is not listed. This MO has the $O_h(2p)$-H(1s) sigma character.

Population analysis

Table 6.13 summarizes the population analysis of six valence molecular orbitals (MOs) of the uranyl monohydroxide cation based on Mulliken gross atomic populations. The main purpose of the population analysis is to characterize the three uranyl-like MOs (one σ and two π) and the three 2p-dominated MOs that correspond to two non-bonding 2p-like orbitals and a $O_h(2p)$ - H(1s) σ-like orbital. Since the essential features of these orbitals are the same in both the VWN

and the PBE levels, only the VWN and VWN + U results are presented and discussed here. The interactions among the valence MOs are predominantly in the molecular plane, i.e., only the MOs of the symmetry a′ show large mixing.

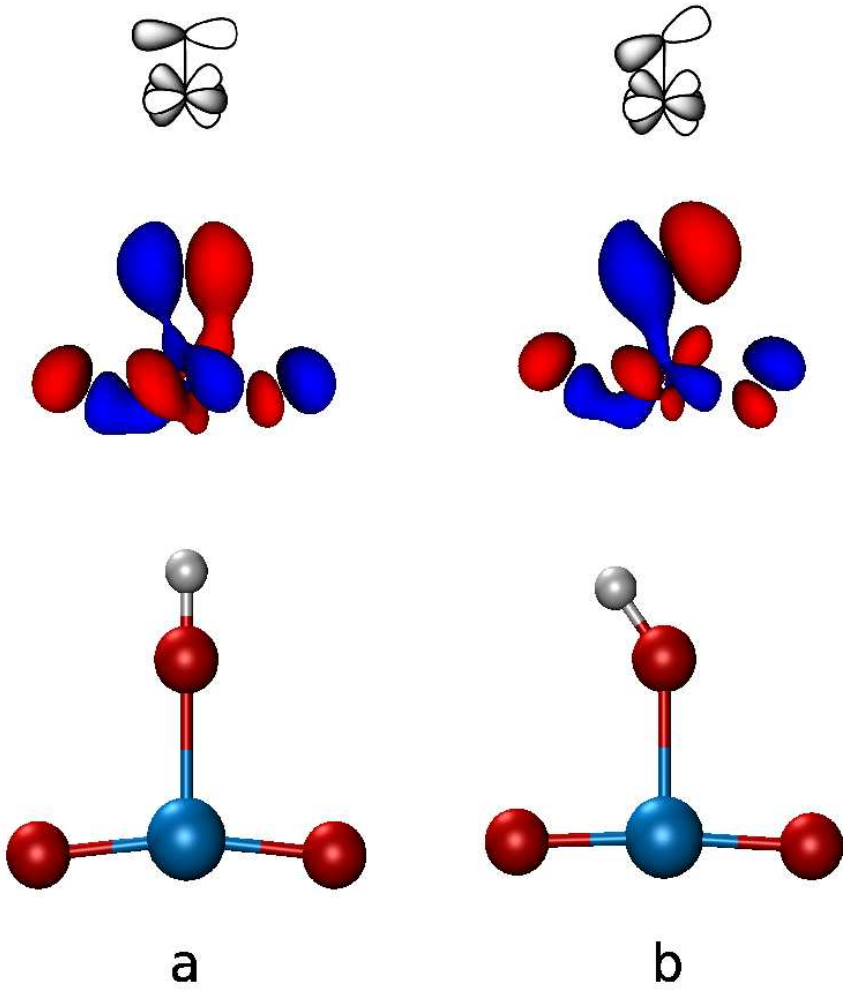

Figure 6.10: Equilibrium geometry and sketch of the HOMO (41 a′) of uranyl monohydroxide: (a) AE DKH VWN, (b) AE DKH VWN + U (U_{eff} = 2.0 eV). The interaction between the uranyl dication and the hydroxyl anion in UO_2OH^+ changes its character from short-range π to long-range σ-like. In the schematic representation (top) of the orbital interaction, the uranyl σ contribution is not shown; and the only quasi $5f_{z(x^2-y^2)}$ contribution is shown on the U center for easy interpretation.

Both at the VWN and the VWN + U (U_{eff} = 2.0 eV) levels, the lowest of the six listed orbitals, 36a′, can be easily characterized as the hydroxyl $O_h(2p)$ - H(1s) sigma bonding orbital. In the VWN geometry with the linear U-O_h-H configuration, this MO slightly mixes with MO 40a′, which is an uranyl in-plane $^{\pi}$ MO; in the and in the bent U-O_h-H configuration (VWN + U) this interaction is removed resulting in the stabilization of 40 a′ by +0.4 eV and a destabilization

of the O_h-H σ orbital, 36a′, by -0.4 eV. In the VWN calculation, MO 39a′ has the character of the uranyl σ bond with a weak π-donation by the hydroxyl $2p$ to the *dough nut* rings of the σ bond which is minimized with the introduction of U_{eff} then the $2p$ character decreases from 30% to 10%. As a distinct feature, the highest occupied molecular orbital (HOMO) 41 a′ of $[UO_2(OH)]^+$ which is easily identified as the O_h ($2p$)non bonding-type orbital in the VWN + U calculation but insufficient localization of the $5f$ orbital in the VWN calculation prevents such a characterization of the HOMO of the VWN calculation. This latter MO shows a π-donation in the VWN calculation with a short U-O_h bond but in the VWN + U calculation with a slightly longer U-O_h bond, it changes its character to a weak σ-type interaction by a rotation in order to account for better overlap between the non-bonding type $2p$ orbital of the hydroxyl O center and a δ-type $5f$ contribution at the U center (Figure 6.10).

Going from VWN to VWN + U, one notes that the slight mixing between the MO 16a″, of uranyl π character, and MO 17a″ which is a non-bonding O_h ($2p$) orbital, is removed as the former MO is shifted down by 0.2 eV and the latter shifted up by 0.4 eV. This decoupling can be partly related to both the decrease in in U-O_t bond length and an increase in the U-O_h bond length.

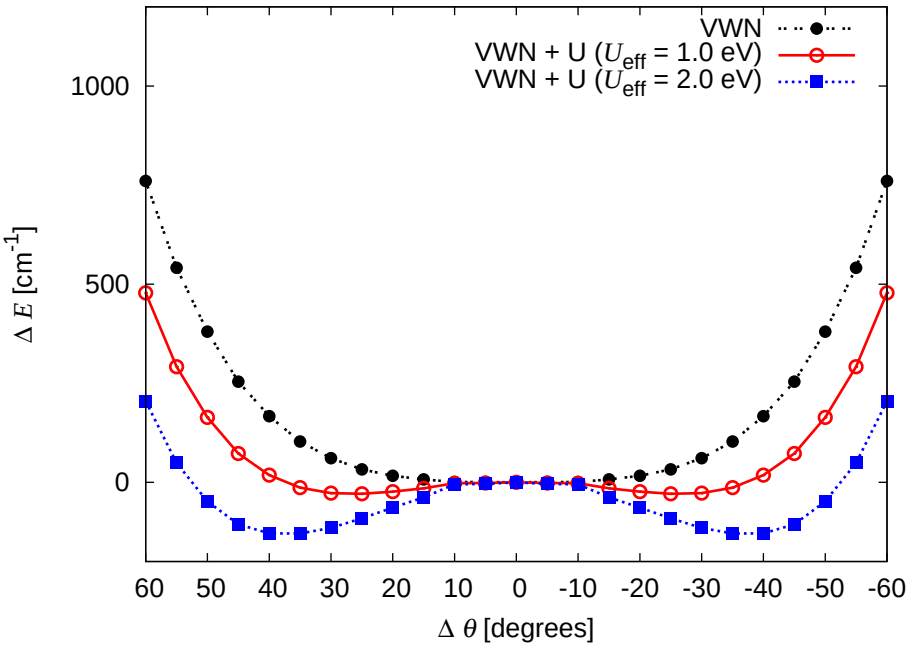

Figure 6.11: Potential energy profiles of $[UO_2(OH)]^+$ along the U-O_h-H bending mode from AE DKH VWN and AE DKH VWN + U calculations. For various angles of deviation $\Delta\theta$ (in degree) from linearity (180°) of the U-O_h-H fragment, relative energies ΔE (in cm^{-1}) are plotted. The energies were obtained by constrained geometry optimizations of $[UO_2(OH)]^+$ at various fixed values of θ(U-O_h-H).

Second-order Jahn-Teller type interaction in $[UO_2(OH)]^+$

Figure 6.11 shows the energy profiles of $[UO_2(OH)]^+$ along the U-O_h-H bending mode, as calculated at the VWN and the VWN + U methods. The VWN potential energy profile shows a minimum for the linear structure of the U-O_h-H fragment. Including the Hubbard term with small positive U_{eff} values, relatively more positive energy correction is provided for the structure with the linear U-O_h-H fragment than with a structure with a bent U-O_h-H fragment which effectively removes the bending mode barrier at θ(U-O_h-H) = 180°.

Similar to the second-order Jahn-Teller type interaction in the bare uranyl ion, the population of a δ_u-type U $5f$ quasi-atomic orbital affects the shape of the potential energy profiles of $[UO_2(OH)]^+$ along the U-O_h-H bending mode. In the linear uranyl ion, the two pertinent orbitals, $5f_{xyz}$ and $5f_{z(x^2-y^2)}$, are degenerate (of δ_u symmetry in the point group $D_{\infty h}$) and non-bonding. In the discussion of $[UO_2(OH)]^+$, we focus only on the orbital $f_{z(x^2-y^2)}$ because for the chosen orientation, this orbital can interact with the uranyl σ-like orbital. Both MOs transform as the a′ irreducible representation in the C_s point group.

The spurious stability of the linear configuration of U-O_h-H at the VWN level can be related to the fact that the π-type interaction between the hydroxyl $2p$ orbital and the uranyl σ-like MO which also contains a small contribution of the U $5f_{z(x^2-y^2)}$ orbital is more favored when the U-O_h-H framework is linear. Such an interaction results in a fractional population of the $5f_{z(x^2-y^2)}$ orbital for which the Coulomb repulsion energy is underestimated in the VWN approximation. By providing suitable energy corrections through the Hubbard term, at the VWN + U level, this linear U-O_h-H configuration is less favored (Figure 6.11). A related notable effect in the structural features of $[UO_2(OH)]^+$ is the prediction of a relatively short U-O_h bond length at the VWN and PBE levels, 199.1 pm and 202.1 pm, respectively. A short U-O_h bond with a linear configuration of U-O_h-H will lead to a stronger π-type interaction and an increased population of the U $5f_{z(x^2-y^2)}$-like orbital. Note that at the VWN + U and the PBE + U levels the U-O_h bond length increases with U_{eff}, reducing or preventing the π-type interaction.

Uranyl monohydroxide aqua complex

Next, the structure of the $[UO_2(OH)]^+$ moiety shall be discussed when additional aqua ligands are present in the complex $[UO_2(OH)(H_2O)_4]^+$. Geometry optimizations of the tetra aqua uranyl monohydroxide complex $[UO_2(OH)(H_2O)_4]^+$ were performed at the AE DKH PBE and AE DKH PBE + U levels. Table 6.14 summarizes the resulting parameters of the equilibrium geometry along with results from various methods such as B3LYP (this work, [171, 191]), AE ZORA PBE [186], AE ZORA BP86 [186], MP2 [187] and CCSD [187]. For the average

U-O_t bond length, AE DKH PBE calculation predicted a value of 180.1 pm which is close to the values obtained by ZORA-PBE [186] and ZORA-BP [186]. The introduction of the onsite Hubbard term with U_{eff} = 1.0 or 2.0 eV has the same effect as in the bare complex molecule $[UO_2(OH)]^+$, resulting in shortening of the U-O_t bond by 0.6 and 1.2 pm, respectively. The hybrid method B3LYP yields a slightly shorter bond length, a RECP/B3LYP calculation of this work gave 177.2 pm for r(U-O_t) which is close to the value calculated with MP2, 177.6 pm [187] while the CCSD method predicted a shorter bond length 175.1 pm [187].

Table 6.14: Geometry parameters of $[UO_2(OH)(H_2O)_4]^+$ [a] calculated from PBE and PBE + U calculations, compared to results from other methods: Average equilibrium U-O_t bond length $\bar{r}$ (U-O_t), average equilibrium U-O_w bond length $\bar{r}$ (U-O_w), equilibrium U-O_h bond length r (U-O_h), uranyl bond angle θ (O_t-U-O_t) and U-O_h-H bond angle θ (U-O_h-H). Bond lengths in pm and bond angles in degrees. Also given is the Hubbard parameter U_{eff} (eV) for the U $5f$ shell.

Method	U_{eff}	$\bar{r}$		r	θ	
		U-O_t	U-O_w	U-O_h	O_t-U-O_t	U-O_h-H
AE DKH PBE [b]		180.1	257	212.3	169.3	133.4
AE DKH PBE + U [b]	1.0	179.5	258	212.8	172.4	129.1
AE DKH PBE + U [b]	2.0	178.9	259	214.3	174.6	125.9
RECP/B3LYP [b]		177.2	259	210.2	173.5	137.5
AE ZORA PBE [c]		179.7	260	211.3		
AE ZORA BP86 [c]		180.0	259	211.6		
RECP/B3LYP [d]		178.3		216.2		
RECP/B3LYP [e]		178.6	258	215.5	166.7	
RECP/MP2 [f]		177.6	255-260	213.2		
RECP/CCSD [f]		175.1	254-259	214.4		

[a] Point group symmetry C_1.
[b] This work.
[c] Ref. [186]
[d] Ref. [171]
[e] Ref. [191]
[f] Ref. [187]

As in the case of $[UO_2(OH)]^+$, equatorial bonds are elongated when $U_{\text{eff}} > 0$. The AE DKH PBE value for the average r(U-O_w) is 257 pm; with U_{eff} = 1.0 and 2.0 eV, this distance is elongated by 1 pm and 2 pm, respectively. AE ZORA PBE [186] and AE ZORA BP [186] values are slightly longer by 3 pm and 2 pm, respectively, compared to the AE DKH PBE value. The RECP/B3LYP value of this work, 210 pm, differs from a previous results obtained with the same method, 216 pm, [171] indicating possible difference in the orientation of the equatorial

water molecules. The equatorial U-O_h bond is expected to be stronger and thus shorter than the U-O_w bond. The AE DKH PBE value for r(U-O_h) is 212.3 pm. With U_{eff} = 1.0 and 2.0 eV, r(U-O_h) increases by 0.5 pm and 2.0 pm, respectively, thus indicating a partial removal of U($5f$)-O_h($2p$) mixing as in the case of $[UO_2(OH)]^+$. As in the penta-aqua uranyl complex, the uranyl bond angle θ (O_t-U-O_t) is moderately affected by the Hubbard term. The AE DKH PBE value for the O_t-U-O_t bond angle is 169° which is similar to the B3LYP value 167° [171]. With U_{eff} = 1.0 eV and 2.0 eV, the uranyl moiety becomes less bent with θ (O_t-U-O_t) values 172 and 175°. The RECP/B3LYP value of the present work 174° is close to the PBE + U value for U_{eff} = 2.0 eV. In the ligand-free complex $[UO_2(OH)]^+$, the U-O_h-H bond angle changes notably with the introduction of the Hubbard term. This is no longer the case once the four aqua ligands are present in the complex $[UO_2(OH)(H_2O)_4]^+$. The AE DKH PBE value of the U-O_h-H bond angle is 133° which is decreased by 4° and 8° for U_{eff} values of 1.0 eV and 2.0 eV, respectively. Interestingly the B3LYP calculation of the present work predicted a structure where the U-O_h-H moiety is closer to the linear configuration than in the PBE calculation, by 5°.

6.3.2 Conclusions

The higher angular momentum of f orbitals provides greater flexibility for multi-directional orientation in directed valence bonding. Uranium $5f$ orbitals which are semi-localized play a vital role in the bonding of certain uranium complexes. An accurate description of their localization is necessary to properly describe the extent of intra-shell $5f$ - $5f$ hybridization, hence the contribution of various f orbitals to valence bonds. In the present work, a subtle competition between a π type and a σ-type interaction has been shown to govern the equilibrium geometry of the uranyl monohydroxide cation. Both these interactions involve the contribution of a δ-type U $5f$ quasi-atomic orbital. Incomplete self-interaction correction in KS-LDA and KS-GGA calculations resulted in uranyl monohydroxide geometries which differed from accurate predictions of CCSD(T) calculations. Also for this complex, the onsite Hubbard term with moderate values of the parameter U_{eff} provides approximate self-interaction correction and provides improved description for the structural aspects of uranyl monohydroxide.

Chapter 7

Summary and Outlook

The main objective of the present thesis was to adapt some commonly used variants of the DFT + U methodology for use with a localized basis set, to implement this method in the parallel density functional program PARAGAUSS, and to carry out molecular applications of systems with f electrons.

Within Kohn-Sham Density Functional Theory (KS-DFT), the electron-electron interaction energy is calculated as the sum of a classical Coulomb repulsion term and a contribution from the so-called exchange-correlation (XC) functional. An exact expression for the XC functional is not known, however approximations have been proposed to compute this term. The accuracy of a proper KS-DFT calculation depends on the approximation of the XC functional. Commonly used XC functionals that are based on the local density approximation (LDA) or the generalized gradient approximation (GGA) are considered as standard tools in computational quantum chemistry. The implicit efficiency of the KS-DFT approach along with the satisfactory accuracy of the LDA and GGA XC functionals ensures practical calculations of several physical properties for a wide range of systems such as atoms, molecules, clusters, polymers, systems with interfaces, etc.

While the formulation of KS-DFT allows an extension to systems with a fractional number of electrons, the description of fractional occupation numbers by approximate XC functionals has been identified as notable failures of LDA and GGA XC functionals. For a fractionally charged n-electron system, where $0 \leq n \leq 1$, and the electrons are of the same spin type, cancellation of the classical Coulomb contribution by the XC contribution both in the total energy and in the orbital energy is an exact condition which is to be satisfied by an exact XC functional. The failure to satisfy this condition results in a situation where an electron erroneously interacts with itself. In such a case the error introduced due to the inexact cancellation of the classical Coulomb and the XC contributions is called as the self-interaction error (SIE).

A number of remedial schemes have been proposed to provide corrections for the SIE present in LDA and GGA KS calculations. In solid state band structure calculations, in order to improve the LDA and GGA description of the $3d$ and $4f$ electrons of transition metal and lanthanide systems, the DFT + U methodology was proposed, where a shell-specific, Hubbard like energy correction term is added to the DFT total energy functional. Several variants of the DFT + U methodology have been suggested, among them the fully localized limit (FLL) approximation gives rise to a simple energy correction term which is aimed to improve the LDA and GGA description of systems with fractional occupation numbers of specified shells. The FLL DFT + U approach is commonly used in a simplified form where the magnitude of the energy correction is controlled by a single parameter U_{eff} (onsite-Coulomb parameter or the Hubbard parameter).

In the present work, the FLL DFT + U methodology has been set up for the first time for molecular systems and implemented in the program PARAGAUSS along with several variants of the onsite-occupation matrix in order to compute the orbital occupation numbers. The implementation was extended to analytic energy gradients to carry out geometry optimizations and, by numerically differentiating analytic forces, to compute the Hessian for calculating frequencies of harmonic vibrations. After implementation, test calculations were performed for model systems to understand the nature of corrections provided by the particular variant of the DFT + U approach and to evaluate the implementation.

As a first application of the DFT + U methodology to molecules, the role of $4f$ electrons in the bonding of LuF_3 was studied. A very recent study in the literature had classified their role as significant. Due to the poor shielding nature of f electrons, the completely filled $4f$ shell of Lu has a very small radial extension and was calculated not to be involved in covalent bonding with ligand orbitals. In LDA and GGA KS calculations, the SIE of orbital energies is maximal for integer occupation numbers which resulted in a severe destabilization of the $4f$ energy levels of Lu in LuF_3 and places the Lu $4f$ levels near the $2p$ levels of F. Such near degeneracy situations encountered in LDA and GGA calculations have been wrongly interpreted as bonding situations. To investigate this situation, several molecular properties such as dissociation energy, equilibrium geometry, etc. were calculated using the GGA-PBE method and the same quantities were computed at the corresponding DFT + U level. The magnitude of the onsite-Coulomb parameter U_{eff} = 18 eV, which was used in the DFT + U calculation was found by fitting the weighted center of the density of states (DOS) of the $4f$ shell of LuF_3 to the corresponding ionization potential (IP) obtained by photo-electron spectroscopy. By providing a suitable correction to the energies of the $4f$ levels, the near degeneracy between Lu $4f$ and F $2p$ levels was removed at the DFT + U level. However molecular properties of LuF_3 as computed at the DFT + U level were found to be essentially unaffected from their pure DFT values indicating that $4f$ electrons of Lu do not play

a role in the bonding of LuF_3.

As applications of the DFT + U methodology to $5f$ elements such as actinides, manifestations of SIE in the form of spurious structural distortions in LDA and GGA results of actinide complexes were studied. The uranyl molecular cation is an important species in the actinide chemistry, hence the bare uranyl ion and its complexes containing water and hydroxyl ligands formed suitable representative actinide systems for this purpose. In the present work, by empirical fitting, a meaningful value for U_{eff} for the $5f$ levels of the uranyl ion was determined to lie in the range of 1 to 2 eV. One of the key findings in the present work is the role of SIE on the uranyl bending mode frequency in LDA and GGA calculations. It was shown that a deviation of uranyl from linearity introduces intra-shell $5f$-$5f$ mixing that results in fractional occupation of previously unoccupied orbitals. Spurious stabilization of such fractional electrons in LDA and GGA calculations has been shown to be the reason for an underestimation of the bending mode frequency of uranyl. For the value of U_{eff} in the range 1 to 2 eV, the DFT + U methodology describes this frequency adequately in good agreement with the accurate and self-interaction free wavefunction based method CCSD(T).

The penta-aqua uranyl complex where the uranyl fragment in its equatorial plane is surrounded by five water ligands, has been predicted to have a structure of D_5 symmetric structure by hybrid-DFT methods such as B3LYP. However, KS-DFT calculations employing common LDA and GGA XC functionals predict a distorted structure for this molecule. This situation was investigated in the present work and it was shown that the soft uranyl bending mode along with a spurious near degenerate orbital interaction in LDA and GGA calculations is responsible for the structural distortion of penta-aqua uranyl. With U_{eff} between 1 to 2 eV, the DFT + U method was shown to improve the uranyl bending mode and to remove the spurious orbital interaction, resulting in a correct geometry for penta-aqua uranyl.

As a final application, the uranyl monohydroxide cation was studied. LDA and GGA methods predicted an equilibrium geometry which markedly deviates from the results of high level methods such as CCSD(T). In the present work, a wide range of calculations were performed to quantify the deviation of LDA and GGA results. From the analysis of the DFT results, the role of U $5f$ orbitals in the U-hydroxyl bonding has been identified which results in fractional occupation of non-bonding type U $5f$ orbitals that are spuriously stabilized in LDA and GGA calculations. In the DFT + U calculations, the same range of U_{eff} (1 to 2 eV) for the U $5f$ shell which was found to be appropriate for the bare uranyl ion and the corresponding penta aqua species is suitable for the uranyl monohydroxide cation to cancel approximately the SIE due to fractional populations of U $5f$ levels. With the inclusion of the U_{eff} parameter, both LDA and GGA descriptions of the structural properties of uranyl monohydroxide cation were improved

towards the results of more accurate methods such as hybrid-DFT and CCSD(T).

Overall, this thesis demonstrated the applicability of the DFT + U methodology to molecular systems and provided some guidelines to carry out further molecular applications of the DFT + U methodology. Besides the discussion of main results of the applications, various analyses were performed in this work to rationalize the corrections provided by the DFT + U method which in turn may aid in related investigations. An attractive feature of the DFT + U methodology is the inclusion of a tunable shell-specific correction term through which self-interaction artifacts introduced in LDA and GGA calculations can be easily identified and related to a specific atomic shell. Through a series of molecular applications, the DFT + U method has been shown to be a suitable probe tool when examining LDA and GGA results for self-interaction related artifacts in LDA and GGA calculations. An implementation of a scheme to calculate the U_{eff} parameter in an *ab-initio* fashion can certainly enhance the applicability of the current implementation of the DFT + U method in PARAGAUSS, however no unique procedure is available to accurately calculate this quantity. In this regard, the judiciously adjusted values of U_{eff}, as used in this work, may serve as suitable starting points for future DFT + U studies of related systems. Finally, the manifestation of SIE in various properties of lanthanide and actinide molecules as studied in the present work may also serve as test situations for newly developed XC functionals.

Appendix A

Basis sets

In this appendix some basic definitions related to the basis set framework of the program PARAGAUSS are given and the basis sets used in this work are described.

In the most general form, the atomic basis functions employed in the LCGTO framework of PARAGAUSS are defined as symmetry adapted linear combinations of contracted Gaussian type functions

$$^{\mathrm{SYM}}\mathbf{\Phi} = {}^{\mathrm{CONT}}\mathbf{\Phi}\,\mathbf{S}. \tag{A.1}$$

In the above equation, $^{\mathrm{CONT}}\mathbf{\Phi}$ is a *row* vector of contracted Gaussian type functions, $\mathbf{S}$ is a *transformation matrix* of symmetry adaption coefficients and $^{\mathrm{SYM}}\mathbf{\Phi}$ is a row of symmetry adapted basis functions. The contracted Gaussian functions are further expanded as linear combinations of *primitive* Gaussian functions as

$$^{\mathrm{CONT}}\mathbf{\Phi} = {}^{\mathrm{PRIM}}\mathbf{\Phi}\,\mathbf{C}, \tag{A.2}$$

where $^{\mathrm{PRIM}}\mathbf{\Phi}$ is a row vector of primitive Gaussian basis functions and the transformation matrix $\mathbf{C}$ is commonly known as the matrix of *contraction coefficients*. A single primitive Gaussian basis function is defined as the product of a Gaussian function of the form $\exp(-\alpha r^2)$, a real solid harmonic function $C_{l,m}$ and a normalization factor [93]. Thus the two main parameters that define a basis set used in a calculation are the set of *exponents* of the primitive Gaussian functions $\{\alpha_i\}$ and the corresponding contraction coefficients $\mathbf{C}$, both of which can be obtained from standard basis set libraries (e.g. [192]). When the matrix $\mathbf{C}$ is a unit matrix with its size equal to the number of primitive basis functions, the basis set is called an *uncontracted basis set*, symbolically represented as $(n_0 s,\ n_1 p,\ n_2 d,\ n_3 f)$ where n_0 is the number of s-type (angular momentum $l = 0$) primitive Gaussian functions and so on. On the other hand, an optimized set of fixed values for the columns of $\mathbf{C}$ is used to construct a *contracted basis set*, represented as $[N_0 s,\ N_1 p,\ N_2 d,\ N_3 f]$ where N_0 is the number of contracted functions that are linear combinations of s-type primitive functions ($l = 0$) and so on. Both contracted and uncontracted basis sets

were employed in the present work. For the lanthanide (La, Ce, Gd, Lu) and actinide (U) atoms, predominantly contracted basis sets were employed, where the columns of the matrix **C** were obtained from corresponding spin-restricted atomic calculations as eigenvectors of the Hamiltonian matrix. Specific details of these atomic calculations and the source of contraction coefficients of the basis sets of main group atoms such as H, C, O and F were discussed in Chapter 4. In the following, only the exponents of the primitive Gaussian functions of all the basis sets used in the present work are listed.

Further, an atomic orbital basis set is supplemented by an uncontracted auxiliary basis set which is used to fit the charge density [103]. The auxiliary basis set contains *s* and r^2 type fitting functions whose exponents were generated from those of *s* and *p* type orbital basis functions respectively by multiplying them by a factor of 2. From the auxiliary basis sets of La, Ce, Gd, Lu and U atoms, every second r^2 type function is removed to arrive at a smaller fit basis in order to decrease the near linear dependency and to improve the convergence. In addition, five primitive Gaussian basis functions of the type *p*, *d* and *f* were used as *polarization functions* whose exponents form the geometric sequence

$$\alpha_i = \zeta\beta^i, \quad i = 0,1,2,3,4. \tag{A.3}$$

For all three types (p, d, f) of polarization functions, the common ratio β is chosen as 2.5 and the pre factor ζ takes the values 0.1, 0.2 and 0.3 for *p*, *d* and *f* functions, respectively. In the following, the charge-fit basis set and the polarization functions are collectively represented as (n_0s, $n_1 r^2$, $m_1 p$, $m_2 d$, $m_3 f$). The set of exponents derived using the above equation are listed in the following table.

Exponents of polarization functions of the auxiliary basis set

	p	***d***	***f***
α_1	0.10000000	0.20000000	0.30000000
α_2	0.25000000	0.50000000	0.75000000
α_3	0.62500000	1.25000000	1.87500000
α_4	1.56250000	3.12500000	4.68750000
α_5	3.90625000	7.81250000	11.71875000

Hydrogen (Z = 1): (6*s*, 1*p*) basis set

Reference	[195, 196]
Contraction	(6*s*, 1*p*) → [4*s*, 1*p*]
Fit basis	(6*s*, 1r^2, 5*p*)

	s	***p***
α_1	0.08989100	1.00000000
α_2	0.25805300	
α_3	0.79767000	
α_4	2.82385400	
α_5	12.40955800	
α_6	82.63637400	

Hydrogen (Z = 1): (8*s*, 4*p*, 3*d*) basis set

Reference	[194]
Contraction	(8*s*, 4*p*, 3*d*) → [4*s*, 3*p* 2*d*]
Fit basis	(8*s*, 4r^2, 5*p*, 5*d*)

	s	***p***	***d***
α_1	0.02796200	0.09882700	0.29104000
α_2	0.07989100	0.28236200	0.72760000
α_3	0.21214900	0.80675000	1.81900000
α_4	0.59106300	2.30500000	
α_5	1.81504100		
α_6	6.42483000		
α_7	28.27659600		
α_8	188.61445000		

Carbon (Z = 6): (14*s*, 9*p*, 4*d*, 3*f*) basis set

Reference	[194]
Contraction	$(14s, 9p, 4d, 3f) \rightarrow [5s, 4p, 3d, 2f]$
Fit basis	$(14s, 9r^2, 5p, 5d)$

	s	*p*	*d*	*f*
α_1	0.03468000	0.02290000	0.08146300	0.20000000
α_2	0.09908700	0.06542900	0.23275000	0.50000000
α_3	0.24606800	0.15474000	0.66500000	1.25000000
α_4	0.61301300	0.36194400	1.90000000	
α_5	1.54711800	0.86515000		
α_6	3.57701500	2.17931700		
α_7	8.38397600	6.08036500		
α_8	20.65931100	19.55761100		
α_9	53.91874600	83.33315500		
α_{10}	151.71075000			
α_{11}	472.82279000			
α_{12}	1694.32760000			
α_{13}	7524.78560000			
α_{14}	50557.50100000			

Oxygen (Z = 8): (9*s*, 5*p*, 1*d*) basis set

Reference	[195, 196]
Contraction	$(9s, 5p, 1d) \rightarrow [5s, 4p, 1d]$
Fit basis	$(9s, 5r^2, 5p, 5d)$

	s	*p*	*d*
α_1	0.30068600	0.21488200	1.15000000
α_2	1.00427100	0.72316400	
α_3	4.75680300	2.30869000	
α_4	12.28746900	7.84313100	
α_5	33.90580900	34.85646300	
α_6	103.65179300		
α_7	364.72525700		
α_8	1599.70968900		
α_9	10662.28494000		

Fluorine (Z = 9): (14*s*, 9*p*, 4*d*, 3*f*) basis set

Reference	[194]
Contraction	(14*s*, 9*p*, 4*d*, 3*f*) $\rightarrow$ [5*s*, 4*p*, 3*d*, 2*f*]
Fit basis	(14*s*, 9r^2, 5*p*, 5*d*)

	s	***p***	***d***	***f***
α_1	0.08430100	0.05418400	0.21437500	0.51200000
α_2	0.24086100	0.15481000	0.61250000	1.28000000
α_3	0.62329000	0.40397300	1.75000000	3.20000000
α_4	1.56815700	0.99506000	5.00000000	
α_5	3.91940100	2.44703000		
α_6	8.53274300	6.27499500		
α_7	18.94287400	17.60456800		
α_8	44.64472700	56.91900500		
α_9	113.44230000	245.33029000		
α_{10}	314.03534000			
α_{11}	967.09483000			
α_{12}	3441.53920000			
α_{13}	15281.00700000			
α_{14}	103109.46000000			

Lanthanum (Z = 57): (24*s*, 21*p*, 15*d*, 5*f*) basis set

Reference	[126]
Contraction	(24*s*, 21*p*, 15*d*, 5*f*) $\rightarrow$ [9*s*, 8*p*, 6*d*, 4*f*]
Fit basis	(24*s*, 11r^2, 5*p*, 5*d*, 5*f*)

	s	***p***	***d***	***f***
α_1	0.01471267	0.02112952	0.03130637	0.10225200
α_2	0.03678167	0.05282379	0.07826592	0.24057400
α_3	0.09195418	0.13205949	0.22988546	0.60143500
α_4	0.22988546	0.33014872	0.56974097	1.50358800
α_5	0.56974097	0.82537179	1.42250633	5.93867800
α_6	1.42250633	1.96206638	3.07135819	
α_7	3.07135819	4.04845718	6.41189459	
α_8	6.41189459	8.31512573	13.16322130	
α_9	13.16322130	16.24070830	26.69874160	
α_{10}	26.69874160	32.08192270	55.06898320	
α_{11}	55.06898320	64.74048750	115.66963400	
α_{12}	115.66963400	130.90304300	251.40762400	
α_{13}	251.40762400	272.99883700	564.23215000	
α_{14}	564.23215000	595.55617800	1293.69218000	
α_{15}	1293.69218000	1383.57034000	3073.74453000	
α_{16}	3073.74453000	3496.48341000		
α_{17}	7611.63314000	9868.88138000		
α_{18}	19800.65040000	32036.71700000		
α_{19}	54741.68130000	123114.08400000		
α_{20}	162993.86400000	585217.19200000		
α_{21}	530660.67500000	3947501.17000000		
α_{22}	1933165.17000000			
α_{23}	8123190.06000000			
α_{24}	44334794.20000000			

Cerium (Z = 58): (25*s*, 22*p*, 15*d*, 11*f*) basis set

Reference	[126]
Contraction	(25*s*, 22*p*, 15*d*, 11*f*) → [9*s*, 8*p*, 6*d*, 4*f*]
Fit basis	(25*s*, 11r^2, 5*p*, 5*d*, 5*f*)

	s	***p***	***d***	***f***
α_1	0.00460118	0.00780792	0.03216400	0.05035943
α_2	0.01150450	0.01951979	0.08040999	0.12589859
α_3	0.02876124	0.04879948	0.23792043	0.31474648
α_4	0.08040999	0.12199870	0.59320372	0.72992149
α_5	0.23792043	0.31474648	1.49142031	1.62215185
α_6	0.59320372	0.72992149	3.22291959	3.39735340
α_7	1.49142031	1.62215185	6.72376354	6.94695462
α_8	3.22291959	3.39735340	13.79309700	14.06409730
α_9	6.72376354	6.94695462	27.94987250	28.05662940
α_{10}	13.79309700	14.06409730	57.62530360	57.77760050
α_{11}	27.94987250	28.05662940	121.07176300	117.58398400
α_{12}	57.62530360	57.77760050	263.32783200	
α_{13}	121.07176300	117.58398400	591.15964500	
α_{14}	263.32783200	245.86049300	1356.51771000	
α_{15}	591.15964500	536.78966500	3225.20602000	
α_{16}	1356.51771000	1245.36053000		
α_{17}	3225.20602000	3139.55221000		
α_{18}	7989.27326000	8834.96472000		
α_{19}	20779.25380000	28617.52420000		
α_{20}	57400.92380000	109980.94900000		
α_{21}	170633.49100000	524129.96600000		
α_{22}	553938.14100000	3555062.42000000		
α_{23}	2008484.48000000			
α_{24}	8375256.96000000			
α_{25}	45191317.30000000			

Gadolinium (Z = 64): (25*s*, 22*p*, 15*d*, 11*f*) basis set

Reference	[126]
Contraction	(25*s*, 22*p*, 15*d*, 11*f*) $\rightarrow$ [9*s*, 8*p*, 6*d*, 4*f*]
Fit basis	(25*s*, 11r^2, 5*p*, 5*d*, 5*f*)

	s	***p***	***d***	***f***
α_1	0.00505301	0.00882074	0.03509922	0.06079557
α_2	0.01263252	0.02205186	0.08774806	0.15198894
α_3	0.03158129	0.05512964	0.27354766	0.37997236
α_4	0.08774806	0.13782410	0.71264801	0.93074707
α_5	0.27354766	0.37997236	1.87459311	2.11418525
α_6	0.71264801	0.93074707	4.08926005	4.57627292
α_7	1.87459311	2.11418525	8.54173610	9.59867792
α_8	4.08926005	4.57627292	17.50432520	19.55546590
α_9	8.54173610	9.59867792	35.27192760	39.64806710
α_{10}	17.50432520	19.55546590	72.46670040	82.64890640
α_{11}	35.27192760	39.64806710	152.32953700	172.14364000
α_{12}	72.46670040	82.64890640	332.00042000	
α_{13}	152.32953700	172.14364000	747.42556100	
α_{14}	332.00042000	369.02563500	1722.31277000	
α_{15}	747.42556100	825.68844400	4108.48885000	
α_{16}	1722.31277000	1967.87734000		
α_{17}	4108.48885000	5114.02661000		
α_{18}	10186.06230000	14859.12410000		
α_{19}	26421.00080000	49379.84090000		
α_{20}	72467.75250000	191924.14100000		
α_{21}	212690.70200000	909355.73100000		
α_{22}	676377.58500000	5979841.01000000		
α_{23}	2377757.08000000			
α_{24}	9460580.02000000			
α_{25}	47757955.70000000			

Lutetium (Z = 71): (25*s*, 22*p*, 15*d*, 11*f*) basis set

Reference	[126]
Contraction	(25*s*, 22*p*, 15*d*, 11*f*) → [9*s*, 8*p*, 6*d*, 4*f*]
Fit basis	(25*s*, 11r^2, 5*p*, 5*d*, 5*f*)

	s	***p***	***d***	***f***
α_1	0.00865860	0.01232352	0.03641605	0.07567004
α_2	0.02164651	0.03080881	0.09104013	0.18917511
α_3	0.05411628	0.07702204	0.30639930	0.47293779
α_4	0.13529071	0.19255512	0.84556697	1.20346956
α_5	0.33822678	0.48138782	2.33020702	2.80208130
α_6	0.84556697	1.20346956	5.14340016	6.16841114
α_7	2.33020702	2.80208130	10.80010080	13.06410770
α_8	5.14340016	6.16841114	22.18571600	26.84545200
α_9	10.80010080	13.06410770	44.55784090	55.11789140
α_{10}	22.18571600	26.84545200	91.35523090	115.62095300
α_{11}	44.55784090	55.11789140	192.40395900	245.16436500
α_{12}	91.35523090	115.62095300	420.73427400	
α_{13}	192.40395900	245.16436500	952.02267900	
α_{14}	420.73427400	536.92927300	2206.33627000	
α_{15}	952.02267900	1229.96307000	5285.35528000	
α_{16}	2206.33627000	3009.97919000		
α_{17}	5285.35528000	8048.21054000		
α_{18}	13115.78600000	23994.79600000		
α_{19}	33896.72310000	80964.26030000		
α_{20}	92147.91420000	314764.31600000		
α_{21}	266370.53700000	1466437.56000000		
α_{22}	827289.33400000	9206720.28000000		
α_{23}	2810703.63000000			
α_{24}	10641810.10000000			
α_{25}	50315163.60000000			

Uranium (Z = 92): (24*s*, 19*p*, 16*d*, 11*f*) basis set

Reference	[193]
Contraction	(24*s*, 19*p*, 16*d*, 11*f*) $\rightarrow$ [10*s*, 7*p*, 7*d*, 4*f*]
Fit basis	(24*s*, 9r^2, 5*p*, 5*d*, 5*f*)

	s	***p***	***d***	***f***
α_1	0.02058815	0.1579066	0.03447413	0.1103255
α_2	0.04313320	0.4089979	0.08774074	0.3025422
α_3	0.08254175	0.9059122	0.21542030	0.7374815
α_4	0.31243190	2.2913760	0.51211640	1.6923540
α_5	0.65236340	4.6491100	1.20507700	3.7526650
α_6	1.85772200	11.1375800	2.55673600	8.1734170
α_7	3.33603700	22.8575700	5.22965900	17.5173600
α_8	8.81990900	52.7374700	10.89752000	38.2236500
α_9	15.37485000	113.7117000	22.23856000	86.8443800
α_{10}	37.71001000	270.7284000	45.78370000	219.0811000
α_{11}	69.22380000	649.7508000	94.63173000	703.2615000
α_{12}	172.98510000	1673.8100000	205.18560000	
α_{13}	370.13750000	4676.7450000	474.04020000	
α_{14}	849.55400000	14437.8400000	1215.79900000	
α_{15}	1981.83800000	50135.6100000	3707.24200000	
α_{16}	4869.81100000	200185.0000000	16079.47000000	
α_{17}	12511.46000000	948314.4000000		
α_{18}	33651.45000000	5589055.0000000		
α_{19}	95179.62000000	30062560.0000000		
α_{20}	285123.90000000			
α_{21}	912190.10000000			
α_{22}	3147013.00000000			
α_{23}	12113820.00000000			
α_{24}	48171220.00000000			

Bibliography

[1] J.C. Slater, The Calculation of Molecular Orbitals, John Wiley & Sons, USA (1979).

[2] D.R. Hartree, The Calculation of Atomic Structures, John Wiley & Sons, New York (1957).

[3] N.H. March, in: S. Lundqvist, N.H. March (Eds.), Theory of Inhomogeneous Electron Gas, Plenum Press, New York (1963), pp. 1-78.

[4] F.L. Hirschfeld, in: A. Domenicano, I. Hargittai (Eds.), Accurate Molecular Structures: Their Determination and Importance, Oxford University Press, USA (1992), pp.238-269.

[5] E. Schrödinger, Ann. Phys. **386**, 109 (1926).

[6] R.F.W. Bader, J. Mol. Struct. (THEOCHEM) **943**, 2 (2010).

[7] N.H. March, Electron Density Theory of Atoms and Molecules, Academic Press (1992).

[8] R.G. Parr, W. Yang, Density Functional Theory of Atoms and Molecules, Oxford University Press, New York (1989).

[9] P. Hohenberg, W. Kohn, Phys. Rev. **136**, B864 (1964).

[10] W. Koch, M.C. Holthausen, A Chemist's Guide to Density Functional Theory, Wiley-VCH Verlag, Weinheim (2001).

[11] R.D. Morgan III, in: G.F.W. Drake (Ed.), Springer Handbook of Atomic, Molecular, and Optical Physics, Volume 1, Springer, Heidelberg (2006), pp. 295-306.

[12] W. Kohn, L.J. Sham, Phys. Rev. **140**, A1133 (1965).

[13] N.C. Handy, in: B.O. Roos (Ed.), Lecture Notes in Quantum Chemistry: European Summer School in Quantum Chemistry, vol. II, Springer, Berlin (1994), pp. 91-124.

[14] A.J. Cohen, P. Mori-Sanchez, W.T. Yang, Science **321**, 792 (2008).

[15] J.P. Perdew, A. Zunger, Phys. Rev. B **23**, 5048 (1981).

[16] J.P. Perdew, A. Ruzsinszky, Int. J. Quantum Chem. **110**, 2801 (2010).

[17] D.S. Sholl, J.A. Steckel, Density Functional Theory, A Practical Introduction, John Wiley & Sons, New Jersey (2009).

[18] C. Morgado, M.A. Vincent, I.H. Hillier, X. Shan, Phys. Chem. Chem. Phys. **9**, 448 (2009).

[19] S. Grimme, J. Comp. Chem. **12**, 1462 (2004).

[20] V.I. Anisimov, J. Zaanen, O.K. Andersen, Phys. Rev. B **44**, 943 (1991).

[21] T. Belling, T. Grauschopf, S. Krüger, F. Nörtemann, M. Staufer, M. Mayer, V.A. Nasluzov, U. Birkenheuer, A. Hu, A. Matveev, A.V. Shor, M. Fuchs-Rohr, K.M. Neyman, D.I. Ganyushin, T. Kerdcharoen, A. Woiterski, S. Majumder, N. Rösch, PARAGAUSS Version 3.1, Technische Universität München (2006).

[22] Th. Belling, T. Grauschopf, S. Krüger, M. Mayer, F. Nörtemann, M. Staufer, C. Zenger, N. Rösch, in: H.-J. Bungartz, F. Durst, C. Zenger (Eds.), High Performance Scientific and Engineering Computing, Lecture Notes in Computational Science and Engineering, vol. 8, Springer, Heidelberg (1999) p. 439.

[23] A.V. Matveev, M. Mayer, N. Rösch, Comp. Phys. Comm. **160**, 91 (2004).

[24] N. Rösch, A.V. Matveev, V.A. Nasluzov, K.M. Neyman, L.V, Moskaleva, S. Krüger, in: P. Schwerdtfeger (Ed.) Relativistic Electronic Structure Theory - Applications, Theoretical and Computational Chemistry Series, Vol. 14, Elsevier, Amsterdam, 2004, pp.656-722.

[25] R. Ramakrishnan, A.V. Matveev, N. Rösch, Chem. Phys. Lett. **468**, 158 (2009).

[26] R. Ramakrishnan, A.V. Matveev, N. Rösch, Comput. Theoret. Chem. **963**, 337 (2011).

[27] R. Ramakrishnan, A.V. Matveev, S. Krüger, N. Rösch, in preparation.

[28] R.A. Evarestov, Quantum Chemistry of Solids: The LCAO First Principles Treatment of Crystals, Springer, Heidelberg (2007).

[29] C. Fiolhais, F. Nogueira, M.A.L. Marques (Eds.), A Primer in Density Functional Theory, Springer, Heidelberg (2003).

[30] J.M. Seminario (Ed.), Recent Developments and Applications of Modern Density Functional Theory, Elsevier, Amsterdam (1996).

[31] L.H. Thomas, Proc. Cambridge Phil. Soc. **23**, 542 (1927).

[32] E. Fermi, Rend. Accad. Naz. Lincei **6**, 602 (1927).

[33] E. Teller, Rev. Mod. Phys. **34**, 627 (1962).

[34] C.F.v. Weizsäcker, Zeitschrift für Physik **96**, 431 (1935).

[35] A. Wang, E.A. Carter, in: S.D. Schwartz (Eds.), Theoretical Methods in Condensed Phase Chemistry. Springer, New York (2002), p. 117-184.

[36] W. Kohn, P. Vashishta, in: S. Lundqvist, N.H. March (Eds.), Theory of Inhomogeneous Electron Gas, Plenum Press, New York (1963), pp. 79-147.

[37] J.C. Slater, Phys. Rev. **81**, 285 (1951).

[38] P.A.M. Dirac, Proc. Cambridge Phil. Soc. **26**, 376 (1930).

[39] J.W.D. Connolly, in: G.A. Segal (Ed.), Semiempirical Methods of Electronic Structure Calculations, Part A: Techniques, Plenum Press, New York (1977), pp. 102-132.

[40] S.H. Vosko, L. Wilk, M. Nusair, Can. J. Phys. **58**, 1200 (1980).

[41] D.M. Ceperley, B.J. Alder, Phys. Rev. Lett. **45**, 566 (1980).

[42] J.P. Perdew, Y. Wang, Phys. Rev. B **45**, 13244 (1992).

[43] A.D. Becke, Phys. Rev. A **38**, 3098 (1988).

[44] J.P. Perdew, Phys. Rev. B **33**, 8822 (1986).

[45] J.P. Perdew, J.A. Chevary, S.H. Vosko, K.A. Jackson, M.R. Pederson, D.J. Singh, C. Fiolhais, Phys. Rev. B **46**, 6671 (1992).

[46] J.P. Perdew, K. Burke, M. Ernzerhof, Phys. Rev. Lett. **77**, 3865 (1996).

[47] B. Hammer, L.B. Hansen, J.K. Nørskov, Phys. Rev. B **59**, 7413 (1999).

[48] J.M. Tao, J.P. Perdew, V.N. Staroverov, G.E. Scuseria, Phys. Rev. Lett. **91**, 146401 (2003).

[49] A.D. Becke, J. Chem. Phys. **98**, 5648 (1993).

[50] C. Lee, W. Yang, R.G. Parr, Phys. Rev. B **37**, 785 (1988).

[51] P.J. Stephens, F.J. Devlin, C.F. Chabalowski, M.J. Frisch, J. Phys. Chem. **98**, 11623 (1994).

[52] C. Adamo, V. Barone, J. Chem. Phys. **110**, 6158 (1999).

[53] D. Bohm, D. Pines, Phys. Rev. **92**, 609 (1953).

[54] J.P. Perdew, K. Schmidt, in: V.E. Van Doren, K. Van Alsenoym, K. Geerlings (Eds.), Density Functional Theory and Its Applications to Materials, AIP, New York (2001) p.1

[55] A. Szabo, N.S. Ostlund, Modern Quantum Chemistry, Introduction to Advanced Electronic Structure Theory, Dover, New York (1982).

[56] N. Rösch, in: P. Phariseau, L. Scheire (Eds.), Electrons in Finite and Infinite Systems, NATO Advanced Study Institute, Series B, Vol. 24, Plenum Press, New York (1977) pp. 1-143.

[57] J.P. Perdew, in: J. Keller and J.L. Gazquez (Eds.), Density Functional Theory, Lecture Notes in Physics, Vol. 187, Spinger, Heidelberg (1983) pp. 127-165.

[58] L. Pauling, E.B. Wilson, Introduction to Quantum Mechanics, Dover, USA (1935) pp. 446-447.

[59] J.P. Perdew, R.G. Parr, M. Levy, J.L. Balduz, Phys. Rev. Lett. **49**, 1691 (1982).

[60] N.D. Mermin, Phys. Rev. **137**, A1141 (1965).

[61] Ya.I. Delchev, A.I. Kuleff, J.Maruani, Tz.Mineva, F. Zahariev, in: J.-P. Julien, J. Maruani, D. Mayou, S. Wilson, G. Delgado-Barrio (Eds.), Recent Advances in the Theory of Chemical and Physical Systems, Progress in Theoretical Chemistry and Physics, Vol. 15, Springer, Dordrecht (2006), pp. 159-176.

[62] Y. Zhang, W. Yang, J. Chem. Phys. **109**, 2604 (1998).

[63] Y. Zhang, W. Yang, Theor. Chem. Acc. **103**, 346 (2000).

[64] A.J. Cohen, P. Mori-Sánchez, W. Yang, Psi-K Newsletter **99**, 24 (2010).

[65] T. Koopmans, Physica **1**, 104 (1934).

[66] J.F. Janak, Phys. Rev. B **18**, 7165 (1978).

[67] H. Chermette1, I. Ciofini, F. Mariotti, C. Daul, J. Chem. Phys. **114**, 1447 (2001).

[68] O.A. Vydrov, G.E. Scuseria, J. Chem. Phys. **121**, 8187 (2004).

[69] S. Kümmel, J.P. Perdew, Phys. Rev. B **68**, 035103 (2003).

[70] V. Anisimov, Y. Izyumov, Electronic Structure of Strongly Correlated Materials, Springer, Heidelberg (2010).

[71] A. Altland, B. Simons, Condensed Matter Field Theory, Cambridge University Press, Cambridge (2010), Chapter 2.

[72] P.R. Surján, Second Quantized Approach to Quantum Chemistry, Springer-Verlag, Heidelber (1989), Chapter 10.

[73] A.B. Shick, A.I. Liechtenstein, W.E. Pickett, Phys. Rev. B **60**, 10763 (1999).

[74] O. Bengone, M. Alouani, P. Blochl, J. Hugel, Phys. Rev. B **62**, 16392 (2000).

[75] F. Zhou, M.Cococcioni, C.A. Marianetti, D. Morgan, G. Ceder, Phys. Rev. B **70**, 235121 (2004).

[76] H. Eschrig, K. Koepernik, I. Chaplygin, J. Solid State Chem. **176**, 482 (2003).

[77] M.J. Han, T. Ozaki, J. Yu, Phys. Rev. B **73**, 045110 (2006).

[78] A.I. Liechtenstein, V.I. Anisimov, J. Zaane, Phys. Rev. B **52**, R5467 (1995).

[79] E.R. Ylvisaker, W.E. Pickett, K. Koepernik, Phys. Rev. B **79**, 035103 (2009).

[80] S.L. Dudarev, G.A. Botton, S.Y. Savrasov, C.J. Humphreys, A.P. Sutton, Phys. Rev. B **57**, 1505 (1998).

[81] D. Seo, Phys. Rev. B **76**, 033102 (2007).

[82] R.C. Dorca, Adv. Quant. Chem. **49**, 121 (2005).

[83] W.E. Pickett, S.C. Erwin, E.C. Ethridge, Phys. Rev. B **58**, 1201 (1998).

[84] A.E. Reed, R.B. Weinstock, F. Weinhold, J. Chem. Phys. **83**, 735 (1985).

[85] H. Eschrig, K. Koepernik, I. Chaplygin, J. Solid State Chem. **176**, 482 (2003).

[86] J.M. Herbert, J.E. Harriman, Chem. Phys. Lett. **382**, 142 (2003).

[87] P. Pou, R. Oswaldowski, H. Vaquez, R. Perez, F. Flores, J. Ortega, Int. J. Quantum Chem. **91**, 151 (2003).

[88] R. Oszwaldowski, H. Vaquez, P. Pou, J. Ortega, R. Perez, J. Phys.: Condens. Matter **15**, S2665 (2003).

[89] M. Staufer, A Parallel Implementation of the Density Functional Method: Analytical Energy Gradients, DF Quadrature and Applications to Chemisorption, Dissertation, Technische Universität München (1999).

[90] V.A. Nasluzov, N. Rösch. Chem. Phys. Lett. **210**, 413 (1996).

[91] M. Filatov, D. Cremer, Chem. Phys. Lett. **370**, 647 (2003).

[92] M. Filatov, D. Cremer, J. Chem. Phys. **118**, 6741 (2003).

[93] T. Belling, A Parallel Implementation of the Density Functional Method: Integral Evaluation and External Potentials, Application to Thiolate Adsorption on Gold Surfaces, Dissertation, Technische Universität München (1998).

[94] A.G. Petukhov, I.I. Mazin, L. Chioncel, A.I. Lichtenstein, Phys. Rev. B **67**, 153106 (2003).

[95] N.J. Mosey, E.A. Carter, Phys. Rev. B **76**, 155123 (2007).

[96] N.J. Mosey, P. Liao, E.A. Carter, J. Chem. Phys. **129**, 014103 (2008).

[97] A. Rohrbach, J. Hafner, G. Kresse, Phys. Rev. B **70**, 125426 (2004).

[98] O. Bengone, M. Alouani, P. Blöchl, J. Hugel, Phys. Rev. B **62**, 16392 (2000).

[99] B. Judd, Operator Techniques in Atomic Spectroscopy, McGraw-Hill, New York (1963).

[100] V.I. Anisimov, O. Gunnarsson, Phys. Rev. B **43**, 7570 (1991).

[101] M. Cococcioni, S. de Gironcoli, Phys. Rev. B **71**, 035105 (2005).

[102] H.J. Kulik, M. Cococcioni, D.A. Scherlis, N. Marzari, Phys. Rev. Lett. 97, 103001 (2006).

[103] B.I. Dunlap, N. Rösch, Adv. Quant. Chem. **21**, 317 (1990).

[104] NIST Atomic Spectra Database,
http://www.nist.gov/pml/data/asd.cfm

[105] B. Ruščić, G.L. Goodman, J. Berkowitz, J. Chem. Phys. **78**, 5443 (1983).

[106] R. Laskowski, G.K.H. Madsen, P. Blaha, K. Schwarz, Phys. Rev. B **69**, 104408 (2004).

[107] A.N. Yaresko, V.N. Antonov, P. Fulde, Phys. Rev. B **67**, 155103 (2003).

[108] J. Han, V. Goncharov, L.A. Kaledin, A.V. Komissarov, M.C. Heaven, J. Chem. Phys. **120**, 5155 (2004).

[109] J.K. Gibson, R.G. Haire, J. Marcalo, M. Santos, J.P. Leal, A.P. de Matos, R. Tyagi, M.K. Mrozik, R.M. Pitzer, B.E. Bursten, Eur. Phys. J. D **45**, 133 (2007).

[110] B. Johansson, in: P.A. Sterne, A. Gonis, A.A. Borovoi (Eds.), Actinides and the Environment: NATO ASI Series, Kluwer, Netherlands (1998) pp. 47-96.

[111] S. Cotton, Lanthanide and Actinide Chemistry, John Wiley & Sons, West Sussex (2006).

[112] P. Pyykko, Chem. Rev. **88**, 563 (1988).

[113] M.S. Banna, J. Chem. Educ. **62**, 197 (1985).

[114] M. Seth, M. Dolg, P. Fulde, P. Schwerdtfeger, J. Am. Chem. Soc. **117**, 6597 (1995).

[115] M. Dolg, H. Stoll, in: K.A. Gschneider, L. Eyring (Eds.), Handbook of Chemistry and Physics of Rare Earths, vol. 22, Elsevier, Amsterdam (1996) pp. 607-729.

[116] M. Hargittai, Coord. Chem. Rev. **91**, 35 (1988).

[117] M. Hargittai, Chem. Rev. **100**, 2233 (2000).

[118] A. Kovács, R.J.M. Konings, J. Phys. Chem. Ref. Data **33**, 377 (2004).

[119] J.C. Culberson, P. Knappe, N. Rösch, M.C. Zerner, Theor. Chim. Acta **71**, 21 (1987).

[120] C. Adamo, V. Barone, J. Comp. Chem. **76**, 1153 (2000).

[121] C. Adamo, P. Maldivi, Chem. Phys. Lett. **268**, 61 (1997).

[122] V. Vetere, C. Adamo, P. Maldivi, Chem. Phys. Lett. **325**, 99 (2000).

[123] C. Clavaguéra, J.P. Dognan, P. Pyykkö, Chem. Phys. Lett. **429**, 8 (2006).

[124] M. Dolg, H. Stoll, H. Preuss, J. Mol. Struct. (THEOCHEM) **235**, 67 (1991).

[125] G. Lanza, C. Minichino, J. Phys. Chem. A **109**, 2127 (2005).

[126] B.O. Roos, R. Lindh, P.-Å. Malmqvist, V. Veryazoc, P.-O. Widmark, A.C. Borin, J. Phys. Chem. A **112**, 11431 (2008).

[127] O. Kahn, Molecular Magnetism, Wiley-VCH, Newyork (1993), Chapter 3.

[128] J. Molnar, M. Hargittai, J. Phys. Chem. **99**, 10780 (1995).

[129] C.E. Myers, Inorg. Chem. **14**, 199 (1975).

[130] C.E. Myers, L.J. Norman II, L.M. Leow, Inorg. Chem. **17**, 1581 (1978).

[131] Y. Zhang, W. Yang, J. Chem. Phys. **109**, 2604 (1998).

[132] A. Görling, S.B. Trickey, P. Gisdakis, N. Rösch, in: J. Brown, P. Hoffman (Eds.), Topics in Organometallic Chemistry, vol. 4, Springer, Heidelberg (1999) p. 109.

[133] N. Rösch, S.B. Trickey, J. Chem. Phys. **106**, 8940 (1997).

[134] P.A. Chrstiansen, W.C. Ermler, K.S. Pitzer, Ann. Rev. Phys. Chem. **36**, 407 (1985).

[135] M. Dolg, W. Liu, S. Kolvoda, Int. J. Quantum Chem. **76**, 359 (2000).

[136] L. Perrin, L. Maron, O. Eisenstein, Faraday Discuss. **124**, 25 (2003).

[137] L. Joubert, G. Picard, J.J. Legendre, Inorg. Chem. **37**, 1984 (1988).

[138] G. Frenking, N. Fröhlich, Chem. Rev. **100**, 717 (2000).

[139] T.A. Albright, J.K. Burdett, M. Whangbo, Orbital Interactions in Chemistry, Wiley-Interscience (1985).

[140] J.K. Burdett, Chemical Bonds: A Dialog, Wiley (1997).

[141] T.A. Albright, J.K. Burdett, Problems in Molecular Orbital Theory, Oxford University Press, USA (1992).

[142] C. Fua, T. Lia, J. Qia, J. Pana, S. Chena, C. Chenga, Chem. Phys. Lett. **494**, 117 (2010).

[143] C. Zhang, A. Michaelidesa, S.J. Jenkinsb, Phys. Chem. Chem. Phys. **13**, 23 (2011).

[144] C. Zhang, A. Michaelides, D.A. King, S.J. Jenkins, J. Chem. Phys. **129**, 194708 (2008).

[145] C. Zhang, A. Michaelides, D.A. King, S.J. Jenkins, Phys. Rev. **79**, 075433 (2009).

[146] F. Esch, S. Fabris, L. Zhou, T. Montini, C. Africh, P. Fornasiero, G. Comelli, R. Rosei, Science, **309**, 752 (2005).

[147] G. Meyer, L.R. Morss, Synthesis of Lanthanide and Actinide Compounds, Springer, Heidelberg (1990).

[148] Didier Astruc, Nanoparticles and Catalysis, Wiley-VCH (2007).

[149] C. Loschen, S.T. Bromley, K.M. Neyman, F. Illas, J. Phys. Chem. **111**, 10142 (2007).

[150] F. Zhang, Q. Jin, S. Chan, J. Applied. Phys. **95**, 4319 (2004).

[151] M.M. Branda, N.J. Castellani, R. Grau-Crespo, M.H. de Leeuw, N.C. Hernendez, J.F. Sanz, K.M. Neyman, F. Illas, J. Chem. Phys. **131**, 094702 (2009).

[152] A. Harju, E. Räsänen, H. Saarikoski, M.J. Puska, R.M. Nieminen, K. Niemela, Phys. Rev. B **69**, 153101 (2004).

[153] E.A.A. Noha, J. Zhang, Chem. Phys. **330**, 82 (2006).

[154] K. Tatsumi, R. Hoffmann, Inorg. Chem. **19**, 2656 (1980).

[155] V.E. Jackson, R. Craciun, D.A. Dixon, K.A. Peterson, W.A. de Jong, J. Phys. Chem. A **112**, 4095 (2008).

[156] R.G. Denning, in: Structure and Bonding, vol. 79, Springer-Verlag, Berlin (1992), pp.217-276.

[157] R.L. Dekock, E.J. Baerends, P.M. Boerrigter, J.G. Snijders, Chem. Phys. Lett. **105**, 308 (1984).

[158] C. Jörgensen, Chem. Phys. Lett. **89**, 455 (1982).

[159] W.R. Wadt, J. Am. Chem. Soc. **103**, 6053 (1981).

[160] P. Pyykkö, L. Laaksonen, J. Phys. Chem. **88**, 4892 (1984).

[161] P. Pyykkö, J. Li, N. Runeberg, J. Phys. Chem. **98**, 4809 (1994).

[162] R.G. Denning, J. Phys. Chem. A **111**, 4125 (2007).

[163] X. Cao, M. Dolg, in: M. Baryszm, Y. Ishikawa (Eds.), Relativistic methods for chemists, Springer, UK (2010), pp.215-278.

[164] A.V. Matveev, N. Rösch, J. Chem. Phys. **128**, 244102 (2008).

[165] H.A. Jahn, E. Teller, Proc. R. Soc. London A **161**, 220 (1937).

[166] R.G. Pearson, Symmetry Rules for Chemical Reactions, Wiley, New York (1976).

[167] E.R. Davidson, W.D. Borden, J. Phys. Chem. **87**, 4783 (1983).

[168] G. Herzberg, The Spectra and Structures of Simple Free Radicals: An Introduction to Molecular Spectroscopy, Dover, 1989, p. 164.

[169] S. Fortier, T.W. Hayton, Coord. Chem. Rev. **254**, 197 (2010).

[170] K.E. Gutowski, D.A. Dixon, J. Phys. Chem. A **110**, 8840 (2006).

[171] P.J. Hay, R.L. Martin, G. Schreckenbach, J. Phys. Chem. A **104**, 6259 (2000).

[172] L.V. Moskaleva, S. Krüger, A. Spörl, N. Rösch, Inorg. Chem. **43**, 4080 (2004).

[173] F. Schlosser, A Relativistic Density Functional Study of Actinide Complexation in Aqueous Solution, Dissertation, Technische Universität München (2006).

[174] P.G. Allen, J.J. Bucher, D.K. Shuh, N.M. Edelstein, T. Reich, Inorg. Chem. **36**, 4676 (1997).

[175] A. Klamt, G. Schüürmann, J. Chem. Soc., Perkin Trans. **2**, 799 (1993).

[176] M. Gal, P.L. Goggin, J. Mink, Spectrochim. Acta **48A**, 121 (1992).

[177] V.Ya. Antonchenko, E.S. Kryachko, Theor. Chem. Acc. **120**, 421 (2008).

[178] G.S. Groenewold, A.K. Gianotto, M.E. McIlwain, M.J. Van Stipdonk, M. Kullman, D.T. Moore, N. Polfer, J. Oomens, I. Infante, L. Visscher, B. Siboulet, W.A. de Jong, J. Phys. Chem A **112**, 508 (2008).

[179] M. Straka, K.G. Dyall, P. Pyykkö, Theor. Chem. Acc. **106**, 393 (2001).

[180] Y. Oda, A. Aoshima, J. Nucl. Sci. Techno. **39**, 647 (2002).

[181] G.A. Shamov, G. Schreckenbach, T.N. Vo, Chem. Eur. J **13**, 4932 (2007).

[182] P. Pyykkö, J. Li, N. Runeberg, J. Phys. Chem. **98**, 4809 (1994).

[183] C.N. Trung, G.M. Begun, D.A. Palmer, Inorg. Chem. **31**, 5280 (1992).

[184] G.L. Gresham, A.K. Gianotto, P. de B. Harrington, L. Cao, J.R. Scott, J.E. Olson, A.D. Appelhans, M.J. Van Stipdonk, G.S. Groenewold, J. Phys. Chem. A **107**, 8530 (2003).

[185] M.V. Stipdonk, V. Anbalagan, W. Chien, G. Gresham, G. Groenewold, D. Hanna, J. Am. Soc. Mass Spectrom. **14**, 1205 (2003).

[186] K.I.M. Ingram, L.J.L. Häller, N. Kaltsoyannis, Dalton Trans. 2403 (2006).

[187] Z. Cao, K. Balasubramanian, J. Chem. Phys. **131**, 164504 (2009).

[188] M. Lundberg, P.E.M. Siegbahn, J. Chem. Phys. **122**, 224103 (2005).

[189] X. Cao, M. Dolg, H. Stoll, J. Chem. Phys. **118**, 487 (2003).

[190] M. Garcia-Hernández, C. Lauterbach, S. Krüger, A. Matveev, N. Rösch, J. Comp. Chem. **23**, 834 (2002).

[191] Y. Oda, A. Aoshima, J. Nucl. Sci. Techno. **39**, 647 (2002).

[192] K.L. Schuchardt, B.T. Didier, T. Elsethagen, L. Sun, V. Gurumoorthi, J. Chase, L. Li, T.L. Windus, J. Chem. Inf. Model. **47**, 1045, (2007).

[193] T. Minami, O. Matsuoka, Theo. Chim. Acta **90**, 27 (1995).

[194] P.O. Widmark, P.-Å. Malmqvist, B. Roos, Theor. Chim. Acta **77**, 291 (1990).

[195] F.B. Van Duijneveldt, F. B. IBM Res. Rep. RJ 945, (1971).

[196] S. Huzinaga, J. Andzelm, M. Klobukowski, E. Radzio-Andzelm, Y. Sakai, H. Tatewaki, Gaussian Basis Sets for Molecular Calculations, Elsevier, Amsterdam (1984).

[197] M.J. Frisch, J.A. Pople, J.S. Binkley, J. Chem. Phys. **80**, 3265, 1984.